IMPROVED SENSITIVITY IN FLUORESCENCE SPECTROSCOPY AND MICROSCOPY

A Dissertation
Presented to
The Academic Faculty

by

Blake C. Fleischer

In Partial Fulfillment
of the Requirements for the Degree
Doctor of Philosophy in the
School of Chemisty and Biochemistry

Georgia Institute of Technology
May 2016

IMPROVED SENSITIVITY IN FLUORESCENCE SPECTROSCOPY AND MICROSCOPY

Approved by:

Professor Robert M. Dickson, Advisor
School of Chemistry and Biochemistry
Georgia Institute of Technology

Professor Joseph W. Perry
School of Chemistry and Biochemistry
Georgia Institute of Technology

Professor Bridgette A. Barry
School of Chemistry and Biochemistry
Georgia Institute of Technology

Professor Harold D. Kim
School of Physics
Georgia Institute of Technology

Professor Jennifer E. Curtis
School of Physics
Georgia Institute of Technology

Date Approved: March 9, 2016

ACKNOWLEDGMENTS

The work presented in this thesis has benefited from the efforts of many individuals. I would like to thank my dissertation advisor, Prof. Robert Dickson, for the freedom to explore my ideas and methods. I would like to thank my doctoral committee members, Profs. Bridgette Barry, Jennifer Curtis, Joseph Perry, and Harold Kim for their insight and thoughtful advice.

I thank both current and former Dickson lab members, with special thanks to Andrew Khalil, Jung-Cheng Hsiang, Amy Jablonski, and Chaoyang Fan for their support, collaboration, and insight. I would also like to thank the department staff for their patient and kind aid especially Nicole Thompson, Marketta Powers, Ebere Lima, Wendy Harris, Cam Tyson, and Kenyetta Johnson. I want to extend my gratitude to the Partnership for an Advanced Computing Environment (PACE) both for funding my graduate studies and the opportunities for professional and personal growth.

Finally, I would like to thank my family. To my wife Candace, I am incredibly grateful for your steadfast support and encouragement.

TABLE OF CONTENTS

LIST OF TABLES

LIST OF FIGURES

LIST OF SYMBOLS AND ABBREVIATIONS

$\otimes$	Convolution
$*$	Correlation
μ	Extinction coefficient
μ_n	Moment of order n
c	Speed of light
h	Planck's constant
I_{exc}	Primary excitation intensity
I_{sat}	Saturation intensity
I_{sec}	Secondary excitation intensity
k_B	Boltzmann constant
k_{exc}	Excitation rate
$k_{offExit}$	Sum of rates out of the dark state
s_k	Time-dependent stochastic blinking
ε	Extinction coefficient or molar absorption coefficient
ε_k	Molecular brightness for fluorescence emitter k
η	Viscosity
κ_n	Cumulant of order n
λ	Wavelength
σ	Absorption cross section
σ_{dark}	Dark state absorption cross section
τ_c	Characteristic time
τ_{fl}	Fluorescence lifetime

τ_{off}	Off time
τ_{on}	On time
Φ	Quantum yield
Φ_{revisc}	Reverse intersystem crossing yield
2D	Two dimensional
3D	Three dimensional
Ag-DNA	DNA scaffolded silver cluster fluorophores
AOM	Acousto optical modulator
APD	Avalanche photo diode
CCD	Charge coupled device
CW	Continuous wave
EOM	Electro optical modulator
FCS	Fluorescence correlation spectroscopy
FFT	Fast fourier transform
FIFO	First in first out
FWHM	Full width at half maximum
MSD	Mean square displacement
NA	Numerical aperture
PEG	Polyethylene glycol
PMT	Photomultiplier tube
PSF	Point spread function
PVA	Polyvinyl alcohol
QD	Quantum dot
SAFIRe	Synchronously Amplified Fluorescence Imaging Recovery
SOFI	Super resolution optical fluctuation imaging

SPT	Single particle tracking
ss-DNA	Single stranded DNA
TTL	Transistor transistor logic

SUMMARY

Fluorescence spectroscopy and microscopy are widely applied in biological systems. However, challenges still remain due to endogenous background signal that obscures measurements and spatial resolution that is limited by excitation and emission wavelengths. Additionally, diffusive processes inherent in the aqueous biological environment place artificial limits on the timeframes of study. This work describes sensitivity and resolution improvements to fluorescence-based measurements through a combination of optical modulation and correlative methods including fluorescence correlation spectroscopy (FCS), synchronously amplified fluorescence image recovery (SAFIRe) and super-resolution optical fluctuation imaging (SOFI). Ag-DNA clusters are used as a modulatable fluorophore that is both photostable and sensitive to optical modulation. Work on a single particle, real-time tracking instrument is also detailed with the goal of extending the time that diffusing particles remain in the focus of a microscope and enabling analysis over longer time scales.

First, the combination of SAFIRe with FCS is presented, describing a theoretical framework for background subtracted FCS (SAFIRe-FCS) and demonstrating concentration recovery of an analyte of interest amid high fluorescence background. Background reduction in Ag-DNA clusters is also demonstrated through pulsed excitation schemes, leading to a refined photophysical model describing photophysical transitions from a dark state directly to an emissive state in the absence of additional ground state excitations. The technique was then applied to FCS for concentration recovery amid background fluorescence. We report concentration recovery in the

presence of fivefold higher background. Both methods for improved sensitivity are not limited to Ag-DNA clusters and are readily applicable to biological systems.

In addition to sensitivity, resolution improvements are demonstrated using computational simulations of fluorescent signals of point scanning using a fast avalanche photodiode, followed by cumulant analysis analogous to SOFI. Important fluorophore photophysical properties are described and specific fluorophores are explored, where high fluence rates with long dark state lifetimes are crucial for resolution improvements and rhodamine 6G is identified as a potentially useful dye. Finally, work on a single particle tracking instrument is reported in an effort to extend the observation time of freely diffusing single fluorophores with eventual application to particle tracking in high background biological systems. Such an instrument would to provide new insights into relatively fast intramolecular interactions, traditionally hard to observe in freely diffusing particles on a single-molecule level. The work in this thesis covers a number of different approaches to improved fluorescence sensitivity, including the combination of SAFIRe with FCS, pulsed excitation, SOFI and single particle tracking. Future applications are targeted towards biological environments that present high background, such as biological systems or assays with multiple fluorophores.

CHAPTER 1

INTRODUCTION

1.1 Motivation

Fluorescence microscopy has provided important insight into fundamental biological processes. Our understanding of sub-cellular dynamics and signaling pathways has progressed as a result of significant research efforts focused on fluorophore biocompatibility, brightness, photostability, labelling efficiency, and tunability as well as technique and instrument development.[1-12] Many of these efforts are aimed at improving sensitivity as nearly all biologically relevant environments contribute background signals that obscure the signal of interest.[13-17]

Fluorescence microscopy applied in a biological context suffers from endogenous background fluorescence wherein various components present in living tissue exhibit fluorescence that competes with the analyte signal.[15] Background fluorescence reduces sensitivity and is defined as the ratio of signal to noise. Sensitivity can be improved by increasing signal, decreasing the noise, or a combination of both. Endogenous background fluorescence in biological samples, often from flavins, nicotinamide adenine dinucleotide (NADH), collagen, or hemoglobin can be simultaneously excited with the species of interest and are treated as a form of noise that decreases sensitivity.[14-17] Increases in signal are often pursued through brighter, more photostable fluorophores and higher labelling efficiency. Noise reduction frequently occurs through the design and application of fluorescent labels that have minimal spectral overlap with endogenous fluorescence.[5,11,15,18,19] The need for increased sensitivity has also resulted in technique

development including confocal microscopy, multiphoton excitation, and optical modulation.[10,20,21] The complexity and difficulty when studying biological processes continually drives the pursuit of novel approaches.

This thesis describes sensitivity improvements to fluorescence-based methods as a result of both new and improved techniques that exploit fundamental photophysical processes. The techniques are directly applied towards sensitivity gains in concentration measurements and optical resolution, are readily applicable in related techniques such as fluorescence imaging, and are considered in the context of eventual biological application. Chapter 1 provides an introduction to fluorescence spectroscopy and microscopy, followed by a description of fluorescent probes. Advanced fluorescence methods including optical modulation, single molecule measurements, and super-resolution are also presented in this thesis. Background for each method will also be presented in this chapter.

1.2 Fluorescence Spectroscopy

Fluorescence occurs through the absorption of electromagnetic energy in the visible to ultraviolet range and can be depicted using a Jablonski diagram, shown in Figure 1.1.[22,23] Excitation of an electron from a ground electronic to an excited electronic state occurs after absorption of a photon with the appropriate energy. The emission of light resulting from relaxation from higher to lower electronic spin paired states is known as fluorescence. The time spent in the higher electronic state before radiative relaxation is known as the fluorescence lifetime τ_{fl}, and relaxation occurs at a rate equal to the inverse lifetime (k_{fl}). The absorption of fluorescence emitters can be represented in terms of individual fluorophores by the absorption cross section (σ), or in terms of fluorophore

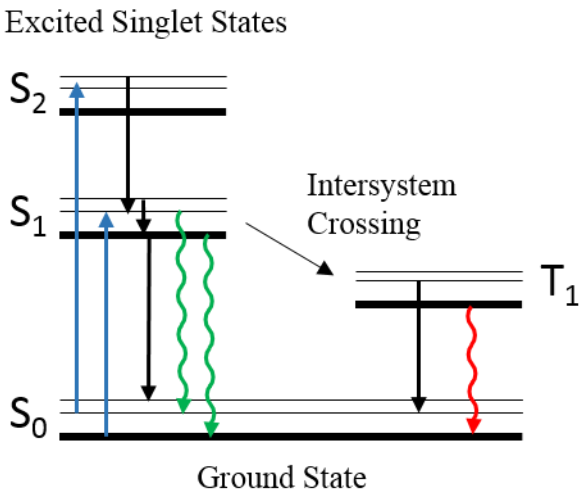

Figure 1.1. Jablonski diagram, showing absorptions in blue (~10^{-15} s), internal conversion (~10^{-14} - 10^{-9} s) and other nonemissive relaxations in black, fluorescence in green (~10^{-9} - 10^{-6} s) and phosphorescence in red (10^{-3} - 10^{3} s). Adapted from Lakowicz.[23]

molar concentration as the extinction coefficient (ε), also known as the molar absorption coefficient. Not all relaxations from excited states are in the form of fluorescence. The quantum yield of fluorescence (Φ_{fl}) and intersystem crossing (dark state) yield (Φ_{isc}) are measures of the likelihood that excited fluorophores relax via fluorescence or transition into different (here, nonemissive) manifold of states, respectively. Importantly, relaxation to the ground state can also occur non-radiatively, such as through vibrational energy dissipation. Fluorophores may also cross into metastable states which last several orders of magnitude longer than fluorescence (μs vs ns), after which fluorophores non-radiatively relax to the ground state. Such metastable states can occur as a result of charge separation, photoisomeriazation, or different spin multiplicities and their relaxation regenerates the original ground state, leading to additional fluorescence. Any process that hastens such relaxation to the ground state offers the potential to modulate molecular fluorescence.

The use of fluorescence in biological studies is very widespread due to high sensitivity (single molecule), fast temporal (ns) and high spatial resolution (100's of nm).[2,22,23] All known fluorophores suffer from photobleaching, defined as any process that limits the total number of excitation and emissive relaxation processes.[2] Fluorescence spectroscopy utilizes fluorescent labels to report on specific species within the context of a large sample. Depending on type and distribution of the fluorophore, fluorescence spectroscopy can be used to determine a wide range of information including position, dynamics, and concentration. [2 22,23]

1.3 Fluorescent Probes

1.3.1 General Overview

Fluorescence studies are made possible through the use of fluorescent labels which respond to excitation by the emission of photons. Common fluorophores include organic dyes, fluorescent proteins, and quantum dots (QDs). Organic dyes are perhaps the most well established fluorescent label and are available in a range of emission wavelengths ranging from UV into the near IR. Organic dye extinction coefficients can be as large as ~$3x10^5$ M^{-1} cm^{-1}, can have fluorescent quantum yields of up to ~0.9, and fluorescent lifetimes typically between 1-10 ns.[23,24] Although they have found application in biology due to their small size, organic dyes require specialized delivery across cellular membranes and have lower photostability compared to nanoparticles such as quantum dots (QDs).

Fluorescent proteins have shown great promise in biological applications as they can be genetically encoded and expressed within living systems.[25,26] Fluorescent proteins

are available in a wide array of colors ranging from blue to red.[25,27] Extinction coefficients of fluorescent proteins range up to ~1x10^5 M^{-1} cm^{-1}, have fluorescence quantum yields typically 0.6 or below, typical fluorescence lifetimes 1-4 ns, and exhibit photostabilities comparable to organic dyes.[27-29]

QDs are significantly more photostable, are comprised generally of biologically incompatible materials, and require some functionalization of biocompatible ligands for use in biological applications.[30-32] QD emission is available in a wide range of colors, exhibit large extinction coefficients from 10^5 to 10^6 M^{-1} cm^{-1}, fluorescence lifetimes ranging from 1-100 ns, and fluorescent quantum yields ranging from 0.1 to 0.8.[24] Quantum dots are significantly larger than other fluorescent probes (~30 nm) as they must be functionalized for biological compatibility.[29,30,33]

In the pursuit of improved photostability and size, our group has developed fluorescent silver clusters scaffolded by single stranded (ss) DNA.[11,34] A variety of colors have been reported by varying the DNA, resulting in blue to near-IR wavelength emission.[9,35] Extinction coefficients of the Ag-DNA clusters are typically ~10^5 M^{-1} cm^{-1}, fluorescence lifetimes range from 2-6 ns, and quantum yields range from 0.1 to 0.4.[9,35] Ag-DNA clusters are used extensively throughout this thesis and will be described in more detail in the section that follows.

1.3.2 Ag-DNA Cluster Background

Our group has previously reported the use of highly photostable, optically modulatable Ag-DNA clusters.[20,35,36] As aqueous solutions of Ag alone lead to large nanoparticle formations that do not emit fluorescence, the use of scaffolds is crucial to Ag fluorophore formation.[37-39] Much like previous work in rare gas matrices, the

application of oligonucleotides and peptides allowed the formation of smaller cluster sizes.[40,41] However, the peptides provided a greater control over nanoparticle size and ultimately led to much greater control over the optical properties of silver clusters. The use of a negatively charged phosphodiester DNA backbone presents multiple potential sites of Ag-DNA interaction.[42-44] Silver clusters of only cytosine have also been demonstrated.[36] Exhibiting high absorption cross sections, nanosecond fluorescence lifetimes and reasonable fluorescent quantum yields, Ag-DNA clusters are relatively bright fluorophores.[9,18,35]

The dark state of Ag-DNA clusters is thought to be a result of a charge-separated state.[45] Previous reports of the Ag-DNA cluster Stokes shift dependence on solvent polarity, microsecond blinking, and similar transient absorption spectra in the infrared (IR) region across varying compositions of Ag-DNA clusters all point to a charge-separated nonfluorescent state. Similar behavior observed in pyrene-deoxynucleotide coupled systems was identified as an anionic nucleotide absorption that relaxed via charge recombination, and represents an analogous charge separated system with very similar transient absorption.[46]

1.4 Fluorescence Microscopy

One of the most ubiquitous tools for observing single molecules is the fluorescence microscope. Originally developed in the 1960's, epi-fluorescent microscopes utilize the same light path for excitation and emission by employing a dichroic mirror and optical filters to separate fluorescence emission by wavelength. Biological fluorescent microscopes are often operated in a widefield configuration, where excitation and emission are uniform across the sample.[43,45,47] Fluorescence emission from

the entire sample volume is then collected on a detector, commonly a charge-coupled device (CCD) camera.

Confocal configurations are also employed, constraining excitation and emission through a small pinhole that rejects out of focus emission and results in a gain in axial and lateral resolution.[48,49] Thus, only a single point within a sample may be imaged at a time, and confocal images are obtained through laser scanning, stage rastering, or a combination of both. Detection of confocal signals is typically on a single element detector, such as a photomultiplier tube (PMT) or an avalanche photodiode (APD). These devices have a single sensitive element which responds to external light and are capable of recording individual photons. Quantum efficiency (QE), or the ability to convert photons into electrons, is an important deciding factor when choosing a detector. Avalanche photodiodes in general have a higher QE in the 600-900 nm wavelength range and are used in this work.

1.5 Improved Fluorescence Methods

The focus of this thesis is to gain improved sensitivity through fluorescence-based techniques. A major theme in this thesis is the development of all-optical methods for increasing fluorescence sensitivity, an extension of previous work in our group.[11] In addition, the work herein builds on previous work in our lab related to imaging beyond the few-hundred nm optical resolution limit in conventional fluorescence microscopes, and thus single molecule and super-resolution techniques will be introduced.[50,51]

1.5.1 Optical Modulation

Improved fluorescence microscopy techniques have leveraged the photophysical properties of fluorophores to dynamically and selectively influence intensities of analyte

over background. One method for improving the fluorescence signal to noise ratio is through a technique known as optical modulation. As fluorescence is a result of optical excitation, optical modulation is the fluorescence response to two wavelength separated excitation sources such that a primary excitation induces fluorescence and a secondary excitation modulates analyte fluorescence intensity. By optically modulating a sample with analyte fluorophores sensitive to secondary excitation, it is possible to modulate fluorescence of only analyte, leaving the background fluorescence unaffected. Detecting at the specific modulation frequency provides a means to recover analyte from background, significantly improving sensitivity.

As an example, the case of a fluorophore with a metastable nonemissive state that is optically sensitive to long wavelength excitation is considered. Primary excitation induces excitation to an emissive state, and fluorescence relaxation results in emission of photons. A fraction of all excited photons enter the metastable nonemissive state, reducing total fluorescence fluency. Application of a time variant secondary excitation intensity depopulates the nonemissive state, causing a corresponding time-variance in analyte fluorescence. Importantly, the secondary excitation does not interact with background, only affecting analyte fluorescence. Variations in fluorescence can then be post-processed to extract signal over background.

1.5.1.1 Optical Modulation Techniques

Optical modulation for improved fluorescence sensitivity has been accomplished in more than one way. Demonstrated with photoswitch flurophores, optical lock-in detection (OLID) reduces background through a cross-correlation of modulated fluorescence signal to an internal reference.[21,52] Only fluorescence variations that occur

simultaneously in both the reference and signal are recovered in the correlation, as all other fluorescence is averaged out.[21] Improving on OLID, synchronously amplified fluorescence image recovery (SAFIRe) improves signal to noise by selective observation of dynamic photobrightening at only the externally encoded secondary modulation frequency. Frequently, this signal is decoded via Fourier transforms (FT) where image contrast is directly proportional to the FT amplitude at the externally encoded excitation frequency.[10,11,51,53,54] The amplitude of SAFIRe photobrightening scales linearly with the number of modulated flurophores, a contrast to OLID which is comprised of the product of signal with reference, normalized by the standard deviation of intensity values.[21,54]

1.5.1.2 Fluorophores for Optical modulation

Optical modulation schemes have utilized both slower fluorophore photoswitches and more rapid responding fluorophores resulting from population shifts between states modelled as triplet or charge separated states.[10,11,20,21,51,52,54,55] Photoswitches comprise a subset of fluorophores that respond to additional optical excitation by reversibly switching between emissive and nonemissive states and often undergo some sort of conformational change.[21,56,57] As a result, their response is typically slower (s to hundreds of ms) and subsequently limit biological applications that may be observed within that timeframe. Faster responses have been reported in fluorophores utilizing photophysical dark states resulting in optical responses in the ms to μs time frames.[11,18,55] This opens avenues to faster observations, but is limited to fluorophores equipped with optically depopulatable nonemissive states.

Ag-DNA clusters are were the first class of emitters shown to be optically modulated.[20] Excitation via a primary laser induces fluorescence, followed by relaxation

into a μs-lived nonemissive state that can be depopulated with long wavelength co-excitation. The cluster dark state maximally absorbs excitation between 700-800 nm, a wavelength range which typical endogenous biological fluorescence is significantly less sensitive.[45] As a result, long-wavelength secondary excitation minimally interacts with background while rapidly depopulating Ag-DNA cluster dark states, modulating fluorescence intensities in only the Ag-DNA and not background. In addition, Ag-DNA clusters have good fluorescence quantum yields and high intersystem crossing rates that make them ideal candidates for optical modulation.[35] Specifically, a high intersystem crossing rate into a nonemissive state allows rapid formation of dark state populations, enabling faster rates of optical modulation that report on the rates in and out of dark states.[20,35] The high photostability of Ag-DNA clusters makes them good candidates for novel extensions to optical modulation, especially those that benefit from low concentration or even single molecule experiments.

1.5.2 Single Molecule Fluorescence

Although traditionally applied to bulk samples, sensitivity improvements from optical modulation could in principle be applied at the single molecule level. Single molecule experiments are complementary to bulk measurements, which inherently incorporate molecular averaging and thus reveal the most common behaviors as they are often the most important for understanding a system. However, single molecule experiments are particularly well suited to capture infrequent, unsynchronized, or otherwise weakly observable phenomena so long as many measurements are made to statistically sample the full range of behaviors in an unbiased manner.

The early single molecule experiments were conducted in solids at cryogenic temperatures to minimize spectral broadening due to thermal processes and thus obtain more narrow spectra, relying on the combination of optical spectroscopy with Stark or ultrasonic modulation to observe the absorption of single molecules.[58,59] The superior sensitivity of fluorescence compared to absorbance marked the advancement of single molecule study.[60-63] As a result, fluorescence is widely used in modern single molecule experiments, providing important fundamental mechanistics insights.[8,63] Examples of single molecule fluorescence contributions to the field of biological study include embryonic stem cell-specific gene regulation and observation of the rotation of F1-ATPase, essential components in biological growth and immunology.[64,65] Relevant techniques to single molecule measurements are fluorescence correlation spectroscopy (FCS), described in Chapter 3 and single particle tracking, described in Chapter 6.

Advances in single molecule fluorescence microscopy were initially limited to spatially separated emitters usually as a result of very low concentrations. Such low concentrations do not represent realistic conditions for biological systems as fluorophores are not perfectly separated in living systems and are often in very close proximity. Resolving overlapping fluorescence from separate emitters in close spatial proximity has presented a new challenge as smaller and smaller length scales are approached. As a result, a variety of techniques has emerged to address resolution below the optical resolution limit.

1.5.3 Super-Resolution Microscopy

The pursuit of understanding ever greater detail in biological systems has driven optical microscopes to probe smaller length scales. While other methods of imaging

small length scales exist, optical microscopy has the distinct advantage of fast temporal resolution and noninvasivity, crucial properties for observing biological systems. Due to the intrinsic properties of light, there is a fundamental limit to how tightly an excitation source can be focused, presenting a barrier to imaging structures of decreasing size. As a result, many methodologies have emerged to circumvent this limit.

Also known as the diffraction barrier, the ability of optical components to collect and focus light is fundamentally governed by the wave nature of light, a result of diffraction caused by the action of interference. For any real lens of finite size, there is a limit to its ability to gather light, represented in terms of half angle from the optical axis. Defined as the numerical aperture (NA), the focusing ability of any practical lens is the product of sin Θ of this half angle and the index of refraction *n*, such that:

$$\mathrm{NA} = n \sin \Theta \qquad \text{Equation 1.1}$$

Employing NA as part of the physical description of a focusing lens, the Abbe limit, proposed by Ernst Abbe, describes the radius (*d*) of the tightest spot that light may be focused as:

$$d = \frac{\lambda}{2\,NA} \qquad \text{Equation 1.2}$$

or:

$$d = \frac{\lambda}{2\,n \sin \Theta} \qquad \text{Equation 1.3}$$

where λ is the wavelength of light.[66,67] However, this limit, roughly half the wavelength of light and resulting from the focusing ability of practical optical components, does not prevent fluorescent observations beyond this length scale. As a result, many different

methodologies have emerged to resolve beyond the optical limit, collectively referred to as "super-resolution".[8,59,62,68-71] Super-resolution methods may be broadly categorized as manipulation of the excitation point spread function (PSF),[69,72,73] signal separation into additional domains such as time or wavelength,[59,68] and post-experimental analysis or post-processing.[74-76]

1.5.3.1 Manipulation of the Excitation Point Spread Function (PSF)

Fundamentally, the Abbe limit describes the greatest ability for a microscope to focus light, and anything smaller is 'spread out' to a degree, characterized by the PSF. This was slightly reduced in confocal microscopy by constraining excitation and emission through a small pinhole, resulting in a resolution increase of approximately $\sqrt{2}$. Stimulated Emission Depletion (STED) incorporates a dual excitation scheme, exciting with one laser and depleting excited states with a second, ring shaped excitation pattern that narrows collected fluorescence more than that by a single focused laser alone.[69] Structured illumination microscopy (SIM) along with saturated illumination (SSIM) utilizes multiple structurally varying excitation patterns to collect high resolution structural information, which is visualized through computational post-processing.[73,77]

1.5.3.2 Separation into Additional Dimensions

While reductions in the PSF are important for super-resolution, it is also possible to separate fluorescence into additional dimensions. Photoactivated localization microscopy (PALM) and stochastic optical reconstruction microscopy (STORM) employ optically controlled photoswitchable fluorophores, stochastically activated, imaged, and photobleached such that overlapping fluorophores that would otherwise reside in a diffraction limited volume are temporally separated.[68,78] Fluorescence from overlapping

emitters may alternatively be separated in terms of wavelength through the use of an external electric field, such that the resulting fluorescence is wavelength-shifted as a function of position due to the Stark effect.[79]

1.5.3.3 Post-Processing

Finally, one can apply post-processing to fluorescent signals to image beyond the diffraction limit. Careful observation of sequential photobleaching fluorophores with overlapping PSFs is used to determine the final positions, referred to as Single-Molecule High-Resolution Imaging with Photobleaching (SHRImP).[74] Bayesian analysis of the blinking and bleaching (3B) models collected signals as being generated by a number of fluorophores that may or may not be emitting at any given time.[75] Lastly, in stochastic optical fluctuation imaging (SOFI), higher order cumulant statistics are used to determine independence between individual overlapping and blinking emitters.[76,80] A detailed introduction to SOFI will be presented in Chapter 5.

1.8 Overview of Thesis

The work presented in this thesis focuses on improved fluorescence sensitivity as a result of the application of new techniques exploiting fundamental photophysical processes. Specifically, in Chapters 3 and 4, photophysical characteristics of optically modulatable Ag-DNA clusters are investigated and utilized to determine quantitative measures of concentration, demonstrating novel and near background free methodologies for improved sensitivity. The same photophysical properties that lead to blinking are also explored in the context of super-resolution microscopy in Chapter 5, where computational simulation is used to explore physically relevant parameters for optimal resolution enhancements. Finally, progress in a fluorescence-based single particle

tracking instrument is detailed in Chapter 6 with the eventual goal of applying optical modulation for improved fluorescence sensitivity in biologically relevant highly autofluorescent environments. Through novel technique development, additional tools become available to the scientist pushing the boundaries of biological fluorescence spectroscopy ever further.

1.9 References

1. Combs, C. A. "Fluorescence Microscopy: A Concise Guide to Current Imaging Methods." *Current Protocols in Neuroscience*, **2010**, *0 2*, 2.1-2.1.

2. Lichtman, J. W.; Conchello, J.-A. "Fluorescence microscopy." *Nature Methods*, **2005**, *2*, 910-919.

3. Meyer, T.; Teruel, M. N. "Fluorescence imaging of signaling networks." *Trends in Cell Biology*, **2003**, *13*, 101-106.

4. Weissleder, R.; Ntziachristos, V. "Shedding light onto live molecular targets." *Nature Medicine*, **2003**, *9*, 123-128.

5. Rao, J.; Dragulescu-Andrasi, A.; Yao, H. "Fluorescence imaging in vivo: recent advances." *Current Opinion in Biotechnology*, **2007**, *18*, 17-25.

6. Weiss, S. "Fluorescence Spectroscopy of Single Biomolecules." *Science*, **1999**, *283*, 1676-1683.

7. Kim, S. A.; Heinze, K. G.; Schwille, P. "Fluorescence correlation spectroscopy in living cells." *Nature Methods*, **2007**, *4*, 963-973.

8. Joo, C.; Balci, H.; Ishitsuka, Y.; Buranachai, C.; Ha, T. "Advances in Single-Molecule Fluorescence Methods for Molecular Biology." *Annual Review of Biochemistry*, **2008**, *77*, 51-76.

9. Richards, C. I.; Choi, S.; Hsiang, J.-C.; Antoku, Y.; Vosch, T.; Bongiorno, A.; Tzeng, Y.-L.; Dickson, R. M. "Oligonucleotide-stabilized Ag nanocluster fluorophores." *Journal of the American Chemical Society*, **2008**, *130*, 5038-5039.

10. Richards, C. I.; Hsiang, J.-C.; Dickson, R. M. "Synchronously amplified fluorescence image recovery (SAFIRe)." *The Journal of Physical Chemistry B*, **2010**, *114*, 660-665.

11. Hsiang, J. C.; Jablonski, A. E.; Dickson, R. M. "Optically modulated fluorescence bioimaging: Visualizing obscured fluorophores in high background." *Accounts of Chemical Research*, **2014**, *47*, 1545-1554.

12. Zheng, Q.; Juette, M. F.; Jockusch, S.; Wasserman, M. R.; Zhou, Z.; Altman, R. B.; Blanchard, S. C. "Ultra-stable organic fluorophores for single-molecule research." *Chemical Society Reviews*, **2014**, *43*, 1044-1056.

13. Aubin, J. E. "Autofluorescence of viable cultured mammalian cells." *The journal of histochemistry and cytochemistry : official journal of the Histochemistry Society*, **1979**, *27*, 36-43.

14. Andersson; Baechi; Hoechl; Richter "Autofluorescence of living cells." *Journal of Microscopy*, **1998**, *191*, 1-7.

15. Mansfield, J. R.; Gossage, K. W.; Hoyt, C. C.; Levenson, R. M. "Autofluorescence removal, multiplexing, and automated analysis methods for in-vivo fluorescence imaging." *Journal of Biomedical Optics*, **2005**, *10*, 041207-041201 - 041207-041209.

16. Vigneshwaran, N.; Bijukumar, G.; Karmakar, N.; Anand, S.; Misra, A. "Autofluorescence characterization of advanced glycation end products of hemoglobin." *Spectrochimica Acta Part A: Molecular and Biomolecular Spectroscopy*, **2005**, *61*, 163-170.

17. Lin, B.; Urayama, S.; Saroufeem, R. M. G.; Matthews, D. L.; Demos, S. G. "Characterizing the origin of autofluorescence in human esophageal epithelium under ultraviolet excitation." *Optics express*, **2010**, *18*, 21074-21074.

18. Petty, J. T.; Fan, C.; Story, S. P.; Sengupta, B.; St. John Iyer, A.; Prudowsky, Z.; Dickson, R. M. "DNA encapsulation of 10 silver atoms producing a bright, modulatable, near-infrared-emitting cluster." *Journal of Physical Chemistry Letters*, **2010**, *1*, 2524-2529.

19. Petty, J. T.; Fan, C.; Story, S. P.; Sengupta, B.; Sartin, M.; Hsiang, J. C.; Perry, J. W.; Dickson, R. M. "Optically enhanced, near-IR, silver cluster emission altered by single base changes in the DNA template." *Journal of Physical Chemistry B*, **2011**, *115*, 7996-8003.

20. Richards, C. I.; Hsiang, J.-C.; Senapati, D.; Patel, S.; Yu, J.; Vosch, T.; Dickson, R. M. "Optically Modulated Fluorophores for Selective Fluorescence Signal Recovery." *Journal of the American Chemical Society*, **2009**, *131*, 4619-4621.

21. Marriott, G.; Mao, S.; Sakata, T.; Ran, J.; Jackson, D. "Optical lock-in detection imaging microscopy for contrast-enhanced imaging in living cells." *Proceedings of the National Academy of Sciences,* **2008**.

22. Michalet, X.; Kapanidis, A. N.; Laurence, T.; Pinaud, F.; Doose, S.; Pflughoefft, M.; Weiss, S. "The Power and Prospects of Fluorescence Microscopies and Spectroscopies." *Annual Review of Biophysics and Biomolecular Structure,* **2003**, *32*, 161-182.

23. Lakowicz, J. R. *Principles of Fluorescence Spectroscopy*; Springer: New York, 2006.

24. Resch-Genger, U.; Grabolle, M.; Cavaliere-Jaricot, S.; Nitschke, R.; Nann, T. "Quantum dots versus organic dyes as fluorescent labels." *Nature Methods,* **2008**, *5*, 763-775.

25. Chudakov, D. M.; Matz, M. V.; Lukyanov, S.; Lukyanov, K. A. "Fluorescent Proteins and Their Applications in Imaging Living Cells and Tissues." *Physiological Reviews,* **2010**, *90*, 1103-1163.

26. Chudakov, D. M.; Lukyanov, S.; Lukyanov, K. A. "Fluorescent proteins as a toolkit for in vivo imaging." *Trends in Biotechnology,* **2005**, *23*, 605-613.

27. Stepanenko, O.; Stepanenko, O.; Shcherbakova, D.; Kuznetsova, I.; Turoverov, K.; Verkhusha, V. "Modern fluorescent proteins: from chromophore formation to novel intracellular applications." *BioTechniques,* **2011**, *51*, 313-327.

28. Shaner, N. C.; Steinbach, P. A.; Tsien, R. Y. "A guide to choosing fluorescent proteins." *Nature Methods,* **2005**, *2*, 905-909.

29. Berezin, M. Y.; Achilefu, S. "Fluorescence Lifetime Measurements and Biological Imaging." *Chemical Reviews,* **2010**, *110*, 2641-2684.

30. Michalet, X. "Quantum Dots for Live Cells, in Vivo Imaging, and Diagnostics." *Science,* **2005**, *307*, 538-544.

31. Derfus, A. M.; Chan, W. C. W.; Bhatia, S. N. "Probing the Cytotoxicity of Semiconductor Quantum Dots." *Nano Letters,* **2004**, *4*, 11-18.

32. Lovrić, J.; Bazzi, H. S.; Cuie, Y.; Fortin, G. R. A.; Winnik, F. M.; Maysinger, D. "Differences in subcellular distribution and toxicity of green and red emitting CdTe quantum dots." *Journal of Molecular Medicine,* **2005**, *83*, 377-385.

33. Medintz, I. L.; Uyeda, H. T.; Goldman, E. R.; Mattoussi, H. "Quantum dot bioconjugates for imaging, labelling and sensing." *Nature Materials,* **2005**, *4*, 435-446.

34. Petty, J. T.; Zheng, J.; Hud, N. V.; Dickson, R. M. "DNA-Templated Ag Nanocluster Formation." *Journal of the American Chemical Society,* **2004**, *126*, 5207-5212.

35. Vosch, T.; Antoku, Y.; Hsiang, J.-C.; Richards, C. I.; Gonzalez, J. I.; Dickson, R. M. "Strongly emissive individual DNA-encapsulated Ag nanoclusters as single-molecule fluorophores." *Proceedings of the National Academy of Sciences of the United States of America,* **2007**, *104*, 12616-12621.

36. Ritchie, C. M.; Johnsen, K. R.; Kiser, J. R.; Antoku, Y.; Dickson, R. M.; Petty, J. T. "Ag nanocluster formation using a cytosine oligonucleotide template." *Journal of Physical Chemistry C,* **2007**, *111*, 175-181.

37. Henglein, A. "Small-particle research: physicochemical properties of extremely small colloidal metal and semiconductor particles." *Chemical Reviews,* **1989**, *89*, 1861-1873.

38. Linnert, T.; Mulvaney, P.; Henglein, A.; Weller, H. "Long-lived nonmetallic silver clusters in aqueous solution: preparation and photolysis." *Journal of the American Chemical Society,* **1990**, *112*, 4657-4664.

39. Henglein, A.; Mulvaney, P.; Linnert, T. "Chemistry of Ag aggregates in aqueous solution: non-metallic oligomeric clusters and metallic particles." *Faraday Discussions,* **1991**, *92*, 31-44.

40. Diederich, T.; Tiggesbäumker, J.; Meiwes-Broer, K.-H. "Spectroscopy on rare gas–doped silver clusters in helium droplets." *The Journal of Chemical Physics,* **2002**, *116*, 3263-3269.

41. Ievlev, D.; Rabin, I.; Schulze, W.; Ertl, G. "Fluorescence spectroscopy of silver clusters formed in rare gas droplets." *The European Physical Journal D - Atomic, Molecular, Optical and Plasma Physics,* **2001**, *16*, 157-160.

42. Eichhorn, G. L.; Shin, Y. A. "Interaction of metal ions with polynucleotides and related compounds. XII. The relative effect of various metal ions on DNA helicity." *Journal of the American Chemical Society,* **1968**, *90*, 7323-7328.

43. Storhoff, J. J.; Mirkin, C. A. "Programmed Materials Synthesis with DNA." *Chemical Reviews,* **1999**, *99*, 1849-1862.

44. Becerril, H. A.; Woolley, A. T. "DNA-templated nanofabrication." *Chemical Society Reviews,* **2009**, *38*, 329-337.

45. Patel, S. a.; Cozzuol, M.; Hales, J. M.; Richards, C. I.; Sartin, M.; Hsiang, J. C.; Vosch, T.; Perry, J. W.; Dickson, R. M. "Electron transfer-induced blinking in Ag

nanodot fluorescence." *Journal of Physical Chemistry C*, **2009**, *113*, 20264-20270.

46. Trifonov, A.; Buchvarov, I.; Wagenknecht, H.-A.; Fiebig, T. "Real-time observation of hydrogen bond-assisted electron transfer to a DNA base." *Chemical Physics Letters*, **2005**, *409*, 277-280.

47. Valeur, B.; Berberan-Santos, M. N. *Molecular Fluorescence: Principles and Applications*; 2nd ed.; Wiley-VCH: Weinheim Germany, 2012.

48. Mertz, J. *Introduction to Optical Microcopy*; Roberts and Company Publishers: Greenwood Village, Colorado, 2010.

49. Hell, S. W. "Far-Field Optical Nanoscopy." *Science*, **2007**, *316*, 1153-1158.

50. Nicovich, P. R. *Widefield Fluorescence Correlation Spectroscopy.* PhD Thesis, Georgia Institute of Technology, 2010.

51. Fan, C.; Hsiang, J.-C.; Jablonski, A. E.; Dickson, R. M. "All-optical fluorescence image recovery using modulated stimulated emission depletion." *Chemical Science*, **2011**, *2*, 1080-1080.

52. Mao, S.; Benninger, R. K. P.; Yan, Y.; Petchprayoon, C.; Jackson, D.; Easley, C. J.; Piston, D. W.; Marriott, G. "Optical Lock-In Detection of FRET Using Synthetic and Genetically Encoded Optical Switches." *Biophysical journal*, **2008**, *94*, 4515-4524.

53. Jablonski, A. E. *Optically modulated fluorescent proteins.* PhD Thesis, Georgia Institute of Technology, 2014.

54. Chen, Y.-C.; Jablonski, A. E.; Issaeva, I.; Bourassa, D.; Hsiang, J.-C.; Fahrni, C. J.; Dickson, R. M. "Optically Modulated Photoswitchable Fluorescent Proteins Yield Improved Biological Imaging Sensitivity." *Journal of the American Chemical Society*, **2015**, 150924164102005-150924164102005.

55. Fan, C.; Hsiang, J.-C.; Dickson, R. M. "Optical Modulation and Selective Recovery of Cy5 Fluorescence." *ChemPhysChem*, **2012**, *13*, 1023-1029.

56. Querard, J.; Markus, T.-Z.; Plamont, M.-A.; Gauron, C.; Wang, P.; Espagne, A.; Volovitch, M.; Vriz, S.; Croquette, V.; Gautier, A.; Le Saux, T.; Jullien, L. "Photoswitching Kinetics and Phase-Sensitive Detection Add Discriminative Dimensions for Selective Fluorescence Imaging." *Angewandte Chemie International Edition*, **2015**, *54*, 2633-2637.

57. Li, A. D. Q.; Zhan, C.; Hu, D.; Wan, W.; Yao, J. "Photoswitchable nanoprobes offer unlimited brightness in frequency-domain imaging." *Journal of the American Chemical Society*, **2011**, *133*, 7628-7631.

58. Kador, L.; Horne, D. E.; Moerner, W. E. "Optical detection and probing of single dopant molecules of pentacene in a p-terphenyl host crystal by means of absorption spectroscopy." *The Journal of Physical Chemistry*, **1990**, *94*, 1237-1248.

59. Moerner, W. E.; Kador, L. "Optical detection and spectroscopy of single molecules in a solid." *Physical Review Letters*, **1989**, *62*, 2535-2538.

60. Orrit, M.; Bernard, J. "Single pentacene molecules detected by fluorescence excitation in a p-terphenyl crystal." *Physical Review Letters*, **1990**, *65*, 2716-2719.

61. Moerner, W. E.; Basché, T. "Optical Spectroscopy of Single Impurity Molecules in Solids." *Angewandte Chemie International Edition in English*, **1993**, *32*, 457-476.

62. Moerner, W. E.; Dickson, R. M.; Norris, D. J. In *Advances In Atomic, Molecular, and Optical Physics*; Benjamin, B., Herbert, W., Eds.; Academic Press: 1998; Vol. Volume 38, p 193-236.

63. Plakhotnik, T.; Donley, E. A.; Wild, U. P. "SINGLE-MOLECULE SPECTROSCOPY." *Annual Review of Physical Chemistry*, **1997**, *48*, 181-212.

64. Chen, J.; Zhang, Z.; Li, L.; Chen, B.-C.; Revyakin, A.; Hajj, B.; Legant, W.; Dahan, M.; Lionnet, T.; Betzig, E.; Tjian, R.; Liu, Z. "Single-Molecule Dynamics of Enhanceosome Assembly in Embryonic Stem Cells." *Cell*, **2014**, *156*, 1274-1285.

65. Noji, H.; Yasuda, R.; Yoshida, M.; Kinosita, K. "Direct observation of the rotation of F1-ATPase." *Nature*, **1997**, *386*, 299-302.

66. Stephenson, J. W. "Observations on Professor Abbe's Experiments illustrating his Theory of Microscopic Vision." *The Monthly Microscopical Journal*, **1877**, *17*, 82-88.

67. Abbe, E. "XV.—The Relation of Aperture and Power in the Microscope (continued)*." *Journal of the Royal Microscopical Society*, **1883**, *3*, 790-812.

68. Betzig, E.; Patterson, G. H.; Sougrat, R.; Lindwasser, O. W.; Olenych, S.; Bonifacino, J. S.; Davidson, M. W.; Lippincott-Schwartz, J.; Hess, H. F. "Imaging Intracellular Fluorescent Proteins at Nanometer Resolution." *Science*, **2006**, *313*, 1642-1645.

69. Hell, S. W.; Wichmann, J. "Breaking the diffraction resolution limit by stimulated emission: stimulated-emission-depletion fluorescence microscopy." *Optics Letters*, **1994**, *19*, 780-782.

70. Dertinger, T.; Heilemann, M.; Vogel, R.; Sauer, M.; Weiss, S. "Superresolution Optical Fluctuation Imaging with Organic Dyes." *Angewandte Chemie International Edition*, **2010**, *49*, 9441-9443.

71. Cox, S. "Super-resolution imaging in live cells." *Developmental Biology*, **2015**, *401*, 175-181.

72. Bailey, B.; Farkas, D. L.; Taylor, D. L.; Lanni, F. "Enhancement of axial resolution in fluorescence microscopy by standing-wave excitation." *Nature*, **1993**, *366*, 44-48.

73. Gustafsson, M. G. L. "Nonlinear structured-illumination microscopy: Wide-field fluorescence imaging with theoretically unlimited resolution." *Proceedings of the National Academy of Sciences of the United States of America*, **2005**, *102*, 13081-13086.

74. Gordon, M. P.; Ha, T.; Selvin, P. R. "Single-molecule high-resolution imaging with photobleaching." *Proceedings of the National Academy of Sciences of the United States of America*, **2004**, *101*, 6462-6465.

75. Cox, S.; Rosten, E.; Monypenny, J.; Jovanovic-Talisman, T.; Burnette, D. T.; Lippincott-Schwartz, J.; Jones, G. E.; Heintzmann, R. "Bayesian localization microscopy reveals nanoscale podosome dynamics." *Nature Methods*, **2012**, *9*, 195-200.

76. Dertinger, T.; Colyer, R.; Iyer, G.; Weiss, S.; Enderlein, J. "Fast, background-free, 3D super-resolution optical fluctuation imaging (SOFI)." *Proceedings of the National Academy of Sciences of the United States of America*, **2009**, *106*, 22287-22292.

77. Neil, M. A. A.; Juškaitis, R.; Wilson, T. "Method of obtaining optical sectioning by using structured light in a conventional microscope." *Optics Letters*, **1997**, *22*, 1905-1907.

78. Rust, M. J.; Bates, M.; Zhuang, X. "Sub-diffraction-limit imaging by stochastic optical reconstruction microscopy (STORM)." *Nature Methods*, **2006**, *3*, 793-796.

79. Hettich, C.; Schmitt, C.; Zitzmann, J.; Kühn, S.; Gerhardt, I.; Sandoghdar, V. "Nanometer Resolution and Coherent Optical Dipole Coupling of Two Individual Molecules." *Science*, **2002**, *298*, 385-389.

80. Dertinger, T.; Colyer, R.; Vogel, R.; Enderlein, J.; Weiss, S. "Achieving increased resolution and more pixels with Superresolution Optical Fluctuation Imaging (SOFI)." *Optics express,* **2010**, *18*, 18875-18885.

CHAPTER 2

EXPERIMENTAL METHODS

2.1 Synthesis of Ag-DNA Clusters

Analogous to our previous reports, we prepared a new 630 nm-emitting Ag nanodot that exhibits a higher dark state quantum yield than do other nanodot species.[1,2] This species is readily synthesized using our published procedures in water, but using the single stranded DNA (ss-DNA) sequence 5′-CCCCAACTCC-3′ as the template. Specifically, ss-DNA (Integrated DNA Technology) is first diluted in water to form a final 20 nM concentration solution. $AgNO_3$ (Sigma-Aldrich, 204390) is added to form a 3:1 Ag:DNA ratio via a 2 mg/mL aqueous solution. Next a 6:1 ratio of 1 mg/mL of $NaBH_4$ (Sigma-Aldrich, 213462) is added to the ss-DNA and Ag mixture within 30 seconds of combining $NaBH_4$ and water. The $NaBH_4$ was weighed immediately before adding, and added within 30 s of diluting. It is easiest to create a 1 mg/mL solution of $NaBH_4$, and then add the appropriate amount of BH_4^- to the DNA/$AgNO_3$ solution. The resulting 1 mL mixture is then vortexed for about a minute, incubated at room temperature for about six hours and then refrigerated (~2° C) for permanent storage. While Ag-DNA clusters may continue to form in the refrigerator for approximately 24-48 hours, they are stable in stock concentrations for at least two weeks.

The 710 nm Ag-DNA emitter was synthesized following our original procedure,[1] using 5′-CCCTTAATCCCC-3′ as the template. Samples for photophysical and fluorescence correlation spectroscopy (FCS) analysis were prepared as follows: ss-DNA was combined with $AgNO_3$ in a 6:1 molar ratio and incubated at room temperature for 15 minutes. The mixture was then combined with $NaBH_4$ in a 3:1 ratio of BH_4^-:DNA, vortexed for one minute and incubated at room temperature for two hours. 710 nm emitters made in the absence of buffer are not as chemically stable as the 630 nm

emitters, and should be used within a day. 630 nm emitters should be viable a month later, though they may last longer.

Fluorescence excitation and emission spectra were recorded on a fluorescence spectrophotometer (Photon Technology International QM-4/2006) and are shown in Figure 2.1.

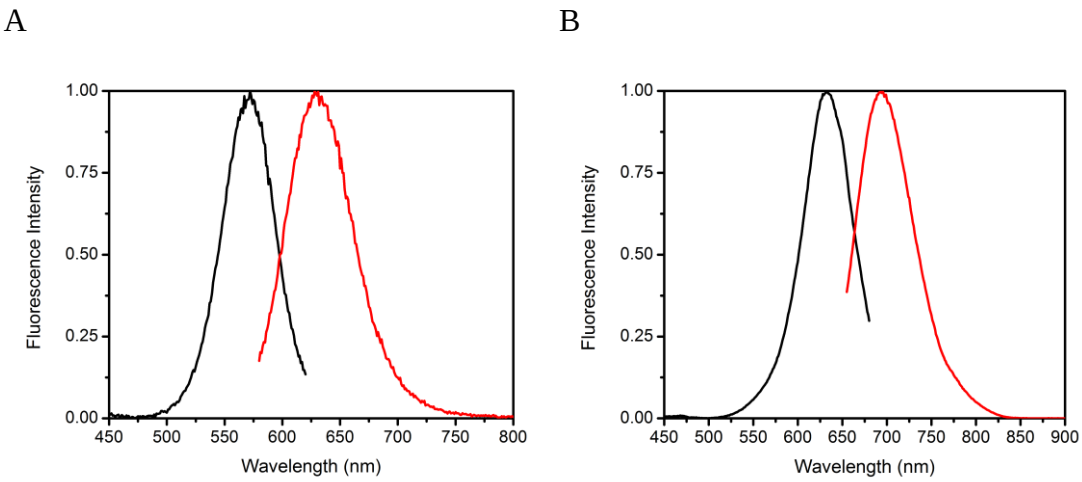

Figure 2.1. Fluorescence excitation and emission spectra for (A) 630 nm emitters and (B) 710 nm emitters.

2.2 Bulk Photophysical Characterization

Bulk photophysical absorption measurements were conducted to determine quantum yields, extinction coefficients, and photophysical rate constants. Fluorescence was recorded on a Photon Technology International (PTI) Quanta Master 40 equipped with a xenon lamp and a photomultiplier tube with sensitivity out to 900 nm. Absorption measurements were made on a Shimadzu UV-2401 PC spectrophotometer. In all cases, measurements were collected in a glass cuvette. τ_{on} was determined via FCS fits according to previous methods.[2] The determination of τ_{on} and τ_{off} were extracted from fluorescence correlation fits, detailed in Section 2.4.

2.3 Fluorescence Microscopy

All fluorescence-based microscopy (FCS, fluorescence lifetime, fluorescent imaging) experiments were performed on an Olympus IX70 or IX71 inverted microscope. Excitation was aligned into the back of the microscope, which was reflected into a 60x 1.2 NA water immersion objective for aqueous samples or a 60x 1.45 NA oil immersion objective for immobilized samples. Epi-fluorescent emission was collected by the same objective, passed through a set of emission filters selected to block both excitation wavelengths and pass emission, and then through 100-µm multimode fiber and onto an avalanche photodiode (APD) (Perkin-Elmer, SPCM-AQRH-15-FC). Fluorescence was recorded on either a Becker-Hickl SPC-630 board operated in reverse stop/start and FIFO modes, or an NI PCI-6602 fast counting board with homebuilt software written by the previous Dickson lab member Jung-Cheng Hsiang in the C programming language.

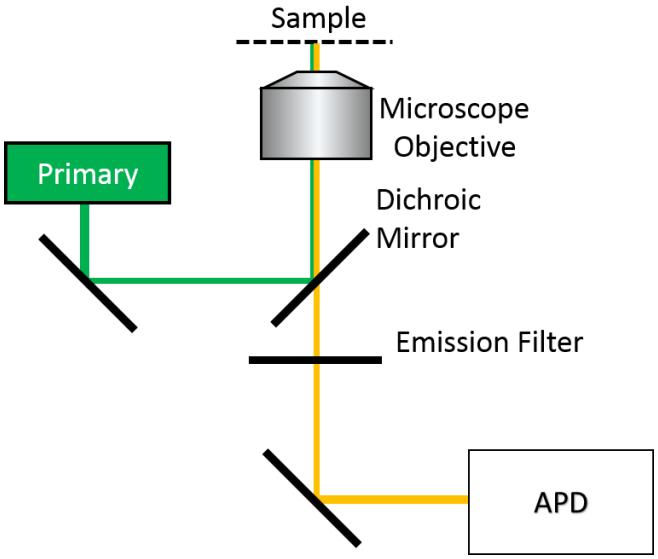

Figure 2.2. Schematic of fluorescence experiment, where a laser (primary excitation) is aligned into an epi-fluorescent microscope and onto a dichroic mirror which reflects the excitation into the objective and onto a sample. Fluorescence is collected back through the objective and passes through the dichroic mirror and an emission filter, reducing any additional light at the excitation wavelength. The light is collected on an avalanche photodiode and subsequently sent to a photon counting board (not shown).

Frequency response was determined via immobilization in 20% (w/v) PVA/H_2O in a 1:1 ratio of Ag-DNA:PVA and extremely low 560 nm excitation intensity (1.4 mW/cm^2) to minimize photobleaching while maximizing count rates. Home built software automated data collection written in the C programming language.

Fluorescence lifetimes were determined on an Olympus IX71 microscope (60x 1.2 NA water immersion objective), with a 560 nm PicoQuant LDH-D-TA-560 driven by a Sepia II controller focused into an aqueous sample. Subsequent fluorescence was collected through a 100-µm multimode fiber and routed to an avalanche photodiode (PerkinElmer, SPCM-AQRH-15-FC). Time-stamped photon arrival times were recorded with a Becker-Hickl SPC-630 board operating in reverse stop/start and FIFO modes and subsequent analysis was performed using Decayfit (http://www.fluortools.com/software/decayfit) for impulse deconvolution.

Immobilized long-term fluorescence lifetimes were acquired using Ag-DNA immobilized in 20% (w/v) PVA. In both cases, continuous wave (CW) 803 nm secondary excitation was combined with 532 nm or 643 nm primary excitation for 630 nm or 710 nm Ag-DNA clusters, respectively. The 532 or 643 nm secondary laser was expanded and collimated to backfill the objective and produce a tightly focused excitation volume. Because of a slow 10 kHz repetition rate in excitation, a Becker-Hickl HRT-41 router was used to send both fluorescent signals and timing of laser pulses to the SPC-630 counting board, each utilizing a different channel. Fluorescent lifetimes were built by assigning a photon arrival time after each laser pulse.

2.4 Fluorescence Correlation Spectroscopy

2.4.1 Theory

While not explicitly limited to single molecule measurements, FCS is a very common means of serially observing the fluorescence of many individual molecules

diffusing through the focal volume. Typically applied to solutions containing freely diffusing fluorophores, an excitation source is tightly focused into a sample and fluorescence is passed through a spatial filter (pinhole or optical fiber) and onto a fast recording device such as an APD or photomultiplier tube (PMT) with ns time resolution. Low concentrations are important such that fluctuations in fluorescence intensity are recorded with a single photon counting board. Any process that gives rise to fluctuations in fluorescence is detectable in correlative analysis, and as a result, the technique is applicable to many different physical systems such as solvated diffusion, binding kinetics, and dark state kinetics arising from photophysical transitions.

FCS traces are constructed by utilizing fluorescence fluctuations at time t about the mean, represented in Equation 2.1 where <F> is the time-average of F(t).[2-4] These

$$\delta F(t) = F(t) - \langle F \rangle \qquad \text{Equation 2.1}$$

fluctuations are used in the definition of an autocorrelation function, shown in Equation 2.2. The fluorescence autocorrelation the product of the fluorescence fluctuations with

$$G_2(\tau) = \frac{\langle \delta F(t) \cdot \delta F(t+\tau) \rangle}{\langle F(t) \rangle^2} \qquad \text{Equation 2.2}$$

itself as a function of time delay, τ, and thus has the greatest similarity at zero delay (along with maximal noise). As the time delay is increased, fluorescence fluctuations become less similar as a result of underlying physical processes such as photophysical blinking and diffusion through the excitation volume.

Correlation functions performed on photon arrival trajectories naturally average over many individual events and report on characteristic timescales of the system under

study. As with any FCS experiment, fluctuations resulting from individual molecules must remain larger than those arising from background sources, mandating relatively low concentrations, bright analyte molecules, stable lasers, sensitive detectors, and very low obscuring background. In the limit of zero background, the number of molecules in the excitation volume is determined using an autocorrelation fit to a standard diffusing molecule model, shown in Equation 2.3 for a three dimensional Gaussian function with molecular diffusion:[4]

$$G_2(\tau) = 1 + \frac{1}{N} \cdot \frac{1}{\left(1 + \frac{4\,D\,\tau}{{w_{xy}}^2}\right)} \cdot \frac{1}{\sqrt{1 + \frac{4\,D\,\tau}{{w_z}^2}}} \qquad \text{Equation 2.3}$$

in which τ is the delay, N is the number of molecules, D is the diffusion coefficient and w_{xy}, w_z are the excitation volume dimensions.[5] As dynamics are not synchronized, contrast increases with decreasing numbers of molecules contributing to the overall signal. Signal to noise of the correlation curve, however, increases with increased fluorescence brightness of the sample. Thus, crucial parameters include molecular brightness for good visibility at low analyte concentration and maintaining very low obscuring background fluorescence.[5]

In the case of blinking, fluorescent on and off times may be fit by Equation 2.4, where τ_c is the characteristic blinking time, and A and B are constants related to τ_c via Equation 2.5 and Equation 2.6:[2]

$$G_2(\tau) = 1 + \frac{1}{N} \frac{1}{\left(1 + \frac{4\,D\,\tau}{{w_{xy}}^2}\right)} \frac{1}{\sqrt{1 + \frac{4\,D\,\tau}{{w_z}^2}}} \left(A + B\,e^{\frac{\tau}{\tau_c}}\right) \qquad \text{Equation 2.4}$$

where the photophysical on and off times τ_{on} and τ_{off} are related to τ_c and constants A and B via:

$$\frac{1}{\tau_c} = \frac{1}{\tau_{on}} + \frac{1}{\tau_{off}} \quad \text{Equation 2.5}$$

$$\frac{A}{B} = \frac{\tau_{on}}{\tau_{off}} \quad \text{Equation 2.6}$$

2.4.2 Experimental FCS

Using a fluorescence setup, extremely low concentrations of solutions were observed in minimal ambient light conditions (1-300 cts/s when primary excitation is blocked). Extremely dilute solutions (pM to nM) are important for significant correlation amplitudes as fewer fluorophores generate greater fluctuations, greater amplitude in the correlation function, and subsequently better parameter extraction as a result of fitting. FCS correlations were fit to Equation 2.3 for non-blinking fluorophores.

FCS combined with dual excitation were collected via two overlapped lasers, where the beam width of the secondary laser is smaller than the primary laser which is aligned to backfill the objective to minimize excitation volume. This way the secondary laser has a larger excitation volume and effectively depopulates any thermally excited states before they enter the excitation volume of the primary laser. Importantly, secondary excitation is passed through an electro-optical modulator and then an optical fiber. The electro-optical modulator varies the intensity of passed secondary intensity, and the fiber significantly increases the contrast between ‘on’ and ‘off’ states. The combination of both the well-aligned electro-optical modulator and optical fiber (~80% power aligned) allows one to attain a contrast ratio of 10,000:1 or greater. A schematic of the alignment is shown in Figure 2.3.

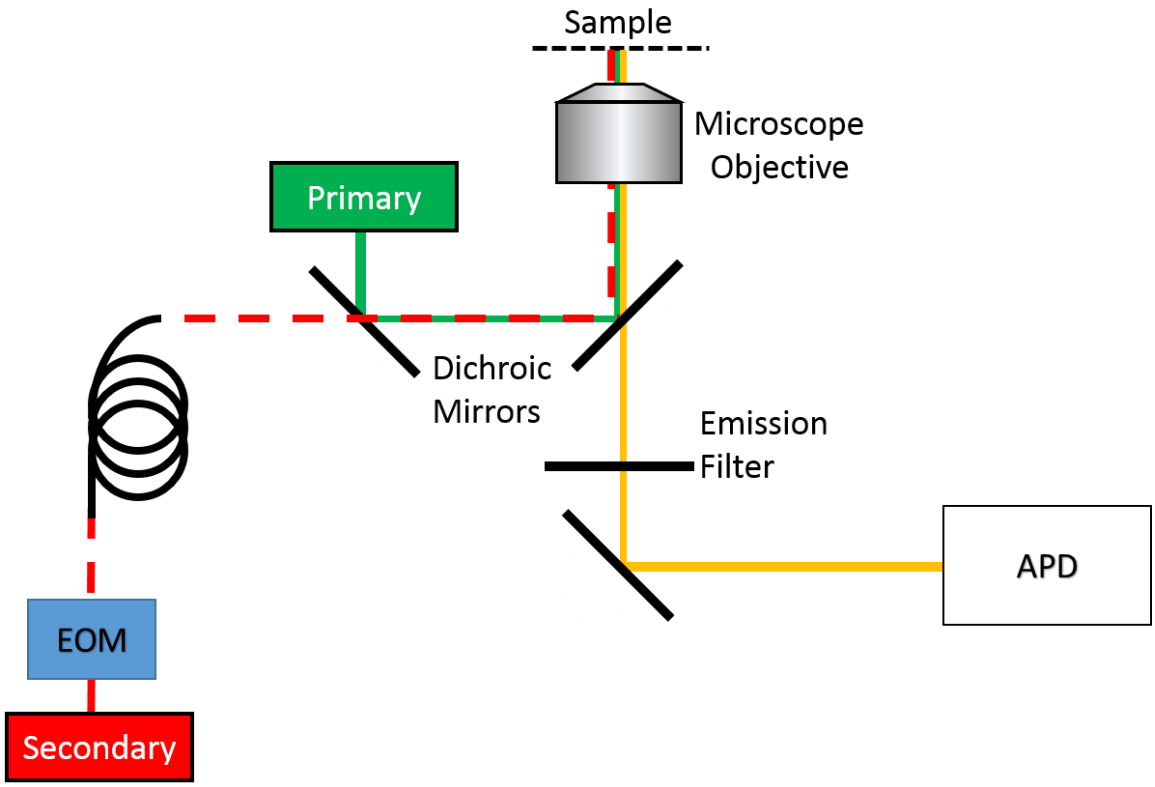

Figure 2.3. Schematic of SAFIRe-FCS subtraction alignment. Much like the fluorescence experiment, a primary laser is aligned into a microscope and fluorescence is collected on an APD. The addition of a secondary excitation is aligned first through an electro-optical modulator and then an optical fiber before being overlapped with the primary excitation. The combination of the electro-optical modulator and fiber maximizes the contrast of 'on' and 'off' modulated intensity.

2.5 Pulse – Continuous Wave (CW) Experiments

Pulse – CW experiments were conducted via a pulsed diode laser. For 500 kHz repetition rates and above, the pulse repetition was simply recorded in the 'sync' port on the photon counting card (Figure 2.4). Lower frequency repetition rates were recorded by collecting the pulses as 'photons' on a separate channel via a Becker-Hickl HRT-41 router connected to a Becker-Hickl SPC 630 photon counting board operated in reverse stop/start and FIFO modes (Figure 2.5).

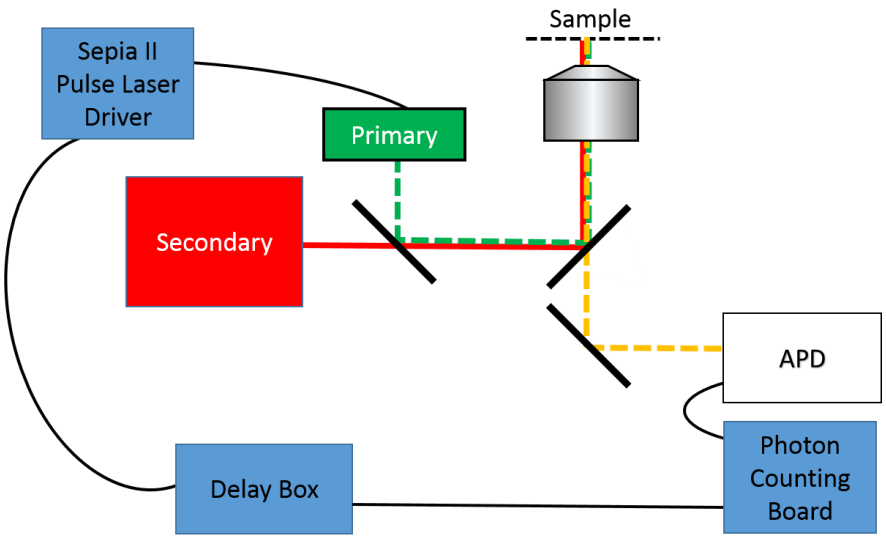

Figure 2.4. Schematic of fast (>200 kHz) pulse-CW experiments where a primary diode laser synced via a delay box to a photon counting board.

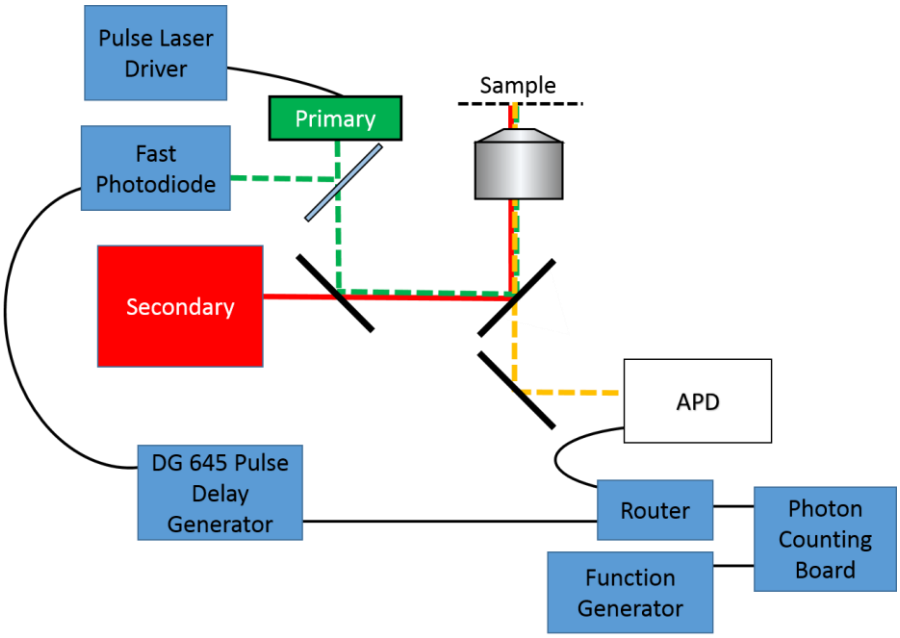

Figure 2.5. Schematic of slow (<200 kHz) pulse-CW experiments where a fast diode records the output from a 10 kHz diode laser and is collected along with fluorescence via a router which assigns a channel to APD vs photodiode pulses.

Subsequent analysis was used to determine the time delay between each sync 'photon' and all other collected fluorescence.

2.6 Pulse-Pulse Experiments

Pulse-pulse experiments were also conducted in two time schemes – 10 MHz and 10 kHz, and were set up as shown in Figure 2.6 and Figure 2.7. Due to the drastic difference in time scales, two digital delay generators (DG 645 and DG 535) were employed in place of delay boxes to properly delay pulses for the 200 kHz modulation.

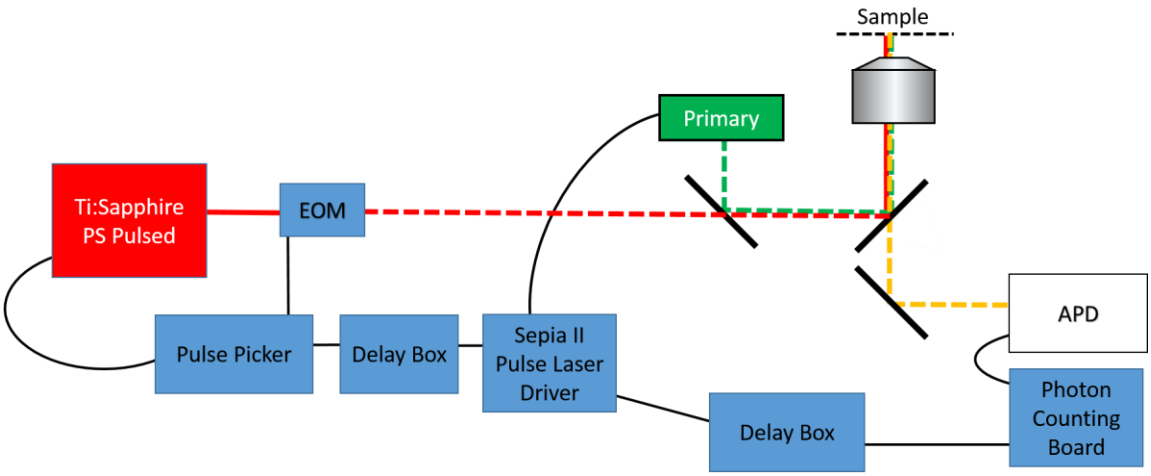

Figure 2.6. Schematic of fast (5 MHz) pulse-pulse experiments. The 80 MHz Ti:Sapphire is pulse picked and used to trigger a pulse laser deriver. Variable delay boxes (0-32 ns) are used to precisely control timing of sync and primary pulses.

2.7 Stochastic Optical Fluctuation Imaging

Glass substrates used in Stochastic Optical Fluctuation Imaging (SOFI) experiments were prepared first by a 2+ hour soak in acetone, followed by a rinse with DI H_2O and subsequent plasma cleaning (Harrick Plasma, PDC-32G) for 15 seconds. All fluorophores were diluted in a 20% (w/v) PVA and deposited on glass coverslips by spin coating at 2500 RPM for 50 seconds.

A 2D or 3D piezoelectric stage was controlled by in-house LabView 8.6 software that recorded fluorescence and position. A LabView PCI-6602 Timer Card with a BNC-2120 breakout box collected fluorescence and the stage was controlled via closed-loop USB. MatLab version r2013a was used to analyze and display data.

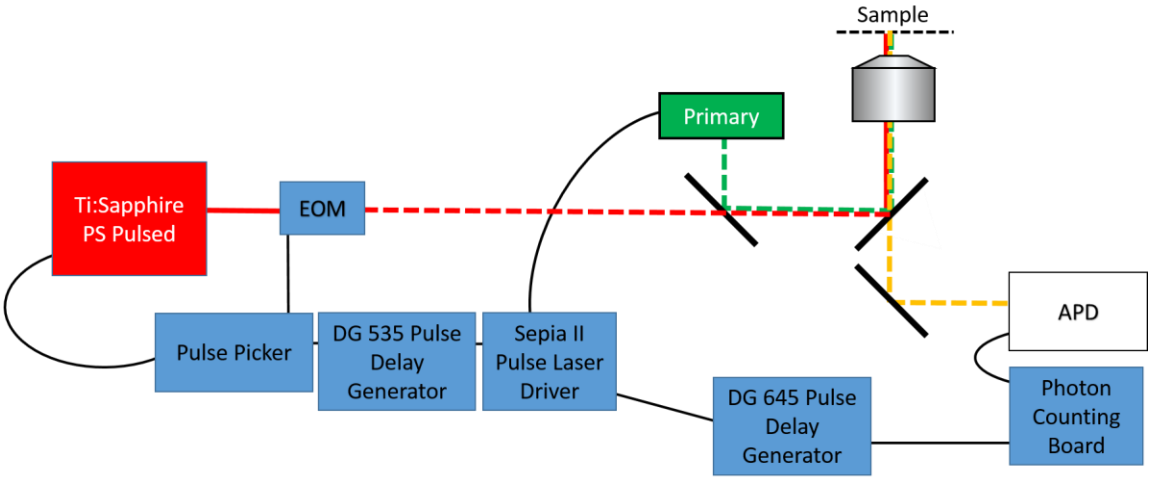

Figure 2.7. Schematic of slow pulse-pulse experiments where the delay boxes in Figure 6 are replaced with digital delay generators. Due to the 200 kHz rep rate, the sync port on the counting board could be used directly.

All simulations were written in MatLab versions r2013a - 2015a. Care was taken to vectorize the fluorescence trajectories, incorporating sequential loops only to determine the occurrence of non-overlapping photophysical dark states. Once optimizations were made via vectorization, the simulations were parallelized and run on PACE cluster resources (http://www.pace.gatech.edu).

2.8 Single Particle Tracking

Samples used for single particle tracking were either aqueous or PEG-600 (carbowax) solutions of crimson (625 ex/ 645 em) beads either 200 nm or 20 nm in diameter (FluoSpheres, ThermoFisher).

Immobilized samples were prepared with a 3.8 pM solution of 250 nm diameter carboxylate-functionalized fluorescent polystyrene beads (Invitrogen, Grand Island, NY) in a 1:10 (w/v) solution of PVA and water. The mixture was then spin-coated onto a glass coverslip at 5500 rpm for 50 s to immobilize the beads in a dry PVA matrix.

Samples used for tracking were sandwiched between two coverslips via two layers of double-sided film tape. The coverslips were then adhered to the microscope stage via double sided tape. PEG solvated samples were prepared by 1:1000 (v/v) dilutions of polystyrene bead stock solutions (2% solids) in PEG 400 solutions for a final concentration of 3.8 pM. Beads were first located on a CCD and subsequent fluorescence collected by the microscope was then directed to an APD via a microscope viewport adjustment knob. Aqueous samples were prepared the same as PEG samples.

2.9 Data Analysis

Data analysis was performed primarily with MatLab (versions r2011a – r2015a), along with the C programming language and Origin software (version 8.5). Autocorrelations were calculated using an in-house implementation of a photon-by-photon method or convolution.[6]

2.9.1 Fluorescence Enhancement

Enhancement was determined via Equation 2.7, where I_{dl} is the dual laser fluorescence intensity and I_{sl} is the single laser fluorescence intensity.[7] However, in practice, a Fourier transform may be used. Equation 2.8 is the enhancement of sin wave modulation, where $FT_{sin,modFreq}$ is the amplitude of the discrete fast Fourier transform at the modulation frequency and FT_0 is the 0 Hz amplitude or offset amplitude. The factors of 2 on the enhancement take into account the symmetric FFT, where only one half is considered, and thus must be multiplied by 2. FT_0 is unique and not multiplied by 2. Equation 2.9 shows the enhancement of square wave modulation, where $FT_{sq,modFreq}$ is the amplitude at the square wave modulation frequency. The factor of $\pi/2$ ($2 \times \pi/4$) in the square wave is a result of the infinite sum of odd harmonic frequencies required to form a square wave.[8]

$$Enh = \frac{I_{dl} - I_{sl}}{I_{sl}} \qquad \text{Equation 2.7}$$

$$Enh = \frac{2\,(2\,FT_{sin,modFreq})}{FT_0 - 2\,FT_{sin,modFreq}}$$ Equation 2.8

$$Enh = \frac{2\,(\frac{\pi}{2}\,FT_{sq,modFreq})}{FT_0 - \frac{\pi}{2}\,FT_{sq,modFreq}}$$ Equation 2.9

2.9.2 Diffusion Coefficient for Tracking

As a means of reporting the capabilities of a tracking instrument, a diffusion coefficient provides an experimentally relevant figure of merit. Diffusion coefficients can be used to characterize the diffusive motions present in a sample, where higher diffusion coefficients represent faster diffusion. Applications of tracking are limited by the range of diffusion coefficients an instrument can follow. Instruments capable of measuring higher diffusion coefficients have wider application because the tracking of nonmoving particles is trivial. Among the highest reported diffusion coefficients for a single tracked particle is 20 $\mu m^2/s$, corresponding to a single 20 nm diameter sphere in water.[9]

Diffusion coefficients can be experimentally determined from a particle trajectory using Equation 2.10. In this equation, the mean square displacement (MSD), represented by $\langle|r(t)-r(0)|^2\rangle$, is calculated from a series of positions in time, r(t), and scaled against the number of dimensions n and time t. While Equation 2.10 represents the diffusion coefficient as a function of time, the diffusion coefficients can also be obtained by plotting MSD/2n versus time and fitting the slope. Diffusion coefficients for particles as a function of time could give insight into the dynamics of either particle diffusion or instrumental response and are discussed in Section 6.6.1.

$$D(t) = lim_{t\to\infty}\frac{1}{2\,n\,t}\langle|r(t) - r(0)|^2\rangle$$ Equation 2.10

As a method for checking experimental work, diffusion coefficients can also be calculated by the Stokes-Einstein relation which is the ratio of the available thermal energy to the frictional forces present. The Stokes-Einstein relation is shown in Equation 2.11 where k_B is the Boltzmann constant, T is temperature (in Kelvin), η is the solution viscosity (Pa·s) and r is the particle radius (m). The Stokes-Einstein equation assumes

$$D = \frac{k_B T}{6 \pi \eta r} \qquad \text{Equation 2.11}$$

spherically symmetric particles and solution viscosities that are temperature independent. Despite these assumptions it is still useful as a way of checking experimental results, and will be used to approximate experimental diffusion coefficients in the thesis research results to follow.

2.10 References

1. Richards, C. I.; Choi, S.; Hsiang, J.-C.; Antoku, Y.; Vosch, T.; Bongiorno, A.; Tzeng, Y.-L.; Dickson, R. M. "Oligonucleotide-stabilized Ag nanocluster fluorophores." *Journal of the American Chemical Society*, **2008**, *130*, 5038-5039.

2. Vosch, T.; Antoku, Y.; Hsiang, J.-C.; Richards, C. I.; Gonzalez, J. I.; Dickson, R. M. "Strongly emissive individual DNA-encapsulated Ag nanoclusters as single-molecule fluorophores." *Proceedings of the National Academy of Sciences of the United States of America*, **2007**, *104*, 12616-12621.

3. Elson, E.; Magde, D. "Fluorescence correlation spectroscopy. I. Conceptual basis and theory." *Biopolymers*, **1974**, *13*, 1-28.

4. Schwille, P.; Heinze, K. G.; Dittrich, P.; Haustein, E. In *Biomedical Optical Imaging*; Fujimoto, J. G. F., Daniel L., Ed.; Oxford University Press: New York, NY, 2009.

5. Biophysical journalApplied Physics BElson, Elliot L. "Fluorescence Correlation Spectroscopy: Past, Present, Future." *Biophysical Journal*, **2011**, *101*, 2855-2870.

6. Laurence, T. A.; Fore, S.; Huser, T. "Fast, flexible algorithm for calculating photon correlations." *Optics Letters,* **2006**, *31,* 829-829.

7. Petty, J. T.; Fan, C.; Story, S. P.; Sengupta, B.; Sartin, M.; Hsiang, J. C.; Perry, J. W.; Dickson, R. M. "Optically enhanced, near-IR, silver cluster emission altered by single base changes in the DNA template." *Journal of Physical Chemistry B,* **2011**, *115,* 7996-8003.

8. Sabah, N. H. *Electronic Circuits and Signals*; CRC Press: Boca Raton, FL, 2007.

9. McHale, K.; Berglund, A. J.; Mabuchi, H. "Quantum Dot Photon Statistics Measured by Three-Dimensional Particle Tracking." *Nano Letters,* **2007**, *7*, 3535-3539.

CHAPTER 3

SAFIRe-FCS

3.1 Introduction

Endogenous fluorescent background, present in nearly all biological fluorescence imaging, obscures signals of interest. Improvements in sensitivity or the ratio of signal to noise is thus important for biological study. The presence of background has forced the development of brighter and wavelength-shifted fluorescent probes such that brighter signals are obtained.[1-3] However, the brightness is limited by the number of electrons involved in the optical transition and organic molecules routinely approach this oscillator strength limit.[4] As a result, further gains in sensitivity are likely to come from background reduction.

Separate from passive background reduction, actively manipulating fluorescent signals enables the selective recovery of signal even in cases where the background is two orders of magnitude greater than signal of interest. Originally demonstrated on Ag-DNA clusters, Synchronously Amplified Fluorescence Intensity Recovery (SAFIRe) is a fluorescence modulation technique that uses an intensity-modulated, lower energy secondary laser to reversibly depopulate photon-generated dark states, subsequently repopulating the ground state in a reversible manner.[5-8] As a result, an external modulation waveform is encoded only on the analyte fluorescence, which can be decoded to recover emission from the emitters separately from the endogenous background.[9]

SAFIRe is effective both for single molecule and bulk samples and is capable of recovering relative concentrations of modulation-sensitive fluorophore signals in high background environments. In contrast, fluorescence correlation spectroscopy (FCS) typically relies on very low concentrations (nM-fM) to observe fluorescence intensity

fluctuations arising from physical processes such as diffusion, concentration and photophysical dark state dynamics.[10,11] One of the most significant challenges to FCS in biological environments is background fluorescence. Even with weak background, the true number of molecules present in the focal volume is not directly recoverable as fluorescent fluctuations arise from both signal and background emitters.[11,12] Thus, optical modulation of Ag-DNA clusters is utilized to demonstrate novel bulk spectroscopic methods to improve one laser FCS to quantitatively recover signal concentration and diffusion dynamics in high background environments.

3.2 Theory

Representing the signal S(t) as S, the obscuring background B(t) as B, there is a relative enhancement factor, c, of the signal as a result of secondary co-illumination (cS). Because the secondary laser is longer wavelength than the collected emission, this enhancement does not affect the non-modulated background, B, which is always present. This leads to two regimes of signal: S+B and cS+B, resulting from single and dual excitation, respectively. The relative enhancement, c, must be greater than or equal to one, where a value of c equal to one corresponds to zero enhancement over primary excitation alone. Because, on average, the background is the same in the two halves of the modulation period, one can use the fact that correlations average data to mathematically extract the signal of interest in FCS. By splitting the intensity trajectory to yield two parallel trajectories consisting of 1) the photons collected with dual excitation and 2) those collected with primary-only excitation, the traces can be processed to extract the pure signal correlation curve without background contributions, according to Equation 3.1:

$$(cS+B)*(cS+B)+(S+B)*(S+B)+(cS+B)*(S+B)+(S+B)*(cS+B) = (c-1)^2(S*S) \quad \text{Equation 3.1}$$

where * indicates a correlation integral and all correlations must remain unnormalized until the final result is obtained.

With sufficient averaging, the correlation subtraction in Equation 3.1 recovers the true autocorrelation curve of the background subtracted signal of interest. Because photons are separated from the original time trace, Nyquist sampling dictates the fastest time that can be probed in the correlation-subtracted curve to be half the modulation period. Because this frequency is still much faster than that of diffusion through the focal volume, fitting the recovered background subtracted signal correlation to Equation 2.10 then allows for extraction of the number of molecules and diffusion time.

3.3 Ag-DNA Cluster Fluorophores

Previously reported photostable Ag-DNA clusters exhibit fluorescence with blinking on μs lifetimes, which significantly decrease when a second, lower energy/ longer wavelength excitation is applied (680-950 nm).[5,7,9,13,14] To confirm the loss of μs blinking as a result of long wavelength excitation, we compare the FCS measurements under conditions of single and dual excitation of shorter (594 and 642 nm wavelengths for 630 nm and 710 nm emitters, respectively) both with and without 803 nm co-illumination (Figure 3.1). This μs reduction in blinking suggests depopulation of a nonemissive dark state as a result of secondary, long wavelength irradiation, consistent with previously reported fluorescence enhancement.[5,15]

For both 630 nm and 710 nm emitting Ag-DNA clusters, primary excitation yields bright fluorescence while simultaneously shifting the population to the sub-100 ms long-lived dark state. Co-illumination with longer wavelengths repopulates the ground state faster than the dark state naturally decays to increase steady-state emission. Thus, all clusters exhibit enhanced fluorescence under secondary co-illumination but with varying degrees resulting from differences in steady-state dark state populations. The combined excitation of a 643 nm 10 kHz pulsed laser with an 803 nm CW yielded a fluorescence

A B

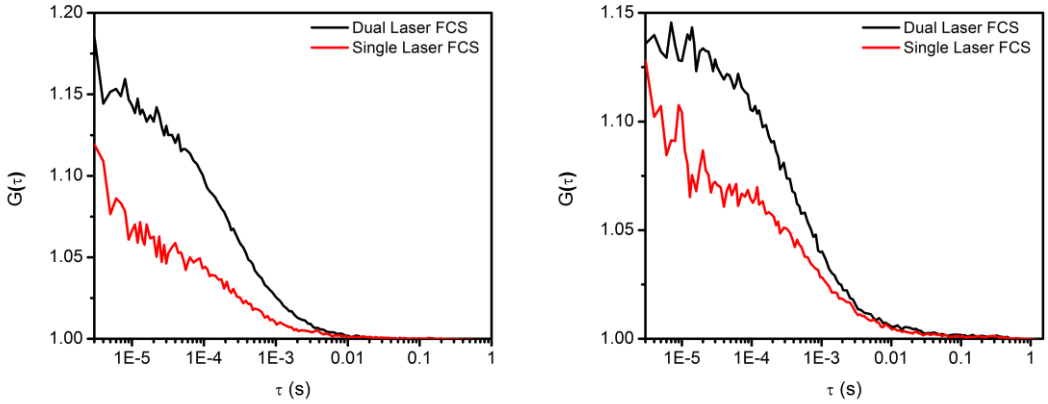

Figure 3.1. Autocorrelations of fluorescence from both single (red) and dual (black) illumination of (A) 630 nm emitters and (B) 710 nm emitters. FCS from primary only excitation is shown in red while FCS from dual excitation is shown in black, demonstrating the loss of µs blinking in the fluorescence as a result of secondary excitation. Samples were illuminated using a 400 W/cm^2 594 nm primary excitation source with and without 130 kW/cm^2 803 nm co-illumination and (B) 1.4 kW/cm^2 594 nm with and without 50 kW/cm^2 800nm co-illumination.

enhancement of ~10% in aqueous 710 nm emitters. By comparison, a 630 nm emitter exhibits a significantly higher aqueous enhancement (~50%), with specific photophysical characteristics listed in Table 3.1.

Table 3.1. Photophysical properties for 630 nm Ag-DNA clusters

Emisssion (nm)	τ_{fl}, ns	Φ_{FL}	ε, 10^5 $M^{-1}cm^{-1}$	τ_{on}, µs	τ_{off}, µs
630	2.16 ± 0.01	0.18 ± 0.03	2.6 ± 0.1	5.9 ± 0.4	10.9 ± 0.7

Our group has previously proposed a photophysical model for Ag-DNA enhancement using a three state system comprised of a ground state, emissive state, and dark state.[5,16-18] The photophysical on and off times (residence time in emissive and dark manifolds, respectively) determine the maximum optical modulation frequency as steady-

state populations must be established during a single modulation cycle. The high intersystem crossing rate, k_{isc}, enables Ag-DNA cluster steady-state populations to be established very quickly, allowing a wide range of modulation cycles to be utilized including those much faster (100 kHz) and much slower (1 Hz) than the diffusion time.

3.4 SAFIRe-FCS

Fluorescence was recorded in a solution of equal parts 630 nm Ag-DNA cluster and Texas Red under co-illumination of 594 nm continuous wave (CW) and modulated intensity 805 nm CW excitation (100kHz or 1Hz). The externally applied square-wave modulation period defines the width of the histogram window, with the secondary laser illuminating the sample for only half the period. The histogram exhibits two regimes – higher fluorescence intensity with secondary laser on, and lower fluorescence intensity with secondary laser off (Figure 3.2A and Figure 3.2As the secondary laser is much longer wavelength (805 nm) than the collected emission (630 nm), the non-modulated background is constant (Poisson distributed) throughout the entire microtime window. At modulation frequencies that are high relative to the diffusion rate, the same molecules are probed as they have had insufficient time to diffuse out of the focal volume during the modulation period.

Figure 3.3 demonstrates the recovery of 630 nm Ag-DNA cluster signals from Texas Red background. Correlation subtraction according to Equation 3.1 (Figure 3.2C and Figure 3.2D) reveals a higher correlation amplitude than present in the raw FCS curve. The higher resulting correlation amplitude can be fit to Equation 3.1 to extract only the 630 Ag-DNA clusters within the Texas Red background.

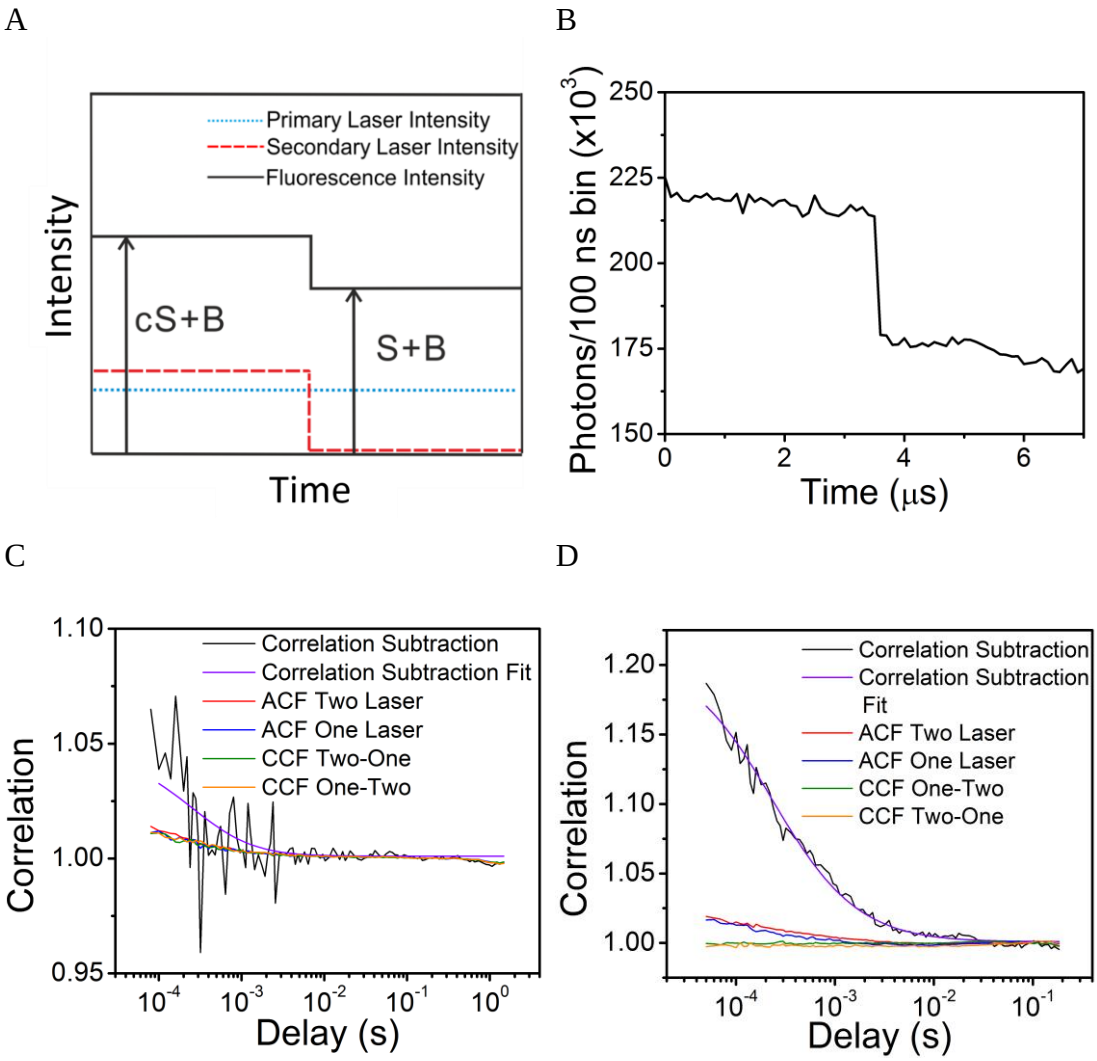

Figure 3.2. Correlation subtraction of modulated 630 nm emitters with Texas Red Background at concentrations such that they both exhibit equal fluorescence, illuminated with 594 nm primary and 805 nm secondary laser intensities of 400 W/cm2 and 70 kW/cm2, respectively, in an excitation volume of ~5x10-17 m3. (A) Schematic of the modulation period (histogram) for recovering concentrations. The primary excitation source is a constant intensity CW with modulated secondary intensity, leading to a modulated fluorescence signal. (B) Experimental microtime window of 100 kHz modulation cycle. (C) 100 kHz modulated fluorescence data from (B) is divided into photons corresponding to single and dual excitation and correlations of all possible combinations are performed. The correlation subtraction is also shown, as determined from Equation 3.1, along with fit to Equation 2.10. (D) Correlations pertaining to 1 Hz modulation of the same sample along with a fit to Equation 2.10.

3.5 High Frequency SAFIRe-FCS

In principle, correlation subtraction works best at very high modulation frequencies. In this regime, the molecules generating background and those giving signal and enhancement have not diffused out of the laser focus even after several modulation cycles. Thus, fluorescence fluctuations due to diffusing individual molecules can be quantitatively averaged and subtracted out of the resulting correlations. In practice, however, such high modulation frequencies require very high emission rates for good signal to noise. For high-frequency modulation, the photon count rate is divided by two as traces are separated into one laser and two laser intensity trajectories. Because signal to noise in correlation functions at a given delay scales with the square of the count rate, this count rate reduction through trace separation, coupled with the multiple operations on the auto and cross-correlations that need to be performed, further increase noise in the recovered correlation. While a unique aspect of these Ag-DNA cluster emitters is their ability to be optically modulated at high frequencies while maintaining large modulation depths, only a limited number of fluorophores exhibit the ability to rapidly establish optically sensitive steady-state populations that may be depopulated via long wavelength excitation.

3.6 Low Frequency SAFIRe-FCS

Low frequency modulation both complements and offers advantages over high frequency modulation-based signal extraction (Figure 3.2). For modulation at 1 Hz, photon arrival trajectories of each half period are correlated and combined according to Equation 3.1 to recover the background-subtracted correlation, S*S. These subtracted correlations can then be averaged over the many modulation cycles, further reducing shot noise contributions.

Sensitivity in correlation signals scales with the square of the photon count rate. Unlike high frequency SAFIRe-FCS, low frequency SAFIRe-FCS does not reduce

sensitivity by reducing the photon count rate prior to calculating correlation functions. Additionally, no additional Nyquist sampling constraints are imposed when separating dual and single-laser excitation traces. Thus, low frequency SAFIRe-FCS has higher sensitivity and readily preserves the faster dark state timescales in correlation subtractions. Only the long time correlations are sacrificed, but are much longer than the diffusion time and thus no diffusive information is lost. As with the high frequency modulation, diffusion times are readily recovered, but fluorescence fluctuations due to

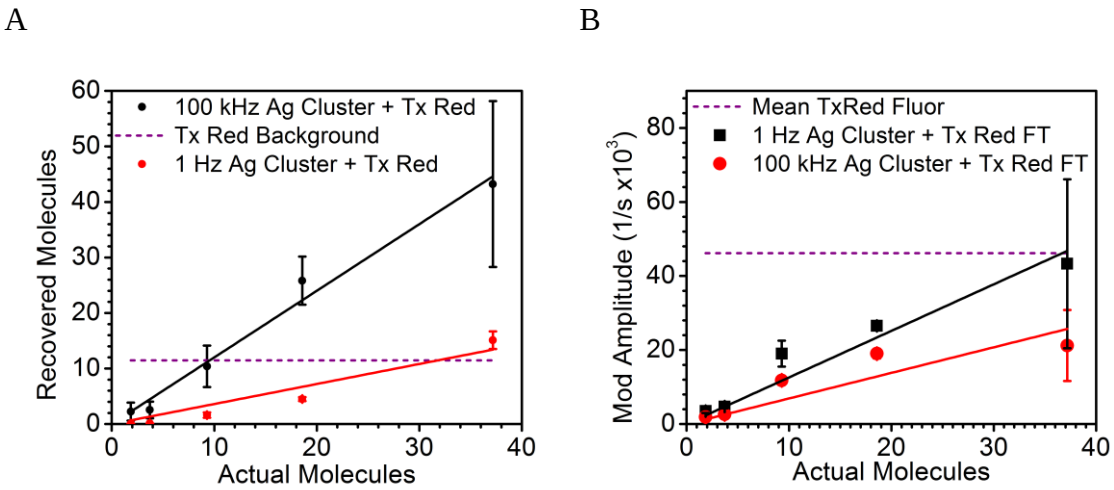

Figure 3.3. A) Plot of actual concentration vs correlation subtraction concentration at 100 kHz and 1 Hz modulation frequencies for 630 nm emitters with Texas Red background, illuminated with 594 nm primary and 805 nm secondary laser intensities of 400 W/cm2 and 70 kW/cm2, respectively. B) Fourier Transform Concentration recovery of 630 nm emitters with Texas Red background for the same experiments.

diffusing individual molecules may not be as effectively recovered as with high-frequency modulation. By using sufficiently long periods to average over background concentration fluctuations, improved averaging and subtractions are likely to be obtained but background may not be quantitatively removed using low-frequency modulation. This is evident in the different in correlation amplitudes in Figure 3.2D and molecule number recovery in Figure 3.3

Importantly, at low modulation frequencies, the number of molecules recovered with correlation subtraction is approximately equal to the difference between single and

dual-laser autocorrelations, shown in Figure 3.2C and Figure 3.2D. In other words, the cross correlations between enhanced and non-enhanced regions contribute less to the subtraction of background fluctuations at low modulation frequencies. The contrast upon correlation subtraction results from the increased signal with dual laser excitation over that with primary laser excitation alone, enabling preferential recovery of only the modulatable molecule signals, but the background fluctuations are not as effectively subtracted as with high frequency modulation. Contrast in the recovered correlation results from the difference in signal intensities between one and two laser excitation. However, since the same molecules are not present in both one and two laser excitation of low frequency SAFIRe-FCS, they are not represented in the cross-correlations as effectively. This suggests that while low frequency modulation removes background, the cross correlations between enhanced and non-enhanced signals are low, indicating that additional calibration will be needed to determine the correct analyte molecule concentration in solution.

3.7 Fourier Transform (FT) Concentration Recovery

Although Equation 3.1 is useful for recovering modulated fluorophore correlation curves with reduced background, the practical challenges in subtracting background at the different timescales suggests a simpler approach. As the auto and cross correlations are related to Fourier transforms (FTs) by the convolution theorem, one can extract the number of analyte molecules from the FT amplitude at the modulation frequency. We have shown that this amplitude scales linearly with the total number of modulated molecules and is shifted to its own unique detection frequency, free from obscuring background signals.[5-9,19-21] While this amplitude is linear in the number of molecules, the slope of FT amplitude vs. concentration of modulated species is a product of many photophysical and experimental parameters. Thus, accurate numbers of molecules can

only be obtained from the FT amplitude if calibrated by the correlation subtracted SAFIRe-FCS or a predetermined calibration curve obtained under identical conditions.

3.8 Comparison of High Frequency, Low Frequency, and FT Recovery

By modulating at 1 Hz, photons were collected for 0.5 seconds with dual CW excitation and 0.5 seconds with primary only excitation. Enough photons are collected to enable calculation of entire correlation functions within each half-second period. Clearly, the 1 Hz recoveries drastically improve correlation contrast through correlation subtraction, since low modulation frequency count rates are not divided as they are at high modulation frequencies. The amplitudes of the cross correlations between modulated and unmodulated halves of the modulation period are much lower as the background in each half-period is not exactly identical as it is at high frequencies. Thus, 1 Hz data may not quantitatively recover concentrations, but it does demonstrate the utility of correlation subtractions to remove background signals.

Because SAFIRe induces high fluorescence enhancement, enhancement photons are synchronized with the secondary laser modulation waveform. Thus, for any specific modulation frequency and excitation conditions, a calibration of FT amplitude to known concentration (including extrapolation of FT amplitude to zero concentration) provides a convenient methodology for relating modulation-dependent fluorescence signals to true concentration in complex environments. When the only varying quantity is concentration, the FT amplitude at the modulation frequency is directly proportional to analyte concentration (Figure 3.3B), providing a calibration curve to determine concentration from modulated signals. Thus, the combination of correlation subtraction at high and low frequencies, coupled with calibrated FT amplitude enables extraction of analyte concentration for fluorophores with optically modulated dark states at a wide range of modulation timescales.

3.9 Conclusions

Biologically relevant environments contribute significant endogenous background signals to fluorescence, providing challenges to sensitive techniques such as FCS. However, modulation sensitive fluorophores, such Ag nanodots used with SAFIRe, provide a means of signal recovery amidst high background and is applicable to FCS through correlation subtractions. Ag nanodots provide excellent brightness in both linear and multiphoton fluorescence, but it is their dark states that enable selective recovery of their emission without recovering background.[5,7,9,20,22,23] Using new SAFIRe-FCS subtractions on fast and slow timescales, the highly populated dark states can be optically depopulated with long wavelength co-illumination to repopulate the fluorescent manifold of states. Modulating this secondary laser modulates recovered fluorescence, shifting Ag nanodot emission signals to a unique detection frequency. Modulation frequency is limited by the time required to build up steady-state populations, which is largely governed by the Ag nanodot dark state lifetime.[6,7,13] SAFIRe-FCS with modulation much faster than the diffusional transit time in an FCS geometry provides a means for concentration recovery through correlation subtraction of enhanced and unenhanced portions of the modulation cycle. Lower frequency modulation provides incomplete background suppression, as subtractions are on timescales significantly longer than diffusion, and thus not performed on the same analyte and background emitters. In both low and high modulation frequencies, the Fourier amplitude provides a linear relationship between concentration and correlation subtraction, making it possible to quantitatively recover Ag nanodot concentrations from high backgrounds in FCS geometries. SAFIRe-FCS should have direct applications to FCS studies in biological systems, making these small (~5nm hydrodynamic diameter) sub-10 atom Ag cluster fluorophores useful labels to observe biological interactions in highly autofluorescent environments or in multiplexed assays.

3.10 References

1. Altman, R. B.; Zheng, Q.; Zhou, Z.; Terry, D. S.; Warren, J. D.; Blanchard, S. C. "Enhanced photostability of cyanine fluorophores across the visible spectrum." *Nature Methods*, **2012**, *9*, 428-429.

2. Zhang, X.; Xiao, Y.; Qi, J.; Qu, J.; Kim, B.; Yue, X.; Belfield, K. D. "Long-Wavelength, Photostable, Two-Photon Excitable BODIPY Fluorophores Readily Modifiable for Molecular Probes." *Journal of Organic Chemistry*, **2013**, *78*, 9153-9160.

3. Wu, X.; Zhu, W. "Stability enhancement of fluorophores for lighting up practical application in bioimaging." *Chemical Society Reviews*, **2015**, *44*, 4179-4184.

4. Zheng, Q.; Juette, M. F.; Jockusch, S.; Wasserman, M. R.; Zhou, Z.; Altman, R. B.; Blanchard, S. C. "Ultra-stable organic fluorophores for single-molecule research." *Chemical Society Reviews*, **2014**, *43*, 1044-1056.

5. Richards, C. I.; Hsiang, J.-C.; Dickson, R. M. "Synchronously amplified fluorescence image recovery (SAFIRe)." *The Journal of Physical Chemistry B*, **2010**, *114*, 660-665.

6. Fan, C.; Hsiang, J.-C.; Dickson, R. M. "Optical Modulation and Selective Recovery of Cy5 Fluorescence." *ChemPhysChem*, **2012**, *13*, 1023-1029.

7. Hsiang, J. C.; Jablonski, A. E.; Dickson, R. M. "Optically modulated fluorescence bioimaging: Visualizing obscured fluorophores in high background." *Accounts of Chemical Research*, **2014**, *47*, 1545-1554.

8. Chen, Y.-C.; Jablonski, A. E.; Issaeva, I.; Bourassa, D.; Hsiang, J.-C.; Fahrni, C. J.; Dickson, R. M. "Optically Modulated Photoswitchable Fluorescent Proteins Yield Improved Biological Imaging Sensitivity." *Journal of the American Chemical Society*, **2015**, 150924164102005-150924164102005.

9. Richards, C. I.; Hsiang, J.-C.; Senapati, D.; Patel, S.; Yu, J.; Vosch, T.; Dickson, R. M. "Optically Modulated Fluorophores for Selective Fluorescence Signal Recovery." *Journal of the American Chemical Society*, **2009**, *131*, 4619-4621.

10. Elson, E.; Magde, D. "Fluorescence correlation spectroscopy. I. Conceptual basis and theory." *Biopolymers*, **1974**, *13*, 1-28.

11. Biophysical journalApplied Physics BElson, Elliot L. "Fluorescence Correlation Spectroscopy: Past, Present, Future." *Biophysical Journal*, **2011**, *101*, 2855-2870.

12. Kim, S. A.; Heinze, K. G.; Schwille, P. "Fluorescence correlation spectroscopy in living cells." *Nature Methods*, **2007**, *4*, 963-973.

13. Vosch, T.; Antoku, Y.; Hsiang, J.-C.; Richards, C. I.; Gonzalez, J. I.; Dickson, R. M. "Strongly emissive individual DNA-encapsulated Ag nanoclusters as single-molecule fluorophores." *Proceedings of the National Academy of Sciences of the United States of America,* **2007**, *104*, 12616-12621.

14. Richards, C. I.; Choi, S.; Hsiang, J.-C.; Antoku, Y.; Vosch, T.; Bongiorno, A.; Tzeng, Y.-L.; Dickson, R. M. "Oligonucleotide-stabilized Ag nanocluster fluorophores." *Journal of the American Chemical Society*, **2008**, *130*, 5038-5039.

15. Patel, S. a.; Cozzuol, M.; Hales, J. M.; Richards, C. I.; Sartin, M.; Hsiang, J. C.; Vosch, T.; Perry, J. W.; Dickson, R. M. "Electron transfer-induced blinking in Ag nanodot fluorescence." *Journal of Physical Chemistry C,* **2009**, *113*, 20264-20270.

16. Petty, J. T.; Fan, C.; Story, S. P.; Sengupta, B.; St. John Iyer, A.; Prudowsky, Z.; Dickson, R. M. "DNA encapsulation of 10 silver atoms producing a bright, modulatable, near-infrared-emitting cluster." *Journal of Physical Chemistry Letters*, **2010**, *1*, 2524-2529.

17. Widengren, J.; Mets, U.; Rigler, R. "Fluorescence correlation spectroscopy of triplet states in solution: a theoretical and experimental study." *The Journal of Physical Chemistry,* **1995**, *99*, 13368-13379.

18. Lakowicz, J. R. *Principles of Fluorescence Spectroscopy*; Springer: New York, 2006.

19. Fan, C.; Hsiang, J.-C.; Jablonski, A. E.; Dickson, R. M. "All-optical fluorescence image recovery using modulated stimulated emission depletion." *Chemical Science*, **2011**, *2*, 1080-1080.

20. Petty, J. T.; Fan, C.; Story, S. P.; Sengupta, B.; Sartin, M.; Hsiang, J. C.; Perry, J. W.; Dickson, R. M. "Optically enhanced, near-IR, silver cluster emission altered by single base changes in the DNA template." *Journal of Physical Chemistry B,* **2011**, *115*, 7996-8003.

21. Jablonski, A. E.; Vegh, R. B.; Hsiang, J. C.; Bommarius, B.; Chen, Y. C.; Solntsev, K. M.; Bommarius, A. S.; Tolbert, L. M.; Dickson, R. M. "Optically modulatable blue fluorescent proteins." *Journal of the American Chemical Society*, **2013**, *135*, 16410-16417.

22. Petty, J. T.; Zheng, J.; Hud, N. V.; Dickson, R. M. "DNA-Templated Ag Nanocluster Formation." *Journal of the American Chemical Society,* **2004**, *126*, 5207-5212.

23. Patel, S. a.; Richards, C. I.; Hsiang, J.-C.; Dickson, R. M. "Water-soluble Ag nanoclusters exhibit strong two-photon-induced fluorescence." *Journal of the American Chemical Society*, **2008**, *130*, 11602-11603.

CHAPTER 4

SEQUENTIAL TWO-PHOTON FLUORESCENCE UPCONVERSION

4.1 Introduction

Endogenous background frequently obscures signals of interest when imaging biological samples with fluorescence microscopy.[1-3] Sensitivity, defined as the ratio of signal to noise, can be improved either by increasing signal or reducing noise. Significant efforts have been made towards increasing signal by improving fluorophore brightness, enhancing photostability, and wavelength-shifting fluorescence emission to portions of the spectrum that exhibit minimal overlap with biological background fluorescence.[4-8]

Efforts have also been made to reduce background and are the focus of this chapter. It is possible to reduce background through selective control and observation of analyte-specific fluorescence intensity changes. Specifically, dual excitation schemes comprised of a primary excitation that causes fluorescence and a secondary wavelength-separated excitation that modulates total fluorescence intensity have demonstrated all-optical control of analyte-specific fluorescence intensity.[9,10] Initially demonstrated in molecular photoswitch fluorophores, optical lock-in detection (OLID) demonstrated a reduction in background by cross correlating deterministic fluorescence fluctuations in cells with a known reference, thereby reducing background.[9,11] Additionally, in synchronously amplified fluorescence recovery (SAFIRe), optical modulation reversibly depopulates fluorophores otherwise trapped in μs-lived photophysical dark states, recovering ground state populations and subsequently increasing fluorescence. Analyzing the fluorescent signal at the modulation frequency permits recovery in the presence of

high background and is frequently accomplished through the use of Fourier transforms (FTs).[10,12-15] Such techniques provide a means to encode a time variant fluorescence intensity signal through secondary excitation which can be post-processed to extract analyte fluorescence amid background. In this chapter, the dual excitation process is considered as a sequential two-photon process comprised of primary excitation to an emissive state, relaxation into a dark state, and a secondary excitation out of the dark state. Additional background information on optical modulation is presented in Section 1.5.1

Aside from optical modulation, a complementary method to circumvent background is through the use of labels that exhibit significantly longer fluorescence lifetimes than background. In this technique, pulsed excitation is applied to fluorophores with long fluorescent lifetimes in the presence of background. The background fluorescence persists for relatively shorter time scales (~ns) while the analyte fluorescence is recorded beyond this time frame (<ms). By gating the collection of fluorescence beyond the fluorescence lifetime of the background, significant gains in sensitivity can be achieved. This has been demonstrated in lanthanide-based fluorescent probes, which exhibit lifetimes on the order of 1-10 ms.[16] Long lifetimes in lanthanides result from a combination of poor connections between ground and emissive states and the high refractive index of the surrounding chelator, molecular sensitizer, or other medium.[17,18] Application of pulsed excitation allows for the background, with shorter fluorescent lifetimes to first decay before the longer lived lanthanide fluorescence is recorded.[16,18-20] Repetitive pulses build fluorescence signals dominated by slowly decaying fluorescence that significantly reduces background.

In this chapter, sequential two-photon optical modulation processes in Ag-DNA clusters are combined with time-gated fluorescent lifetimes providing a near zero background method for obtaining fluorescence. Using pulsed primary excitation, secondary excitation induces luminescence during periods absent of primary excitation, significantly increasing sensitivity. Schemes for high-sensitivity signal extraction are devised using time-gating as the primary mechanism for background reduction.

Sequential two-photon upconversion was successfully applied to fluorescence correlation spectroscopy (FCS) measurements of Ag-DNA nanodots and is presented herein. In addition to FCS, two-photon fluorescence upconversion could be applied to a broad number of other techniques including fluorescence imaging and super-resolution provided that background fluorescence lifetimes are shorter than the optically sensitive analyte dark state lifetimes. Biological fluorescence imaging of single or multiple fluorophores is a feasible future application. One could also imagine applications involving the monitoring of the dark state lifetime as a function of probe environment, mapping lifetimes to chemical or physical processes in the immediate vicinity of the fluorophores. This technique is reliant on a set of photophysical conditions which are explained in the following section.

4.1.1 Photophysical Model for Sequential Upconversion

Transitions between photophysical states of modulated fluorophores can be explained in terms of a three state model comprised of ground, emissive, and non-emissive states.[4,19] Initial excitation would populate an excited fluorescent state with subsequent relaxation typically to the ground state directly. A small percentage relax into a non-emissive dark state. Previous work in our group has detailed a subset of

fluorophores in which long wavelength secondary excitation is absorbed by this dark state, causing rapid depopulation back to the ground state, which in turn increases the population of fluorophores available for subsequent excitation/fluorescent cycles.[10,13,21,22] As a result, the dual excitation process can be considered a sequential two-photon process, comprised of primary excitation, relaxation into a dark state, and a secondary excitation out of the dark state.

Interestingly, Ag-DNA probes emit fluorescence as a direct result of only secondary laser excitation immediately following a pulsed primary excitation. In other words, if the fluorophores are in a dark state, application of only long wavelength secondary excitation can repump the fluorophore directly back into an excited emissive state leading to additional fluorescence. This is a refinement of the general modulation model proposed by our group, where excitations out of a dark state were more generally classified as a rapid pathway to the ground state.[7,10,21] Here, we assign a direct transition between dark and excited fluorescent states as a result of secondary excitation (Figure 4.1, k_{32}). [21] As application of long wavelength secondary excitation alone does not cause fluorescence if the fluorophore is in the ground state, the secondary excitation must drive the fluorophore populations from a non-emissive dark state back into an excited emissive state with subsequent relaxations resulting in additional fluorescence (k_{21}).

This transition can be modelled in a photophysical transition rate matrix (Equation 4.1) modified from previously reported three state rate matrices.[23] Primary excitation, represented as k_{12}, populates the emissive state (S_1) via transitions from the ground state (S_0). Subsequent relaxations lead to fluorescence (k_{21}) and population of a non-emissive state (T, k_{23}) which then relaxes (k_{31}) after a time equal to $1/k_{31}$.

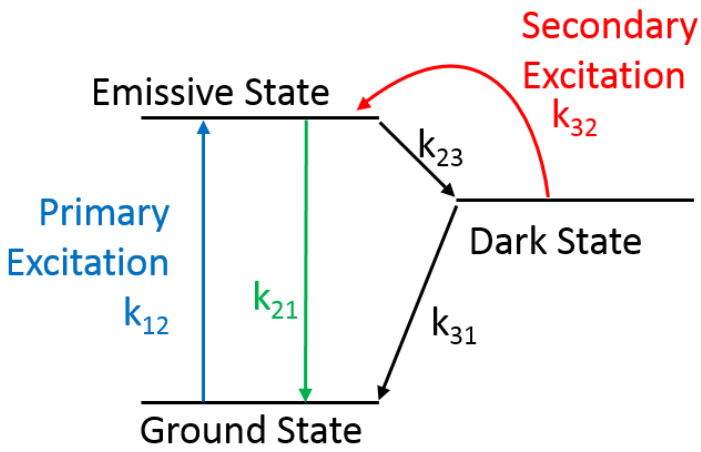

Figure 4.1 Schematic of Ag-DNA cluster photophysics during optical modulation/upconversion. Fluorescence is a result of primary, higher energy wavelength excitation into the emissive state (k_{12}) and relaxation back to the ground state (k_{21}). While in the emissive state, transitions into a dark state (k_{23}) can also occur. The application of a second, longer wavelength laser causes repumping of dark photons directly into the emissive state (k_{32}), providing a direct means for additional fluorescence.

Application of secondary excitation is modelled as a repumping out of the non-emissive state directly back into emissive states (k_{32}). Once repumped, fluorophores can then relax fluorescently or repopulate the dark state. We have empirically observed that unless a minimal excitation intensity of both lasers is applied (100's of W/cm^2 of pulsed primary, ~1 kW/cm^2 of secondary), fluorescence enhancement is limited. We refer to this process as a sequential two-photon upconversion.

$$\frac{d}{dt}\begin{pmatrix} S_0 \\ S_1 \\ T \end{pmatrix} = \begin{bmatrix} -k_{12} & k_{21} & k_{31} \\ k_{12} & -(k_{23}+k_{21}) & k_{32} \\ 0 & k_{23} & -(k_{31}+k_{32}) \end{bmatrix} \begin{pmatrix} S_0 \\ S_1 \\ T \end{pmatrix} \qquad \text{Equation 4.1}$$

By applying ns-pulsed primary excitation and continuous wave (CW) secondary excitation while recording only photons arriving after the background fluorescent lifetime, it is possible to measure only the photons occurring as a result of the repumping

process. To do so, we simply ignore photons resulting from the primary ns pulsed excitation which arrive within the fluorescence lifetime and use a secondary laser to repump dark Ag-DNA clusters back into the emissive state, which are then able to relax radiatively in the form of additional fluorescence. As the dark state lifetime is tens of μs, (vs a few ns for fluorescence), photons occurring from the repumping process may occur on significantly longer timescales. This means that only the fluorophore of interest will be imaged during this time as there is no primary excitation to cause background fluorescence. This process provides a means to recover Ag-DNA signal even when the background autofluorescence signal is significantly higher than the fluorescence signal from Ag-DNA alone.

Sequential two-photon processes allow for the direct recording of background free signal photons, a direct complement and extension of previous SAFIRe methods. Although two lasers are applied, only fluorescence recorded between primary pulses is used. Only the analyte of interest exhibits additional fluorescence during periods between primary pulses where there is only secondary excitation, and thus no background contribution is recorded. The majority of the methods used in this chapter are presented in Chapter 2 (Section 2.4.2), and specific modes of excitation are presented in the section that follows.

4.2 Modes of Secondary Excitation

Primary excitation indirectly leads to dark state populations which can be repumped into the excited state and relax fluorescently. The use of pulsed primary excitation provides periods where secondary-only excitation alone (pulsed or CW) is applied, which does not generate endogenous background fluorescence. Pulsed primary

with pulsed secondary excitation (pulse-pulse) is shown in Figure 4.2, where a primary pulse nearly fully decays and a secondary pulse causes additional fluorescence. After a primary excitation pulse, a secondary pulse generates only a small additional fluorescence signal. This small secondary pulse generated fluorescence is only observed if primary excitation prepares the dark state, but the relatively small fraction of "upconverted " photons upon secondary illumination suggest a relatively small QY for regenerating the emissive excited state from dark state excitation (Figure 4.4). As a result, pulse-pulse is demonstrated only as a proof of concept in section 4.4, and the majority of experiments and background subtraction are executed using pulse-CW excitation.

4.3 Pulse-Pulse Proof of Concept

To demonstrate the recovery of additional fluorescence as a result of two-photon sequential upconversion, 630 nm emitters were irradiated with pulsed 560 nm excitation from a diode laser followed by pulsed 803 nm Ti:Sapphire secondary excitation. Shown

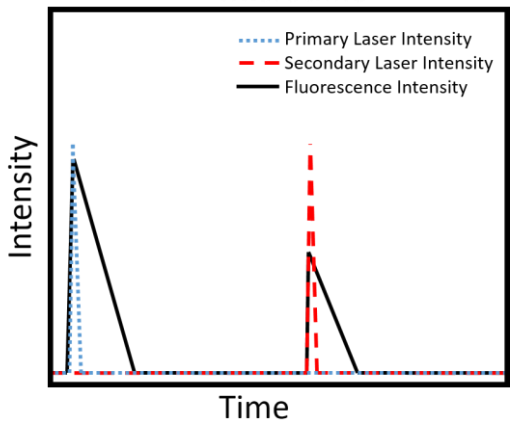

Figure 4.2. Schematic of a single pulse-pulse period. The primary and secondary laser pulses are shown in blue and red, respectively, and the fluorescence signal is shown in black.

in Figure 4.3, the sequential two-photon fluorescence is clearly visible as a second pulse following a primary excitation (Figure 4.3, inset).

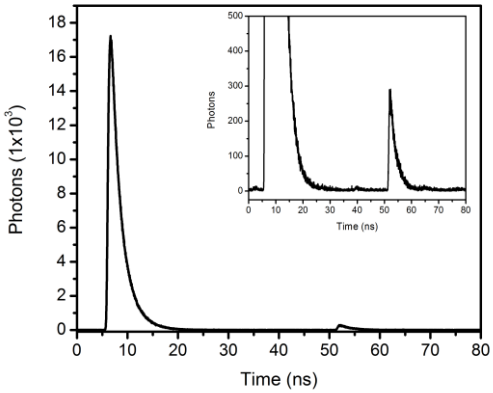

Figure 4.3. Pulse-pulse fluorescence signal in 630 nm Ag-DNA clusters resulting from 1.5 kW/cm^2 560 nm and 880 W/cm^2 803 nm ps pulsed 803 nm Ti:Sapphire for aqueous 630 nm emitters. Inset: magnified plot showing the fluorescence as a result of only 803 nm pulsed excitation.

This excitation scheme paves the way for signal extraction in high background environments by ignoring the photons from the primary excitation and recording only the photons recorded from secondary excitation via the sequential two-photon process. Maximizing the signal photons is crucial and, as compared with pulse-pulse experiments, pulse-CW excitation yields a much greater number of sequential photons providing a more robust means for signal extraction. Pulse-CW more thoroughly depopulates the dark state than pulse-pulse, as more dark state excitation cycles are possible between primary pulses. This provides greater information for characterizing the photophysical rates dictating sequential upconversion and results in increased fluorescence.

4.4 Pulse-CW Experiments

A schematic of pulsed primary, CW secondary (pulse-CW) excitation shows a two component decay in fluorescence with well-separated characteristic decay constants (Figure 4.4). This provides a maximum number of upconverted photons leading to improved signal over background fluorescence.

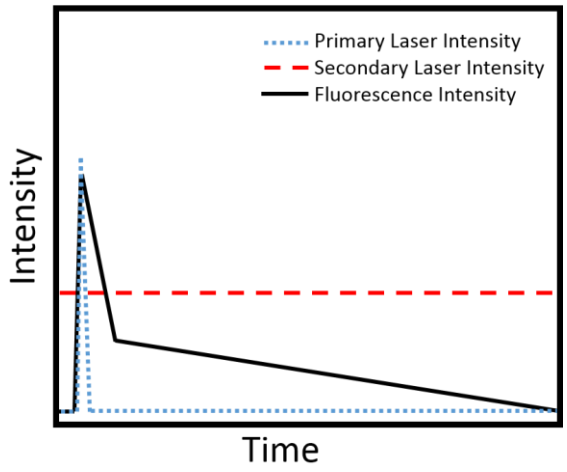

Figure 4.4. Schematic of a single period between primary pulses in pulse-CW. The fluorescence signal is shown as a black line, primary and secondary lasers are shown in blue and red. The x-axis of time is not to scale.

As pulse-CW excitation maximizes the total number of sequentially upconverted photons compared to pulse-pulse excitation, pulse-CW was the primary method utilized in this chapter. First, photophysical rates dictating sequential fluorescence upconversion are explored, outlining characteristic photophysical properties required for implementation. A demonstration of signal recovery of Ag-DNA clusters in the presence of a high background fluorescence is presented, combining sequential upconversion with FCS to show the utility of the sequential two-photon upconversion.

4.4.1 Sequential Two-Photon Lifetime

To investigate the parameters required for sequential two-photon excitation, fluorescence histograms were recorded using a very low pulse repetition rate (10 kHz) in the presence of CW secondary excitation. This low repetition rate allowed for measurements of very long (<50 μs) lifetimes for both 710 nm emitters and 630 nm emitters immobilized in PVA. 710 nm emitters were excited with 643 nm pulsed excitation in the presence of 803 nm CW excitation; 630 emitters were excited with 532 nm pulsed excitation with 803 nm CW excitation. A plot of a pulse-CW fluorescence histogram is shown in Figure 4.5 demonstrating the very different timescales of decay for fluorescence and unconverted fluorescence. In all fluorescence histograms, two very distinct lifetimes were immediately present: that of the ns fluorescence lifetime (black) and an additional, relatively low population decay having a significantly longer μs lifetime (red).

4.4.2 Dark State Photophysical Characteristics

Application of a pulsed primary laser causes excitation into the emissive state, a small portion of which relax into a non-emissive dark state. Fluorophores reside in this state for a period of time equal to the dark state lifetime. The rate at which fluorophores exit this state is equal to the inverse natural dark state lifetime, or k_{31}. Application of CW secondary excitation depopulates the dark state, directly promoting fluorophores back to the emissive state. This provides an additional path for dark state depopulation and is represented as k_{32}. The rate of photons leaving the dark state ($k_{offExit}$) is defined by the sum of these two processes (Equation 4.2).

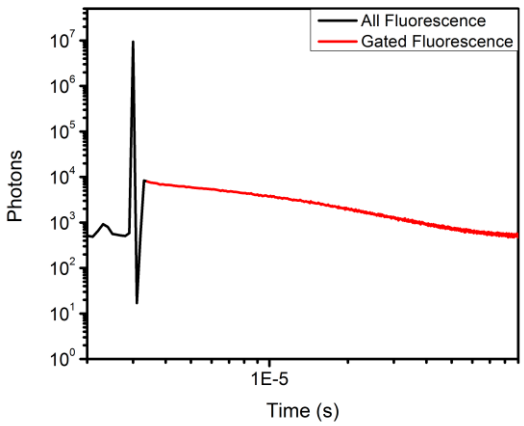

Figure 4.5. 710 nm Ag-DNA clusters with 9.0 W/cm^2 647 nm pulsed (10 kHz) average intensity and 990 W/cm^2 803 nm CW excitation immobilized in PVA. Due to the low repetition rate, a router was used to collect excitation pulse timing and photons in separate channels, as shown in Figure 2.5. The dip in fluorescence immediately after the initial fluorescence lifetime is a result of dead time on the detector as multiple photons were often recorded per primary pulse.

$$k_{offExit} = \frac{1}{(\mu s\ decay)} = k_{31} + k_{32} \qquad \text{Equation 4.2}$$

The rate out of the dark state due to secondary excitation, k_{32}, is the product of the dark state absorption cross section, σ_{dark}, the percent chance of exiting the dark state and directly re-entering the emissive manifold (reverse dark state or reverse intersystem quantum yield), Φ_{revisc}, and the intensity of secondary excitation, I_{sec}, multiplied by wavelength λ over Planck's constant multiplied by the speed of light (c, Equation 4.3).

$$k_{32} = I_{sec}\sigma_{dark}\Phi_{revisc}\frac{\lambda}{h \cdot c} \qquad \text{Equation 4.3}$$

Pulse-CW histograms performed at different excitation intensities are well described by Equation 4.3. A log-linear plot of only the slow decay is shown in Figure 4.6, comparing two different secondary excitation intensities resulting in differing decay rates. The difference in overall fluorescence intensities is understood as a more thorough depopulation of the dark state through unconverted fluorescence. In other words, the long dark state lifetime relative to the excitation pulse repetition rate means that dark state

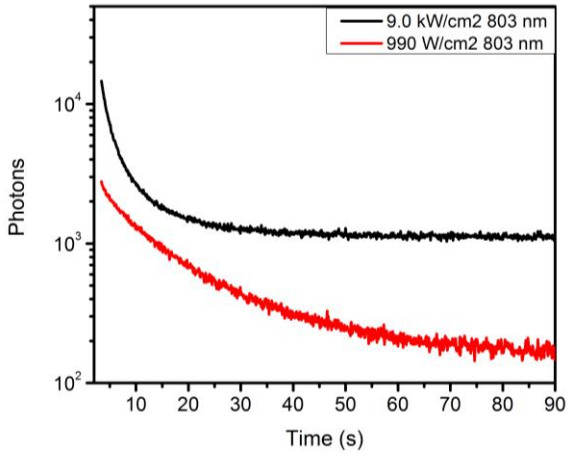

Figure 4.6. Pulse CW excitations of 710 nm Ag-DNA clusters with 9.0 W/cm^2 647 nm pulsed (10 kHz) average intensity showing only the longer time component. Note the difference in decay lifetime as a result of increased secondary laser intensity.

populations are built more rapidly than they are depopulated, resulting in a net increase of dark state populations. Thus, in both high and low intensity secondary excitation, the dark state population is not exhausted between each cycle. Higher excitation intensity simply depopulates this dark state faster than with lower excitation (Equation 4.3). Photophysical dark state lifetimes are presented in Table 4.1

To study the effect of increasing secondary excitation intensity on the μs dark state lifetime, fluorescence decay histograms were obtained across varying secondary excitation intensities while holding the pulsed primary excitation intensity constant. As

Table 4.1. Photophysical parameters for 630 nm and 710 nm emitters in PVA.

Ag-DNA Cluster	τ_1 (μs)	τ_2 (μs)	$\sigma_{dark}\Phi_{iscrev}$ (cm^2, 10^{-18})	$\sigma_{dark2}\Phi_{iscrev2}$ (cm^2, 10^{-18})
710 nm	3.9 ± 0.5	16 ± 1	11 ± 1	1.9 ± 0.2
630 nm	12 ± 1	70 ± 8	1.1 ± 0.2	0.27 ± 0.05

the measured rates of decay are the sum of a natural rate (k_{31}) and excitation rate (k_{32}, Equation 4.2), fluorescent decays were recorded at varying secondary intensity to measure both k_{31} and relevant photophysical parameters (Equation 4.3). Attempts to fit the μs decay as a single exponential were unsuccessful but biexponential fits did yield reasonable matches (Figure 4.7), suggesting two different decay constants that are both affected by secondary excitation. Fits were made to Equation 4.4. The biexponential fits

$$I(t) = A_1 e^{-\frac{t}{\tau_1}} + A_2 e^{-\frac{t}{\tau_2}} \qquad \text{Equation 4.4}$$

resulted in the extraction of two decay constants (or lifetimes). Increasing secondary intensity increases k_{32} and thus $k_{offExit}$ for both states, and is shown as two positive slopes in Figure 4.8.

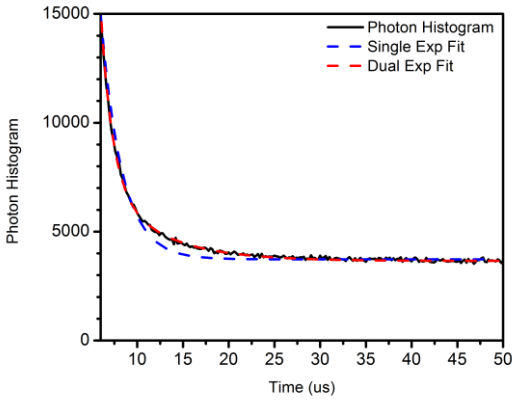

Figure 4.7. Typical fluorescence decay curve beyond the first few-ns decay. A single component fit is shown in the blue dashed line and a dual component fit is shown by the red dashed line. Data was for a 710 nm emitter immobilized in 20 % wt/v PVA excited with a 643 nm 100 ps pulsed laser with a 10 kHz rep rate, using 6 W/cm^2 average intensity and 6 kW/cm^2 CW 803 nm excitation. The two characteristic lifetimes for 710 nm emitters are presented in
Table 4.1.

A

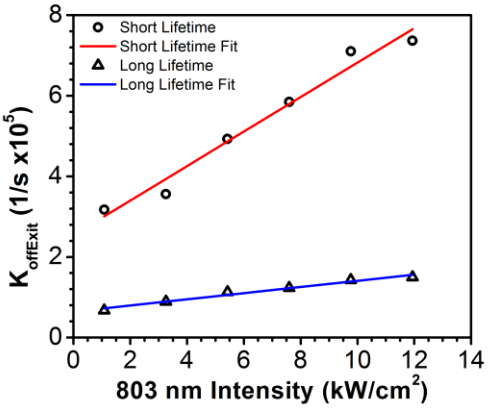

B

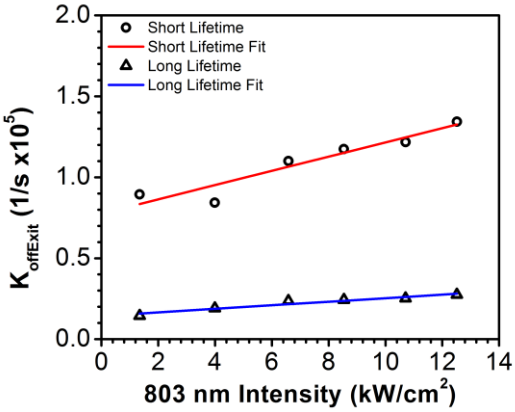

Figure 4.8. Extracted $k_{offExit}$ values from dual exponential fits (Equation 4.4) plotted as inverse lifetime as a function of 803 nm excitation intensity. Linear fits are according Equation 4.2. The two characteristic lifetimes for (A) 710 nm emitters and (B) 630 nm emitters are presented in Table 4.1

Figure 4.8 demonstrates the linear relationship between inverse lifetime ($k_{offExit}$) and secondary excitation intensity (I_{sec}), where the zero-intercept is the natural off time (k_{31}) and the slope of the fit is proportional to the product of the absorption cross section and reverse dark state quantum yield, $\sigma_{dark}\Phi_{iscrev}$ (Equation 4.2). While it is not possible to separate σ_{dark} from Φ_{iscrev}, the product of those two parameters provides insight into the interaction of secondary excitation with the fluorophore. The natural off time τ_N, equal to $1/k_{31}$, and $\sigma_{dark}\Phi_{iscrev}$ for both 630 and 710 nm emitters are presented in Table 4.1

The results from Table 1 provide some photophysical insight into the source of enhancement and thus utility as modulatable probes. Specifically, the fluorescence enhancement in aqueous conditions under dual excitation of 630 nm emitters is significantly higher than 710 nm emitters, but 710 nm emitters have an order of magnitude higher $\sigma_{dark}\Phi_{iscrev}$. The greater $\sigma_{dark}\Phi_{iscrev}$ indicates a greater degree of secondary absorption by the dark state, higher percentage of emitters returning to the emissive state, or a combination of both. While the method cannot determine the mechanism of increased $\sigma_{dark}\Phi_{iscrev}$, the 710 nm emitters in fluorescent dark states demonstrated a stronger response to intensity changes in secondary excitation. It is also important to mention that previous work in our group has determined a dual decay in transient absorption, suggesting that dual decay may be due to delocalization of charge in the ss-DNA bound to the silver cluster.[24] In this case, multiple decay components would be better represented by a continuous distribution of decay times, and thus stretched exponential fitting would be preferred over biexponential.[24]

Importantly, enhancements in fluorescence in aqueous solutions as a result of secondary excitation are significantly larger in the 630 nm emitter compared to the 710

nm emitter (Section 3.4). Also apparent from Table 4.1is the significantly longer natural dark state lifetime in 630 nm emitters versus 710 nm emitter dark state lifetime. It is important to recall that koffExit is the sum of competing k_{31} and k_{32} rates and that for pulsed excitation, k_{32} results in additional fluorescence while k_{31} results in lost sequential upconverted fluorescence. Longer dark state lifetimes in 630 nm emitters are beneficial to sequential upconversion because the competitive nonradiative relaxations are minimized, increasing the number of fluorophores available for sequential upconversion. The order of magnitude lower $\sigma_{dark}\Phi_{iscrev}$ (proportional to k_{32}) in 630 nm emitters is more than made up for by the lower natural off rate (k_{31}) as photons that relax from dark states nonradiatively are no longer accessible to secondary excitation. Photophysical rates into and out of the dark state are crucial the utility of this method, as sufficient populations must be both available and sensitive to excitation.

4.4.3 FCS Concentration Recovery Using Pulse-CW

Given a high enough enhancement (>20%), pulse-CW sequential two-photon fluorescence correlation spectroscopy (FCS) concentration measurements of water solvated Ag-DNA clusters amid a high sulforhodamine 101 (S101) background are possible. This was accomplished by collecting all fluorescence occurring well outside the duration of the S101 background fluorescent lifetime (τ_{S101} = 6 ns). Application of a CW long wavelength secondary laser causes additional fluorescence solely from the Ag-DNA clusters and not from the S101 background. Recording only photons on timescales well outside the background fluorescent lifetime, it is possible to measure Ag-DNA cluster fluorescence with very low background contribution.

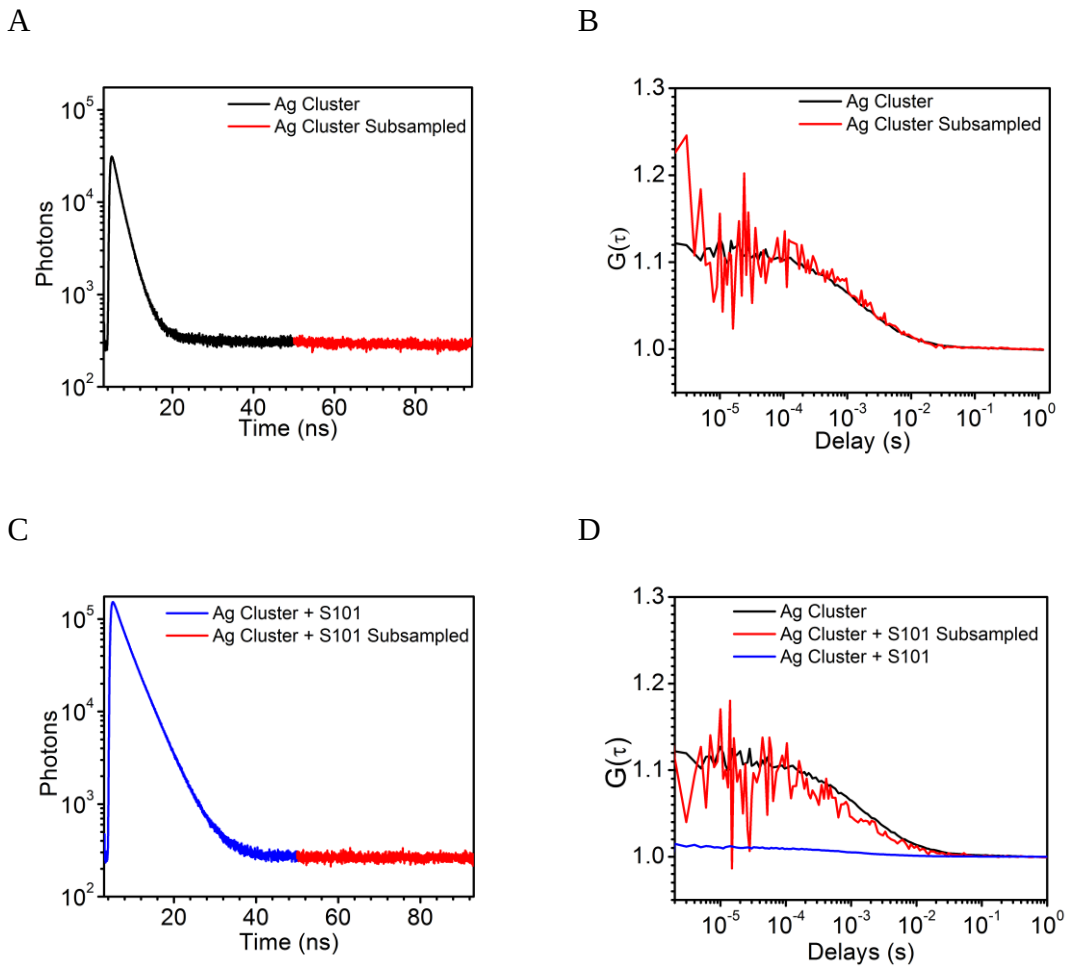

Figure 4.9. Photon arrival histograms of an aqueous 630 nm Ag-DNA clusters, depicting the relatively rapid fluorescence decay and relatively longer lived decay. (A) Fluorescence histogram of Ag-DNA cluster positive control, showing all photons (black) and only those recorded outside the fluorescent lifetime (red, >50 ns). (B) Corresponding correlation decays as a result of the full fluorescence trace (black) and subsampled fluorescence (red), providing a control for the concentration recovery. (C) Plot of fluorescence signal from a mixture of S101 and 630 nm emitters, and D shows the corresponding correlation decays for the full (blue) and subsampled photons (red). The black plot in (D) is the FCS curve from an Ag-DNA cluster only sample (B), and is repeated in (D) for comparison.

Setting the repetition rate of the primary laser sufficiently high to capture the timescale of interest is crucial to permit recovery of concentration via application of FCS, thus mandating repetition rates faster than diffusion. For our experiments, a pulsed 560

nm excitation of 10 MHz was sufficient to capture diffusion and extract concentrations (Figure 4.9). The addition of CW 805 nm excitation provided additional photons, many occurring on timescales longer than the fluorescence lifetime. The relatively low aqueous enhancement of the 710 nm emitter was prohibitive for aqueous concentration recovery via two-photon fluorescence upconversion FCS. Therefore, recovery was performed solely for 630 nm emitters. Controls containing 630 nm emitters alone were run to confirm concentration recovery (Figure 4.9A-B). Recovery of analyte over background was accomplished by gating against photons that arrived during the background fluorescence (Figure 4.9A-C, black) lifetime and measuring only photons sequentially upconverted from the dark state (Figure 4.9A-C, red). Fits to correlations of these photons still retain the same approximate concentration of Ag-DNA clusters, demonstrating concentration recovery amid high background.

4.5 Conclusions

Improvements in fluorescence sensitivity may be achieved through background reduction. Direct optical repopulation of emissive states via long wavelength excitation permits collection of photons only during periods of secondary only excitation and thus very low background fluorescence. Complementary to SAFIRe which relies on analyte-specific photobrightening as a result of secondary long wavelength excitation, sequential two-photon fluorescence upconversion enables significantly reduced background fluorescence in samples of high endogenous background.

While lower primary repetition rates (500 kHz) offer utility for FCS concentration recovery, we demonstrate that higher (10 MHz) repetition rates are very feasible (Figure 4.9). While the faster repetition rates could more immediately be applied to FCS

dynamics significantly faster than diffusion, two-photon sequential upconversion has significantly broader applications in the field of fluorescence microscopy. It certainly is readily adaptable to biological imaging by measuring unconverted fluorescence, and the decay dynamics in upconverted fluorescence have potential use as a biological sensor.

Leveraging 630 nm Ag-DNA cluster sequential two-photon fluorescence upconversion via a pulsed primary and CW secondary excitation, Ag-DNA photons were recorded well outside the fluorescence lifetime of both Ag-DNA analyte and S101 background. It was then possible to measure fluorescence fluctuations arising from diffusion, quantitatively recovering analyte concentrations in the presence of high background. While this work represents a proof of concept, the applications readily extend to a wide array of fluorescence experiments including biologically relevant environments and multi-colored fluorescence imaging.

4.6 References

1. Aubin, J. E. "Autofluorescence of viable cultured mammalian cells." *The Journal of Histochemistry and Cytochemistry*, **1979**, *27*, 36-43.

2. Weiss, S. "Fluorescence Spectroscopy of Single Biomolecules." *Science*, **1999**, *283*, 1676-1683.

3. Lin, B.; Urayama, S.; Saroufeem, R. M. G.; Matthews, D. L.; Demos, S. G. "Characterizing the origin of autofluorescence in human esophageal epithelium under ultraviolet excitation." *Optics Express*, **2010**, *18*, 21074-21074.

4. Petty, J. T.; Fan, C.; Story, S. P.; Sengupta, B.; St. John Iyer, A.; Prudowsky, Z.; Dickson, R. M. "DNA encapsulation of 10 silver atoms producing a bright, modulatable, near-infrared-emitting cluster." *Journal of Physical Chemistry Letters*, **2010**, *1*, 2524-2529.

5. Petty, J. T.; Fan, C.; Story, S. P.; Sengupta, B.; Sartin, M.; Hsiang, J. C.; Perry, J. W.; Dickson, R. M. "Optically enhanced, near-IR, silver cluster emission altered by single base changes in the DNA template." *Journal of Physical Chemistry B*, **2011**, *115*, 7996-8003.

6. Rao, J.; Dragulescu-Andrasi, A.; Yao, H. "Fluorescence imaging in vivo: recent advances." *Current Opinion in Biotechnology,* **2007**, *18*, 17-25.

7. Hsiang, J. C.; Jablonski, A. E.; Dickson, R. M. "Optically modulated fluorescence bioimaging: Visualizing obscured fluorophores in high background." *Accounts of Chemical Research,* **2014**, *47*, 1545-1554.

8. Mansfield, J. R.; Gossage, K. W.; Hoyt, C. C.; Levenson, R. M. "Autofluorescence removal, multiplexing, and automated analysis methods for in-vivo fluorescence imaging." *Journal of Biomedical Optics,* **2005**, *10*, 041207-041201 - 041207-041209.

9. Marriott, G.; Mao, S.; Sakata, T.; Ran, J.; Jackson, D. "Optical lock-in detection imaging microscopy for contrast-enhanced imaging in living cells." *Proceedings of the National Academy of Sciences,* **2008**.

10. Richards, C. I.; Hsiang, J.-C.; Dickson, R. M. "Synchronously amplified fluorescence image recovery (SAFIRe)." *The Journal of Physical Chemistry B,* **2010**, *114*, 660-665.

11. Mao, S.; Benninger, R. K. P.; Yan, Y.; Petchprayoon, C.; Jackson, D.; Easley, C. J.; Piston, D. W.; Marriott, G. "Optical Lock-In Detection of FRET Using Synthetic and Genetically Encoded Optical Switches." *Biophysical Journal,* **2008**, *94*, 4515-4524.

12. Jablonski, A. E. *Optically Modulated Fluorescent Proteins.* PhD Thesis, Georgia Institute of Technology, 2014.

13. Fan, C.; Hsiang, J.-C.; Dickson, R. M. "Optical Modulation and Selective Recovery of Cy5 Fluorescence." *ChemPhysChem,* **2012**, *13*, 1023-1029.

14. Fan, C.; Hsiang, J.-C.; Jablonski, A. E.; Dickson, R. M. "All-optical fluorescence image recovery using modulated stimulated emission depletion." *Chemical Science,* **2011**, *2*, 1080-1080.

15. Chen, Y.-C.; Jablonski, A. E.; Issaeva, I.; Bourassa, D.; Hsiang, J.-C.; Fahrni, C. J.; Dickson, R. M. "Optically Modulated Photoswitchable Fluorescent Proteins Yield Improved Biological Imaging Sensitivity." *Journal of the American Chemical Society,* **2015**, 150924164102005-150924164102005.

16. Zheng, W.; Tu, D.; Huang, P.; Zhou, S.; Chen, Z.; Chen, X. "Time-resolved luminescent biosensing based on inorganic lanthanide-doped nanoprobes." *Chemical Communications,* **2015**, *51*, 4129-4143.

17. Boyer, J. C.; Vetrone, F.; Capobianco, J. A.; Speghini, A.; Bettinelli, M. "Variation of Fluorescence Lifetimes and Judd-Ofelt Parameters between Eu 3+ Doped Bulk and Nanocrystalline Cubic Lu 2 O 3." *The Journal of Physical Chemistry B*, **2004**, *108*, 20137-20143.

18. Zheng, W.; Huang, P.; Tu, D.; Ma, E.; Zhu, H.; Chen, X. "Lanthanide-doped upconversion nano-bioprobes: electronic structures, optical properties, and biodetection." *Chemical Society Reviews*, **2015**, *44*, 1379-1415.

19. Lakowicz, J. R. *Principles of Fluorescence Spectroscopy*; Springer: New York, 2006.

20. Tropiano, M.; Faulkner, S. "A lanthanide based sensor for the time-gated detection of hydrogen sulfide." *Chemical Communications*, **2014**, *50*, 4696-4698.

21. Richards, C. I.; Hsiang, J.-C.; Senapati, D.; Patel, S.; Yu, J.; Vosch, T.; Dickson, R. M. "Optically Modulated Fluorophores for Selective Fluorescence Signal Recovery." *Journal of the American Chemical Society*, **2009**, *131*, 4619-4621.

22. Jablonski, A. E.; Vegh, R. B.; Hsiang, J. C.; Bommarius, B.; Chen, Y. C.; Solntsev, K. M.; Bommarius, A. S.; Tolbert, L. M.; Dickson, R. M. "Optically modulatable blue fluorescent proteins." *Journal of the American Chemical Society*, **2013**, *135*, 16410-16417.

23. Widengren, J.; Mets, U.; Rigler, R. "Fluorescence correlation spectroscopy of triplet states in solution: a theoretical and experimental study." *The Journal of Physical Chemistry*, **1995**, *99*, 13368-13379.

24. Patel, S. *Photophysics of Fluorescent Silver Nanoclusters.* PhD Thesis, Georgia Institute of Technology, 2009.

CHAPTER 5

STOCHASTIC OPTICAL FLUCTUATION IMAGING

5.1 Introduction

Fluorescence microscopy has been applied to study biological processes occurring at ever smaller sizes. Practical limitations in microscope objective aperture size limit the collection angle and result in the Abbe limit, (Equation 1.3) producing a bandwidth-limited optical transfer function that limits the resolvable optical frequencies collected by the microscope objective.[1,2] The finite objective aperture and limited collection angle lead to a three dimensional diffraction pattern that is both manifested as a spatial broadening of features in three dimensions and quantified by the point spread function (PSF).[3] The PSF is the response of an optical system to a single point source. Treated as single point sources, the point spread functions (PSF) of emitters in close proximity will be overlapped and indistinguishable, placing an upper limit on optical resolution and ultimately, observable biological and biophysical processes.

When discussing resolution, it is important to differentiate between narrowing of the PSF and an increase in resolution. While narrowing of the PSF is crucial to increased resolution, it is the ability to distinguish between separate overlapping PSFs that defines an increased resolution beyond the optical limit. The Rayleigh criterion is often used, defining two PSFs as resolved if the peak of one is centered over the first minimum of another. However, the Sparrow criterion is a more restrictive limit to surpass, stating that the resolution is achieved when the combined intensity from two overlapping PSFs is constant along a line between the central peaks of brightness.

In an effort to circumvent this resolution limit and image smaller structures, a number of techniques have emerged over the last decade collectively known as super-

resolution imaging.[4-6] Post-processing super-resolution methods utilize only measured fluorescence, require no modifications in collection optics, and are thus readily applicable to current experimental setups. Typically, however, all of these methods require that multiple measurements are taken such that periods of with fluorophore emission and periods without fluorophore emission are captured. This puts practical limitations on concentration, as emissive/nonemissive states must be recorded from individual emitters. As a result, FCS concentrations are generally required. Additionally, stationary fluorophores are assumed in all cases. Examples of post-processing super-resolution methods include Bayesian analysis of the blinking and bleaching (3B), single-molecule high-resolution imaging with photobleaching (SHRImP), and super-resolution optical fluctuation imaging (SOFI), and will next be described.[7-9]

3B utilizes a series of widefield images that capture independent blinking and bleaching events and then applies a Bayesian technique to model the entire dataset resulting from individual fluorophores.[8] This method is thus dependent on widefield imaging and incurs a high computational load.[10,11] By contrast, SHRImP uses only sequential photobleaching of individual fluorophores, comparing fluorescence measurements before and after multi-step bleaching processes to localize individual fluorophores.[9] However, SHRImP cannot separate fluorophorophores that bleach simultaneously, and can only record distances in two dimensions. SOFI builds upon of previous statistical methods applied to fluorescence correlation spectroscopy, which were able to resolve the presence of multiple diffusing species based solely on differences in brightness.[12] Explained in detail in Section 5.2, SOFI utilizes higher order cumulants to narrow the PSF based on the blinking statistics of individual emitters. Of these three methods, only SOFI is both readily adaptable to a standard confocal microscope and well suited to significant gains in resolution with lower computational load (Section 5.3.1).[7,8,13,14]

The seminal SOFI work from Dertinger, *et al.*, studied the application of super-resolution to CCD-based SOFI imaging of quantum dots (QDs), demonstrating a five-fold resolution enhancement over widefield microscopy.[7] QD labelled microtubulin networks of 3T3 cells were used to demonstrate narrowing of the PSF in three dimensions. However, previous reports of SOFI methods are limited to CCD image capture methods which are currently bound to sub kHz frame rates and >1 s overall time resolution. This limits fluorescent labels to those that respond on this time scale, either blinking naturally or manipulated through external stimulus to induce on/off switching. Both QDs and molecular photoswitches have been employed but these represent only a subset of fluorescent probes available to biological study.[7,13] Additionally, the slow blinking characteristics of these two classes of probes require long acquisition times, mandating near immobile samples.

Our group has previously extended SOFI from CCD imaging to confocal microscopes with single element detectors, specifically avalanche photodiodes (APDs), in an effort to approach significantly faster acquisition times (<1 ms).[15] Higher temporal resolution would enable the study of processes occurring on faster timescales, revealing a greater range of dynamics. Additionally, a greater range of fluorophores would become available as any fluorophore with µs fluorescent blinking could be used as a SOFI label. This chapter explores SOFI with µs blinking fluorophores both with computational simulation and experiment. The work herein extends simulations of SOFI by generating position-independent fluorescence signals as a function of two-dimensional (2D) scan position, implementing rapid laser scanning for cross-correlative signals, significantly reducing computational load, and exploring important photophysical traits to identify effective SOFI probes.

5.2 Theory

5.2.1 Autocumulants

Using the formalism of Dertinger, *et al.*, we can represent the sum of collected fluorescence as a function of position using Equation 5.1, where F(r,t) is the fluorescence

$$F(r,t) = \sum_{k=1}^{N} \delta(r - r_k) \cdot \varepsilon_k \cdot s_k\,(t) \qquad \text{Equation 5.1}$$

at position r and time t, represented as a sum of N total emitters, where each k emitter is the product of the delta function of position $\delta(r\text{-}r_k)$, molecular brightness ε_k and time-dependent stochastic blinking $s_k(t)$.[7]

For a point scanning geometry however, the delta functions are convolutions with the excitation and emission point spread functions (PSFs). As a result, the delta function $\delta(r_1\text{-}r_k)$ is replaced with the convolution of excitation and emission PSFs, $U_{exc}(r_1\text{-}r)$ and

$$F(r,t) = U_{exc}(r_1 - r) \otimes \sum_{k=1}^{N} U(r_1 - r_k) \cdot \varepsilon_k(r_1 - r_k) \cdot s_k(r_1 - r_k, t) \qquad \text{Equation 5.2}$$

$U(r_1\text{-}r_k)$ respectively, shown in Equation 5.2 where r_1 is the current excitation PSF position and r_k is the emitter position. It is also important to mention that both molecular brightness and time-dependent stochastic blinking are excitation intensity dependent, and thus a function of position. However, for the purposes of this thesis, excitation intensities are extremely high and thus fluorescence intensity is saturated. The differences in molecular brightness and stochastic blinking are thus less important than they would be at low excitation intensities. In the limit of high excitation intensities, the positional dependence of both molecular brightness and stochastic blinking are approximated as constant across the excitation PSF.

This PSF is approximated as a Gaussian function and is shown in Equation 5.3 for emitter k as a three-dimensional Gaussian function using variance σ^2 and Cartesian coordinates x, y, and z. The width of the PSF may be represented in terms of $1/e^2$ or e^2 radius, but may also be reported in terms of σ, the standard deviation of the function, or the full width at half the maximum value (FWHM).

$$U(x,y,z) = e^{\frac{-(x-x_k)^2-(y-y_k)^2}{2\,\sigma_{xy}^2} - \frac{(z-z_k)^2}{2\,\sigma_z^2}} \qquad \text{Equation 5.3}$$

Using the second order autocorrelation function as an example, the correlation of fluorescence signal in shown in Equation 5.4, where dF(t) is the time dependent fluorescence fluctuation. The corresponding representation of the fluorescence in terms of Equation 5.2 is shown in Equation 5.5. Considering the multiple emitters with

$$G_2(r,t) = \langle dF(t+\tau) \cdot dF(t) \rangle \qquad \text{Equation 5.4}$$

$$G_2(r,t) = {U_{exc}}^2(r_1 - r) \otimes \sum_{k=1}^{N} U^2(r_1 - r_k) \cdot {\varepsilon_k}^2 \cdot \langle ds_k(t+\tau) \cdot ds_k(t) \rangle \qquad \text{Equation 5.5}$$

overlapping fluorescent PSFs, Equation 5.2 applied to Equation 5.4 would lead to cross terms when expanded. In the case of very high excitation intensities, fluorescent blinking is independent, these cross terms go to zero. Additionally, both excitation and emission PSFs are squared as a result of the second order autocorrelation function, resulting in a decrease in the width of PSF. This relationship holds as higher orders are applied, meaning the n^{th} order autocorrelation leads to the PSF raised to the n^{th} power, resulting in a $\sqrt{n}$ decrease in the width of the PSF. The combination of these two factors plays an important role in the narrowing of PSFs, but not all cross terms are removed solely due to

independence in blinking. An example of nonzero cross terms is next described, illustrating the need for cumulants.

It is crucial to note that the reduction in PSF results in super-resolution if the n^{th} order correlation only contains terms relating directly to the n^{th} power of the PSF. For example in the fourth order there is a case where cross correlations don't cancel: two correlations for one emitter and two correlations from another emitter. Cumulants in place of correlations filter out these lower order contributions such that only n^{th} order autocorrelations are considered. The omission of these lower order cross-terms removes their contribution, which otherwise broaden the PSF (i.e. summing PSFs raised to a lower power). For this reason, cumulants are used in place of correlations and are capable of resolution improvements beyond the optical limit.

While autocorrelations contain cross terms relating to various powers to the PSF, cumulants do not. By definition a cumulant is a function of delay and can be expressed in terms of correlations. Cumulants (C) in terms of correlation functions (G) of fluorescent signals are shown in Equation 5.6 to Equation 5.8 for second to fourth order, respectively.[7,16] Although many cross terms between independently blinking emitters are

$$C_2(r,\tau_1) = G_2(r,\tau_1) \qquad \text{Equation 5.6}$$

$$C_3(r,\tau_1,\tau_2) = G_3(r,\tau_1,\tau_2) \qquad \text{Equation 5.7}$$

$$C_4(r,\tau_1,\tau_2,\tau_3) = G_4(r,\tau_1,\tau_2,\tau_3) - G_2(r,\tau_1)G_2(r,\tau_3) - G_2(r,\tau_1+\tau_2)G_2(r,\tau_2+\tau_3) - G_2(r,\tau_1+\tau_2+\tau_3)\,G_2(r,\tau_2) \qquad \text{Equation 5.8}$$

zero, some higher order nonzero cross terms contribute wider PSFs (Equation 5.5) and subtraction of these lower order correlations narrows the PSF. Application of cumulants to fluorescence signals is important and provides a uniform and straightforward statistical

method for reducing the PSF and resolving single fluorescent emitters that would otherwise be indistinguishable.

Originally proposed by Weiss, Enderlein, *et al.* and applied to widefield charge-coupled device (CCD) imaging, SOFI relies on the accumulation of many successive images to capture independent blinking that is statistically separated between emitters.[17] Cumulants are a measure of the probability of only n-related events, using n^{th} order correlations that raise the PSF to the n^{th} power, narrowing the PSF. To successfully narrow the PSF, lower order correlations (and their wider PSFs) must be removed, mandating cumulants. The application of higher order correlations combined with the subtraction of lower order contributions is the driving factor of improved resolution. However, emitters must be both immobile and blink independently and signal measurements must be fast enough to capture individual blinking events. Concentrations must also be low enough such that individual events can be captured. Additionally, increasing orders of correlation subtractions result in both diminishing resolution improvements and increasing computational load. Novel reductions in computational load are discussed in Section 5.3.1.2.

5.2.2 Approximation to Reduce Computational Load

The computational load for determining cumulant values for all delays at increasing orders scales exponentially and rapidly becomes unreasonable. The amplitude of the cumulant at the zero delay value is an approximation that significantly reduces computational load. As a result, the n^{th} order correlation function is reduced to the n^{th} order central moment. This makes it possible to approximate cumulants in terms of central moments.

The expression of cumulants in terms of central moments are determined according to both Equation 5.9 and Equation 5.10, where κ_n is the cumulant of order n, i

is √(-1), k is the argument which ultimately drops out of Equation 5.9 and μ_n is the raw moment $\langle x^n \rangle$. To briefly summarize, the coefficients of the Taylor expansion of exp(γ) are equated to the left hand side of Equation 5.9, and $\sum_{n=1}^{\infty} \frac{\kappa_n (i \cdot k)^n}{n!}$ is substituted for γ:[18]

$$\sum_{n=1}^{\infty} \frac{\mu_n (i \cdot k)^n}{n!} = Taylor\ Expansion[exp(\gamma)]_{n=0} \qquad \text{Equation 5.9}$$

where:

$$\gamma = \sum_{n=1}^{\infty} \frac{\kappa_n (i \cdot k)^n}{n!} \qquad \text{Equation 5.10}$$

Solving for a cumulant κ_n at the zero delay in terms of moments μ_n for the first few cumulants in terms of raw moments yields:

$$\kappa_1 = \mu_1 \qquad \text{Equation 5.11}$$

$$\kappa_2 = \mu_2 - {\mu_1}^2 \qquad \text{Equation 5.12}$$

$$\kappa_3 = \mu_3 - 3\mu_1 \cdot \mu_2 + 2{\mu_1}^3 \qquad \text{Equation 5.13}$$

$$\kappa_4 = \mu_4 - 4\mu_3\mu_1 - 3{\mu_2}^2 + 12\,\mu_2\,{\mu_1}^2 - 6{\mu_1}^4 \qquad \text{Equation 5.14}$$

These expressions of cumulants in terms of moments are referred to herein as autocumulants as they rely on only the fluorescence collected from a single point.

5.2.3 Cross Cumulants

Cumulants performed on photon trajectories at a single position are also known as autocumulants. Cross cumulants have also been determined from correlations of photon trajectories from different positions.[14] Provided data collection at both positions occurs simultaneously, cross cumulants eliminate shot-noise by correlating separate fluorescence signals each with uncorrelated noise. They also provide a means for relating both space and time and have been shown to generate additional pixels.[14] They are perhaps most simply expressed in the second order (Equation 5.15).

$$XC_2\,(r_1 r_2, \tau\,) = \sum_k \langle \delta F_k(t) \cdot \delta F_k(t+\tau) \rangle_t \; U(r_1 - r_k)\; U(r_2 - r_k) \qquad \text{Equation 5.15}$$

The cross cumulant, computed from fluorescence signals obtained simultaneously from two different positions, is described in Equation 5.15. For each emitter k, Equation 5.15 is a function of two points (r_1, r_2), where dF_k, r_k are the fluorescence fluctuations and positions of each emitter contributing signal in the cross cumulant, respectively. A weighting term emerges as result of the sum that corresponds to the geometric middle of the points r_1 and r_2.[7,14] Thus, for all cross cumulants, the resulting value is plotted at the position represented by the geometric middle. Cross cumulants are advantageous when fluorescence is collected at two positions simultaneously, as they eliminate shot noise which can potentially contribute significantly to the cumulants when using the central moment as an approximation. They cannot be used when data is collected serially at separate positions, as the same fluorescence fluctuations for a single emitter are no longer simultaneously represented in both data traces.

A derivation of multivariate cumulants is not shown here, though other derivations may be found.[16] For the purpose of this work, multivariate cumulants were

generated in terms of central moments using Mathematica's MomentConvert function, which originated from the mathStatica package.[19]

5.3 Methods

5.3.1 Computational Simulation Methods

Simulations of 2D PSF narrowing in a confocal geometry were written in MATLAB (Mathworks). Raster scanning across a two-dimensional plane was implemented and individual fluorescence traces were generated at each point independently. While each fluorescence trace was saved as an independent file, it would be more computationally efficient for future simulations to aggregate all data traces into a single file.

PSFs were determined from the combination of excitation wavelength and numerical aperture, leading to a Gaussian distribution of excitation intensity. Written in terms of empirically relevant photophysical parameters such as dark state quantum yield, dark state lifetime, extinction coefficient, fluorescence lifetime, and fluorescence quantum yield, the fluorescence emission was simulated. Specifically, independent fluorescent time traces were generated at each position using a Gaussian PSF, extinction coefficient, and fluorescence quantum yield. A maximum time step of 50 ns was used, along with the excitation intensities and fluorescence lifetimes used to generate a matrix of Poisson distributed photons. From this distribution, a percentage of those photons, determined by the dark state quantum yield, transition into a dark state for an exponentially distributed period of time defined by the dark state lifetime. Corrections for any potential overlapping dark states are made and fluorescence quantum yields are applied. Finally, any loss of photons due to non-unity detection efficiency are applied, and a uniform distribution of background photons is added. Throughout the simulation,

checks on the photophysical properties are performed, measured, and reported. Individual simulations of two fluorophores at varying distances apart were simulated.

Data analysis was performed in MATLAB versions r2012b-r2015a. However, as there is no built-in function for the computation of cumulants, Mathematica (Wolfram, version 9.0.1) was used to generate symbolic output of cumulants in terms of moments and exported as an ASCII text file. MATLAB was used to parse the Mathematica ASCII output files and apply the necessary mathematical operations on each photon trajectory. Higher order cumulants are comprised of increasingly lengthy arithmetic combinations of the same central moments, often determined using significantly longer computation time.

5.3.1.2 Reduction in Computational Load

Significant effort was extended to reduce computational load in both data simulation and analysis. For simulation, the design of a vectored approach to fluorescence data traces was developed, leveraging the efficient computational BLAS and LAPACK libraries integrated in Matlab to generate a time trace of Poisson distributed photons in a single step.[20] Next, dark state entrance probabilities were assigned, thresholded, and exponentially distributed non-fluorescent times were generated. A single for-loop was used to prevent overlapping dark state lifetimes. Finally, detection efficiencies and background photons were applied in subsequent steps and the entire process was repeated for overlapping fluorophores. Using this approach instead of the standard nested set of for-loops reduced the computation time for simulated data traces significantly (>30%).

Additional gains were made for analysis as well. Higher order cumulants are comprised of an increasingly higher number of central moments, but the same central moments are repeated far more extensively. Thus, a very high degree of memory caching was developed such that moments of the same order were only computed once and extensively reused in the cumulant calculation. This reduced computation of very high

order cumulant images from days to minutes. Finally, as the simulation and analysis of each position-specific fluorescent data trace is independent, both simulation and analysis were parallelized and applied to Georgia Tech PACE computing resources. An average of 30 cores per simulation and analysis was utilized, further multiplying the previous gains in efficiency by well over an order of magnitude.

5.3.2 Experimental Methods

Preliminary experimental results were acquired on an inverted Olympus IX-70 microscope with a 100 μm diameter fiber as a pinhole and means of transmission to a Perkin-Elmer single photon counting module. A 633 nm helium neon laser was used at 20 μW and aligned onto a 670 nm longpass dichroic mirror. In-house Labview software (National Instruments, version 8.6) was written for data collection providing up to 12.5 ns timing for photon arrivals. Olympus 100x 1.4 NA, or 60x 1.45 NA oil objectives were used in an IX-70 inverted fluorescence microscope.

5.4 Simulation and Experimental Results

To improve resolution below the diffraction limit via SOFI, application of cumulants must reduce the PSF width and provide additional resolution between two otherwise overlapping fluorophores. Initially, this is demonstrated in terms of the full-width at half maximum (FWHM) for simulated fluorescence arising from Gaussian point spread functions. Experimental work was initially performed using Ag-DNA clusters and was most effective using long (1.5 s) dwell times.[15] As with previous work, areas that showed broad emission were narrowed, but no super-resolution was obtained from single emitters beneath overlapping PSFs. For this reason, this chapter is focused on simulation for improving previous methodologies and characterizing important photophysical characteristics for future experimental work.

5.4.1 Simulation Results

In general, it is somewhat trivial to demonstrate narrowing of the PSF using simulations in MatLab, although narrowing of the PSF alone does not actually demonstrate increased resolution. Shown in Figure 5.1, individual fluorescence data traces were simulated at a series of grid positions about a Gaussian PSF intensity profile, replicating a confocal raster scan over a single emitter. Independent data traces were collected at each point and a cumulant was applied to each independent trace, resulting in a series of cumulant values as a function of position. The full-width at half maximum (FWHM) of the resulting cumulant map was analyzed to determine a relationship

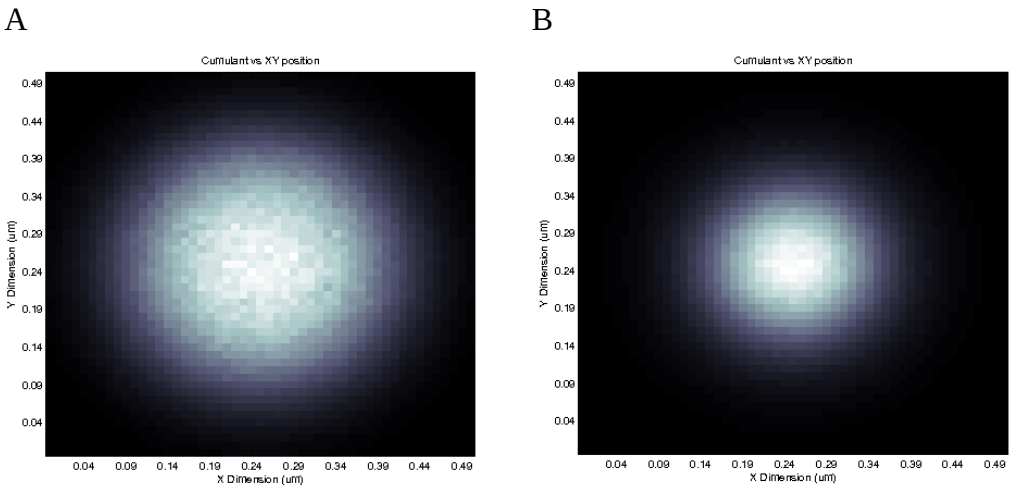

Figure 5.1. Demonstrated narrowing of PSF of a single emitter. (A) shows the total fluorescence image, (B) shows the second order cumulant.

between PSF width and cumulant order. Analysis was repeated using the same simulated fluorescence signal but increasing cumulant order to determine the relationship between PSF width and cumulant order. This is shown in Figure 5.2 which represents the expected narrowing of the PSF (points) vs a simple $1/\sqrt{n}$ plot (black line). The difference between simulated narrowing and expected narrowing is a result of reduced fluorescence collected

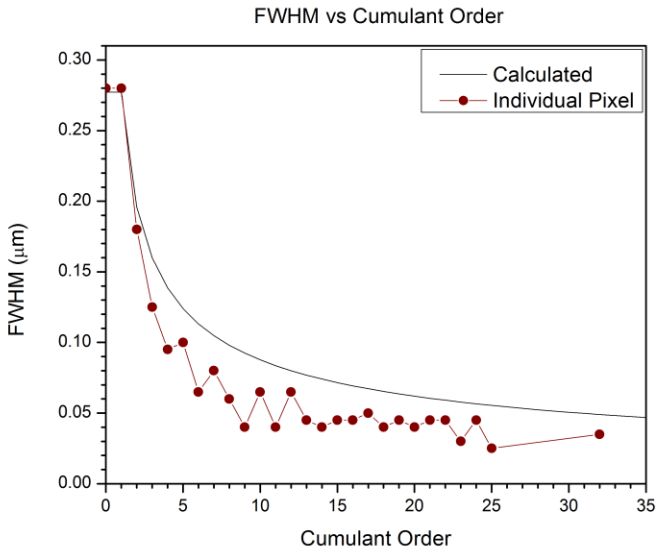

Figure 5.2. FWHM of the PSF vs cumulant order. The theoretical $1/\sqrt{N}$ is compared to single-point autocumulants.

at each point in an effort to represent a more widely available emitter with limited photostability. As a result, cumulants are less able to extract the unique blinking statistics, resulting in a lower cumulant value and artificially greater narrowing of the PSF. However, as a whole, the expected narrowing does approximately follow a $1/\sqrt{n}$ relationship.

5.4.1.1 Importance of Fluorescence Binning

For the successful application of SOFI to fluorescent signals, binning faster than the off state lifetime is absolutely necessary such that blinking due to dark states are apparent in the fluorescence data trace. Without any binning, fluorescence fluctuations are dominated by noise and difficult to properly distinguish between on and off states. This is an important parameter to correlations, and important for properly subtracting off lower order contributions. Without binning, lower order subtractions simply subtract portions of the total fluorescence instead of subtracting lower order correlations. This

A B

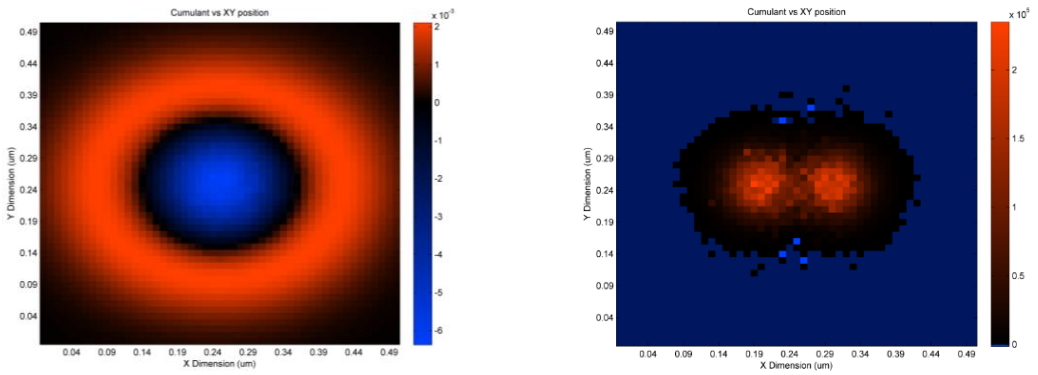

Figure 5.3. Comparison between non-binned (A) and binned (B) fluorescent photons prior to performing cumulant analysis. In this simulation, fluorophores with a 10 μs dark state lifetime were separated by 100 nm, and 10 nm step size. Both images are eighth order autocumulants.

centralized subtraction pattern is evident in Figure 5.3, where two fluorophores are spaced 100 nm apart, with a 10 nm step, 33 ns time resolution, 1 s dwell time, and a 10 μs dark state lifetime. Figure 5.3A is an eighth order cumulant performed on unbinned data (30 ns time step), and demonstrates a subtraction of centralized portions of the cumulant, leaving an almost doughnut shape. This is noticeably absent in Figure 5.3B, demonstrating two separate emitters. Increasing the numbers of photons per bin provides a greater amount of information in each time bin, clearly delineating between on and off states. It also has the added benefit of avoiding the situation where bins with zero value are mean subtracted, which would yield a negative value. Clear blinking is crucial to the function of a cumulant which relies on clear fluctuations in the fluorescence.

5.4.1.2 Important Photophysical Characteristics

Using excitation powers that maximized fluorescence, a parameter sweep was performed across varying dark state lifetimes. In an effort to demonstrate experimental relevance, the average fluorescent rate was set at 2.5×10^5 counts/sec, while varying the dark state lifetime. As a result, the excitation intensity was determined according to

Equation 5.16 through Equation 5.19 where I_{avg} is the average intensity, k_{exc} is the excitation rate, τ_{on} is the on time and τ_{off} is the dark state lifetime. Furthermore, in Equation 5.17 and Equation 5.18, Φ_{isc} is the dark state quantum yield, I_{exc} is the excitation intensity, σ is the absorption cross section, λ is the wavelength, h is Planck's constant and c is the speed of light. I_{sat} is the saturation intensity, determined by the fluorescent lifetime, τ_{fl}. Dwell times were determined from the Gaussian distribution of fluorescence

$$I_{avg} = k_{exc} \frac{\tau_{on}}{\tau_{on} + \tau_{off}} \quad \text{Equation 5.16}$$

$$\tau_{on} = \frac{1}{k_{exc}\, \Phi_{isc}} \quad \text{Equation 5.17}$$

$$k_{exc} = \frac{I_{exc}}{1 + \frac{I_{exc}}{I_{sat}}} \sigma \frac{\lambda}{h\, c} \quad \text{Equation 5.18}$$

$$I_{sat} = \frac{1}{\tau_{fl} \sigma} \frac{h\, c}{\lambda} \quad \text{Equation 5.19}$$

across all positions, such that the sum total of average fluorescence rate at all positions multiplied by the uniform dwell time equals the total number of photons. This is not an exact measure due to the stochastic nature of blinking, but it provides a convenient means to test photostability and in practice was no more than 20% different than the total recorded photons.

Results for a simulation of two fluorophores with 1-Φisc fluorescence quantum yield and unity detection efficiency are shown in Table 5.1. Binning is inherently limited by the blinking statistics and bin duration was set to 1/10 the dark state lifetime. Fluorophores in Table 5.1 were all separated by 170 nm (Sparrow criterion).

Unsurprisingly, the longer the dark state lifetime, the more cumulants that appeared to successfully separate the two fluorophores (i.e. a visible dip between the two

narrowed PSFs). This is in part due to the longer and thus better defined 'off' vs 'on' states. It was also due to larger time bins as a result of longer dark state lifetimes leading to more well-defined statistics for cumulants to operate on. This led to some general principles for selection of appropriate fluorophores including photostability, photophysical on and off times, dark state quantum yields, fluorescent lifetimes and excitation rates.

Table 5.1 Photophysical parameters used to simulate two fluorophores maximally separated such that no dip is present between the two PSFs. Autocumulants up to order 32 that could successfully separate the two fluorophores are reported.

τ_{off} (μs)	Bin (μs)	k_{exc} (1/s)	Dwell (ms)	Total Photons (per fluor, x 10^5)	t_{off}/t_{on}	kExc*Bin (photons/bin at max intensity)	Max order that works	Other Functional Orders
1	0.1	251256	219	9.40	0.01	0.03	0	
2	0.2	252525	219	9.40	0.01	0.05	0	
5	0.5	256410	217	9.50	0.03	0.13	0	
10	1	263158	215	9.50	0.05	0.26	0	
15	1.5	270270	212	9.50	0.08	0.41	0	
20	2	277778	209	9.50	0.11	0.56	0	
30	3	294118	203	9.50	0.18	0.88	4	
40	4	312500	198	9.47	0.25	1.25	0	
50	5	333333	192	9.48	0.33	1.67	3	
60	6	357142	186	9.48	0.43	2.14	3	
70	7	384615	178	9.49	0.54	2.69	3	
80	8	416667	173	9.49	0.67	3.33	32	23,22,20,19-17,13,12,10-5,3
90	9	454545	167	9.48	0.82	4.09	32	25,23,20,18-12,10-5,3
100	10	500000	160	9.50	1.00	5.00	32	25-17,15-12,10-4

Not all orders can successfully resolve two fluorophores. Previous work by Dertinger, *et al.* demonstrated that differences in blinking between otherwise identical QDs appeared 'brighter' in some and 'dimmer' in others after application of cumulant analysis.[7] In a confocal geometry, this variability now takes place on a per-pixel level within a single emitter. The difference in pixel brightness is effectively noise and was

described in previous work by our group.[15] However, this is made worse in the case of limited photostability which mandates a minimal number of pixels. Shorter fluorescence aquisitions, combined with decreases in the total number of pixels resulting from reduced photostability significantly magnifies the problem and reduces the overall effectiveness of SOFI.

Although average fluorescence rates were used to compare the importance of dark state lifetimes, it is in general best to maximize the fluorescence rate to increase the number of photons per bin. However, application of very high excitation powers will force electronic transitions to maximal rates, saturating total collected fluorescence and subsequently widening the PSF artificially, leading to a more 'flat-top' appearance of the PSF. As a result, total summed fluorescence images for high excitation rates appear far more similar for varying fluorophore separations. Thus, it is important to compare the subsequent narrowing of the PSF from SOFI to non-saturated fluorophores obtained at sub-maximal excitation rates.

The question of photostability was next addressed using maximal excitation rates. For this, high performance computing resources at PACE (www.pace.gatech.edu) were utilized, running 8 different separations with 23 different total photon counts. Simulations were run at 50 nm steps with a 4 ms dwell time and a detection efficiency of 0.05. As the only parameters that varied were the separation between fluorophores and total photons recorded, one would expect a relationship between the total functional cumulant orders (ones that show two fluorophores with a visible dip between) and the number of photons present. Shown in Figure 5.4, no clear relationship was apparent between total collected photons and the number of cumulant orders that can successfully separate two overlapping emitters. This result was unexpected, as more total photons were expected to result in better cumulant statistics. It re-emphasizes the importance of fluorophore blinking statistics over photostability, suggesting the potential of organic dyes and fluorescent proteins for SOFI.

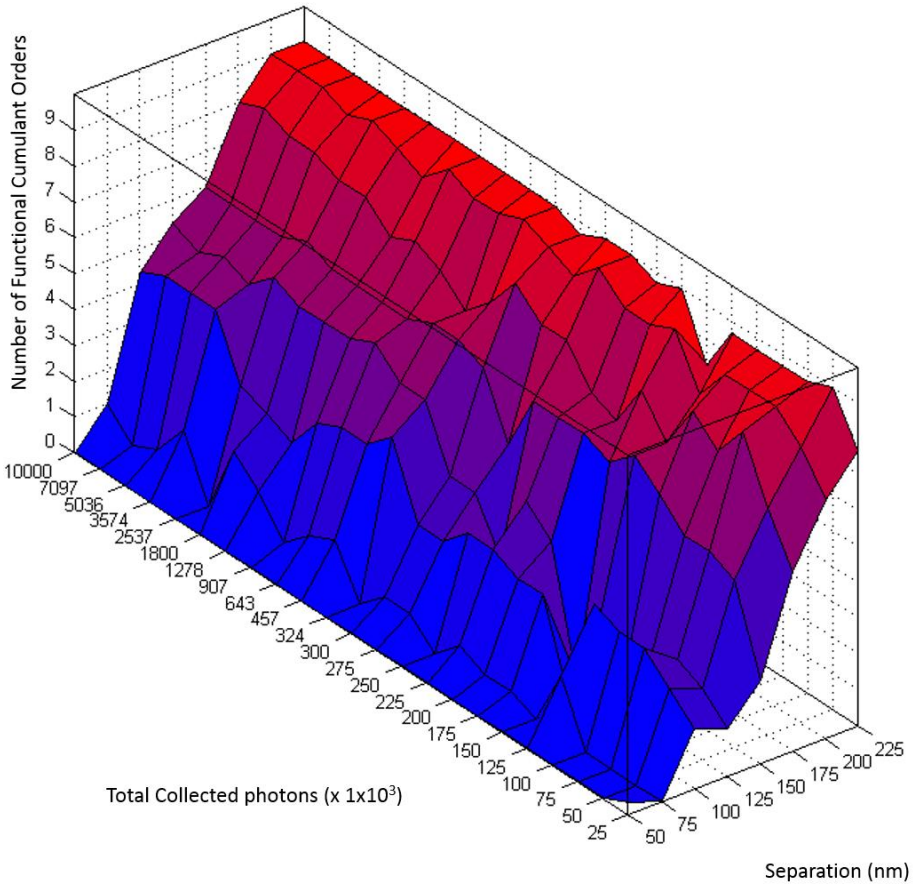

Figure 5.4. Total functional autocumulant orders (colorized, z axis) as a function of both separation between fluorophores and total photons collected.

Optimal fluorophore selection, from the perspective of maximizing cumulant effectiveness, is largely influenced by a strong fluorescence signal while the fluorophore is in an on state and clearly defined off states. This way, the independence between two different blinking fluorophores is the most apparent. Longer, well-defined off states are important, but also maximal photons during on times are also very important. As a result, low dark state quantum yields and shorter fluorescence lifetimes are most effective in improving SOFI (Equation 5.17, Equation 5.20, and Equation 5.21), where Equation 5.20 and Equation 5.21 are simplifications of Equation 5.18 and Equation 5.19, respectively.

$$k_{exc} \propto \frac{I_{exc}}{1 + \frac{I_{exc}}{I_{sat}}}$$ Equation 5.20

$$I_{sat} \propto \frac{1}{\tau_{fl}}$$ Equation 5.21

Subsequently, rhodamine 6G was tested as a potential candidate for super-resolution imaging. Rhodamine 6G has a high fluorescent quantum yield (0.9), low dark state quantum yield (0.008), relatively short fluorescent lifetime (5 ns), and long dark state lifetime (200 μs). Super-resolution was observed in simulations of rhodamine 6G, shown in Figure 5.5. Simulations of Cy5 and Ag DNA did not demonstrate any resolution improvements likely due to low fluorescent quantum yields (~ 0.3 each).

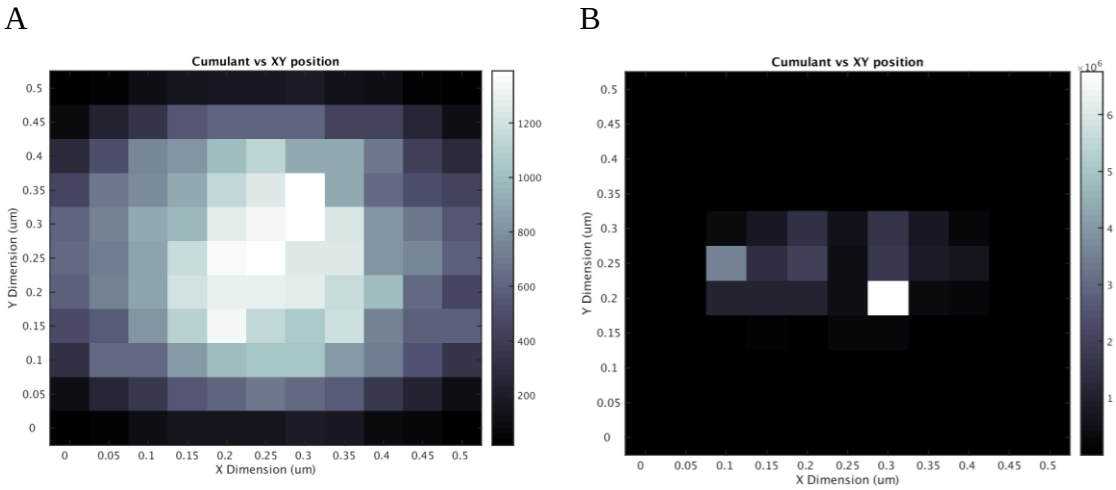

Figure 5.5. Autocumulants of rhodamine 6G, collected within the experimentally relevant photophysical parameters: 0.9 fluorescence quantum yield, 0.008 dark state quantum yield, 4.4 ns fluorescence lifetime, 200 μs dark state lifetime, 4.8 x10^4 cm^{-1} absorption cross-section, 4x10^4 total photons, 50 nm step size. (A) Summed fluorescence signal. (B) Seventh order autocumulant.

5.4.2 Experimental Results

Analogous to previous work in our group, initial experiments were performed with rhodamine 6G and quantum dots (QDs). Collection software was written in-house in

LabView 8.1 with analysis in MatLab. The results in Figure 5.6 don't show resolution improvements, but they did demonstrate narrowing of PSFs. It is not possible to assign positions of fluorophores, and thus the data is only suggestive of resolution improvements. This may very well be due to the non-saturation intensities that were used, and suggest that the assumptions in section 5.2.1, namely that the molecular brightness and stochastic blinking, cannot be assumed to be constants, and thus do not allow narrowing in the same way as the widefield case.

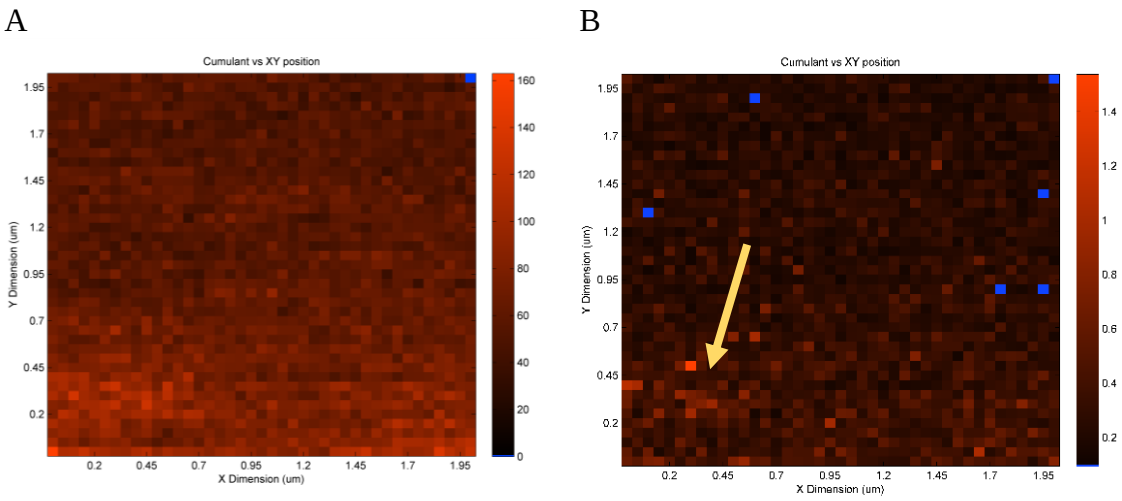

Figure 5.6. Experimental SOFI applied to rhodamine 6G dye using a 4 ms dwell time and ~1.5 mW/cm^2 of 514 Ar^+ excitation. In (A), the bottom left corner appears to have a higher fluorescent signal that is somewhat narrowed in (B) (yellow arrow).

Binning on ms time scales was crucial to obtain any sort of narrowing with QDs. QD present a challenge to SOFI with fast single-element detectors as blinking occurs on all timescales and they may be in a non-emissive state for the entire duration of a single dwell time.[21-24] QD imaging is therefore usually better suited to slower image capture devices such as CCDs. QD experimental results are shown in Figure 5.7.

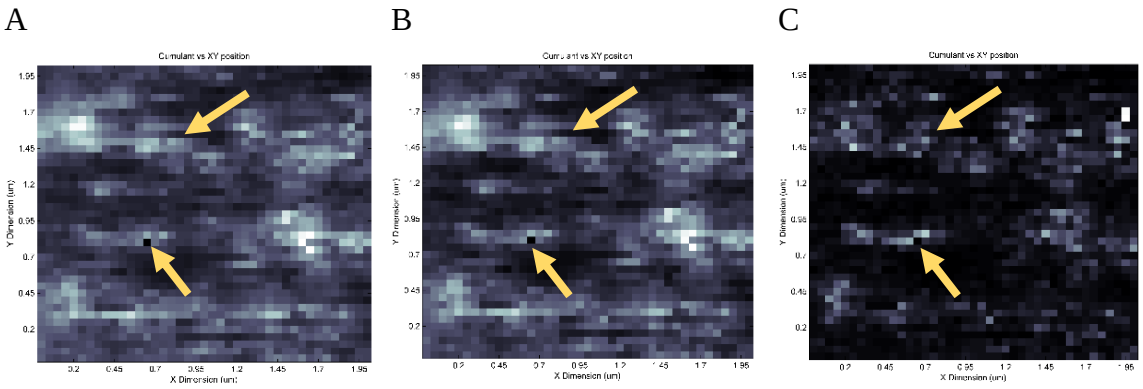

Figure 5.7. Cumulants applied to 605 nm QDs using a 200 ms dwell time and ~5 kW/cm^2 of 514 nm excitation. The experimental fluorescence image is shown in A. Second order autocumulants are applied to (B) using 100 µs binning, with little effect. However, in (C) the second order autocumulant with 10 ms binning yielded some narrowing. Note the black spots in what would appear to be the middle of a QD – a point where a single quantum dot may have been off for the duration of that particular dwell time.

Unfortunately, experimental results were not as successful at narrowing the PSF as computational simulations were. This is largely due to the outcomes of simulation being obtained well after the experimental results, and thus the experimental conditions are poorly configured (i.e. long 4 ms dwell times and low excitation intensities). For these types of experiments, it is crucial that the PSF of the optical system first be characterized and optimized, such that SOFI resolution improvements can be quantified. As experimental data collection and simulations were done in parallel, the optimized parameters were not applied to experimental data. This is an area for future efforts. Finally, a piezo stage was used to scan a sample and obtain confocal fluorescence. Although it may be a small contribution, slight variations in position as a result of piezo creep and hysteresis may have increased noise. This could be remedied by using laser scanning instead of stage scanning, and removing the piezo stage altogether.

5.4.3 Other SOFI Approaches

Initially, it was thought it would be possible to very rapidly 'dither' the excitation laser circularly in two dimensions while collecting fluorescence and assign each recorded photon a two-dimensional position. Provided the rotation is significantly faster than the fluence rate, fluorescence intensity is simply divided by the number of positions. This would have the advantage of spatially scanning significantly faster than the time the emitter could blink and thus make it possible to apply cross cumulants between positions as previously performed on CCD-based cumulants (Figure 5.8).

Rapid laser dithering was computationally simulated by dithering in a circular pattern, dividing the resulting fluorescence into repeating multiple discrete dithered position each associated with a position. Cumulants were then performed on each individual trace or by applying multivariate cross-cumulants across positions. The multivariate cross cumulants were determined using equidistant positions, such that the resulting cross cumulant value yielded a position in the center of the dithered beam (Figure 5.8).[14] In addition to circular dithering, discrete positions about a central point were also tested. In all dithering with fluorophores of limited photostability, significantly fewer cumulant orders were successful at resolving overlapping PSFs, resulting in only the lowest (third to fifth) orders being effective. In general, the more positions in the fast laser displacement that were incorporated, the fewer orders that were successful. This can be understood by considering the need for maximized binning combined with the limitation of fluorescent dark state lifetimes, mandating maximal excitation rates from single emitters. As a result, dithering a laser and dividing the fluorescence trace between positions subsequently lowers the fluorescence fluency for each position. Thus in general, it is not advantageous to attempt cross cumulants on fluorophores with μs blinking by rapid laser dithering.

In addition to dithering, repetitive raster scans were explored. In this simulation the dwell time was divided by the number of scans, and the entire 2D space was fully

scanned before the repeated measurements were made. SOFI applied to multiple scans was less able to successfully resolve two emitters with limited photostability when compared with simply using a single data trace. For a single scan, a dwell time that is dependent on the PSF, step size, and average photostability would yield approximately 500 μs. Given the relatively short dwell times in the absence of multiple scans (10's-100's of μs), insufficient fluorescence and thus poor statistics were obtained, leading to greater noise in the sum of cumulants performed on multiple short fluorescent traces series versus a single longer fluorescent trace. Four to five passes leads to a dwell time that approaches dark state lifetimes, significantly increasing the chances of collecting zero photons for a single dwell time.

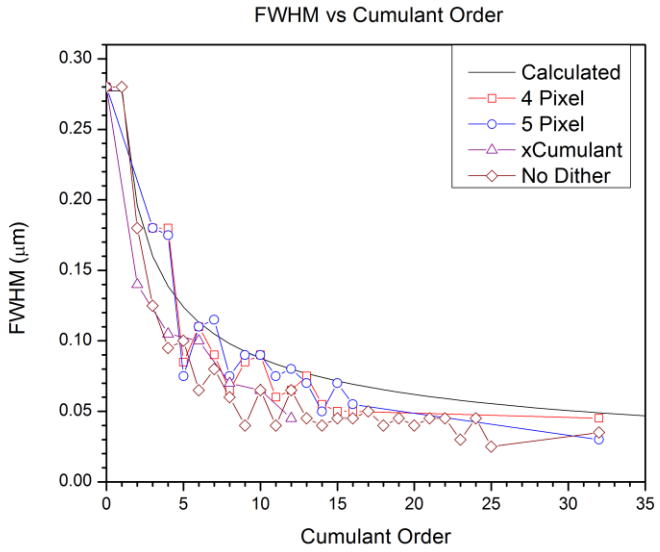

Figure 5.8. FWHM of the PSF vs cumulant orders. The theoretical $1/\sqrt{n}$ is compared to single-point autocumulants (No Dither), a dithering laser occupying four discrete points (4 Pixel) computed with autocumulants, a dithering laser with four discrete points plus a central nondithered (5 pixel) autocumulants, and 4-pixel cross cumulants (xCumulant).

5.5 Conclusions

The need for higher resolution imaging to characterize biological processes has led to the development of super-resolution techniques. SOFI applied to single element

detectors provides access to a significantly larger range of fluorophores blinking in the µs time range while maintaining compatibility with conventional confocal microscopy. In this chapter, the previous SOFI simulations of single element detectors reported by our group were expanded to more physically relevant conditions by collecting independent fluorescent time traces as a function of 2D scan position. Improvements in computational efficiency were applied, providing access to high order auto- and cross cumulants. The importance of binning fluorescence is demonstrated, along with selecting fluorophores with optimal photophysical characteristics such as high fluorescence quantum yields, low dark state quantum yields, and maximal excitation intensities. Fluorescent emitters were tested in simulations designed to compare recovery of resolution as a function of photophysically measurable quantities, and the organic dye rhodamine 6G was shown to be a promising candidate for future computational simulations and experimental studies. These types of photophysical characteristics emphasize a high fluorescence fluence rate while in an on state and relatively long off states, clearly delineating between on and off states. Photostability was not as important as off times and excitation rates, provided dwell times are long enough to collect sufficient photons.

5.6 References

1. Stephenson, J. W. "Observations on Professor Abbe's Experiments illustrating his Theory of Microscopic Vision." *The Monthly Microscopical Journal*, **1877**, *17*, 82-88.

2. Abbe, E. "XV.—The Relation of Aperture and Power in the Microscope (continued)*." *Journal of the Royal Microscopical Society*, **1883**, *3*, 790-812.

3. Hecht, E. *Optics*; 4th ed.; Addison-Wesley: Reading, Mass., 2002.

4. Huang, B.; Bates, M.; Zhuang, X. "Super resolution fluorescence microscopy." *Annual Review of Biochemistry*, **2009**, *78*, 993-1016.

5. Patterson, G.; Davidson, M.; Manley, S.; Lippincott-Schwartz, J. "Superresolution Imaging using Single-Molecule Localization." *Annual Review of Physical Chemistry*, **2010**, *61*, 345-367.

6. Moerner, W. E. "New directions in single-molecule imaging and analysis." *Proceedings of the National Academy of Sciences*, **2007**, *104*, 12596-12602.

7. Dertinger, T.; Colyer, R.; Iyer, G.; Weiss, S.; Enderlein, J. "Fast, background-free, 3D super-resolution optical fluctuation imaging (SOFI)." *Proceedings of the National Academy of Sciences of the United States of America*, **2009**, *106*, 22287-22292.

8. Cox, S.; Rosten, E.; Monypenny, J.; Jovanovic-Talisman, T.; Burnette, D. T.; Lippincott-Schwartz, J.; Jones, G. E.; Heintzmann, R. "Bayesian localization microscopy reveals nanoscale podosome dynamics." *Nature Methods*, **2012**, *9*, 195-200.

9. Gordon, M. P.; Ha, T.; Selvin, P. R. "Single-molecule high-resolution imaging with photobleaching." *Proceedings of the National Academy of Sciences of the United States of America*, **2004**, *101*, 6462-6465.

10. Cox, S.; Jones, G. E. "Imaging cells at the nanoscale." *The International Journal of Biochemistry & Cell Biology*, **2013**, *45*, 1669-1678.

11. Cox, S. "Super-resolution imaging in live cells." *Developmental Biology*, **2015**, *401*, 175-181.

12. Müller, J. D. "Cumulant Analysis in Fluorescence Fluctuation Spectroscopy." *Biophysical Journal*, **2004**, *86*, 3981-3992.

13. Dertinger, T.; Heilemann, M.; Vogel, R.; Sauer, M.; Weiss, S. "Superresolution Optical Fluctuation Imaging with Organic Dyes." *Angewandte Chemie International Edition*, **2010**, *49*, 9441-9443.

14. Dertinger, T.; Colyer, R.; Vogel, R.; Enderlein, J.; Weiss, S. "Achieving increased resolution and more pixels with Superresolution Optical Fluctuation Imaging (SOFI)." *Optics Express*, **2010**, *18*, 18875-18885.

15. Nicovich, P. R. *Widefield Fluorescence Correlation Spectroscopy.* PhD Thesis, Georgia Institute of Technology, 2010.

16. Mendel, J. M. "Tutorial on higher-order statistics (spectra) in signal processing and system theory: Theoretical results and some applications." *Proceedings of the IEEE*, **1991**, *79*, 278-305.

17. Weiss, S. "Fluorescence Spectroscopy of Single Biomolecules." *Science*, **1999**, *283*, 1676-1683.

18. Bilodeau, M.; Brenner, D. *Theory of multivariate statistics*; Springer: New York, 1999.

19. Rose, C. S., Murray D. *Mathematical Statistics In Mathematica*; Springer: New York, 2002.

20. Lawson, C. L.; Hanson, R. J.; Krogh, F. T.; Kincaid, D. R. "Algorithm 539: Basic Linear Algebra Subprograms for Fortran Usage [F1]." *ACM Transactions on Mathematical Software*, **1979**, *5*, 324-325.

21. Nirmal, M.; Dabbousi, B. O.; Bawendi, M. G.; Macklin, J. J.; Trautman, J. K.; Harris, T. D.; Brus, L. E. "Fluorescence intermittency in single cadmium selenide nanocrystals." *Nature,* **1996**, *383*, 802-804.

22. Efros, A. L.; Rosen, M. "Random Telegraph Signal in the Photoluminescence Intensity of a Single Quantum Dot." *Physical Review Letters,* **1997**, *78*, 1110-1113.

23. Krauss, T. D.; Peterson, J. J. "Quantum dots: A charge for blinking." *Nature Materials*, **2011**, *11*, 14-16.

24. Galland, C.; Ghosh, Y.; Steinbrück, A.; Sykora, M.; Hollingsworth, J. a.; Klimov, V. I.; Htoon, H. "Two types of luminescence blinking revealed by spectroelectrochemistry of single quantum dots." *Nature,* **2011**, *479*, 203-207.

CHAPTER 6

SINGLE PARTICLE TRACKING

6.1 Introduction

Unsynchronized, infrequent, or weakly detectable processes benefit can from a single-molecule level of study. However, due to weak single-molecule signals, immobilization is frequently employed and has enabled the study of otherwise inaccessible systems.[1,2] However, many systems of study are strongly perturbed by immobilization or simply cannot be studied while anchored to another component or surface.[2-4] As a result, the methods capable of studying a single particle freely diffusing in a fluid medium were developed, referred herein as single particle tracking (SPT). Monitoring a freely diffusing particle removes the restrictions of immobilization, providing a means for mechanistic insight into biological processes by performing experiments in environments that more closely represent that of a living cell.

One of the earliest descriptions of real-time optical tracking in microscopy was a proof of concept for tracking single bacteria.[5] Comprised of optical fibers connected to photomultiplier tubes, differences in measured voltages drove an electromechanical transducer stage which countered diffusive motion. Piezoelectric stages were later implemented, first by Ha, *et al.* who used a piezoelectric translation stage and lateral steps to center single immobilized fluorophores in a confocal microscope.[6] A theoretical work was later published suggesting the displacement of a single laser instead of the stage to track diffusing fluorophores in two dimensions (2D).[7] Experimental realizations of this displaced laser were later reported, which rely on small servo mirrors or acousto-optical modulators (AOMs).[8,9] In an effort to track in three dimensions (3D), pinholes were combined with quadrant photodetectors or prism mirrors for dividing fluorescence

between photodetectors.[10,11] 3D tracking was more recently reported using a scanning two-photon excitation volume.[12-17] Tracking of individual, freely diffusing single quantum dots in water has been achieved, approaching the single molecule limit and is still some of fastest reported diffusion actively tracked.[18]

Largely based on previous work in the field, development and implementation of a fluorescence-based real-time single particle tracking instrument was started with the goal of studying protein-protein interactions that are too weak or infrequent for more contemporary methods such as fluorescence correlation spectroscopy (FCS).[5,7,9,18,19] Development of an instrument capable of tracking individual diffusing fluorophores is described in this chapter. The theory behind 2D tracking will first be explained followed by 3D tracking. Next, previous contributions to the project and experimental setup will be described followed by the method of calibration. Finally, characterization of the tracking instrument using the diffusion coefficient is presented for both computer and circuit control.

6.2 Method and Design of Single Particle Tracking Instrument

6.2.1 Two Dimensional Estimation of Particle Position

Originally proposed as a theoretical work, fluorescence based tracking method was later experimentally realized and both prior literature reports provide the foundation for the tracking method presented in this chapter[7,9,18,19] The determination of the particle position is crucial to the tracking process and will first be described in 2D for simplicity followed by a 3D description. The method of moving the stage to track a fluorescent particle will follow.

To obtain a positional estimate of a fluorophore in 2D, a laser is displaced laterally in x and y in a sinusoidal manner. By using the same frequency and amplitude of displacement for both x and y, it is possible to create a circular pattern if there is a $\pi/2$ phase shift between the displacements. This is shown in Figure 6.1 where the origin of the plane is at the center of the x and y axes, R represents the radius of laser rotation and w represents the full width-half maximum of the rotating laser beam. The yellow line represents the trajectory of a diffusing fluorescent particle.

A single fluorescent particle centered in the rotating laser would emit constant fluorescence intensity throughout the full rotation of the laser, due to the constant excitation intensity throughout rotation. However, if the particle were offset from the center of the laser rotation, it would experience different laser intensities over time as the laser is rotated. Fluorescence intensity changes would be observed as a result of laser rotation.

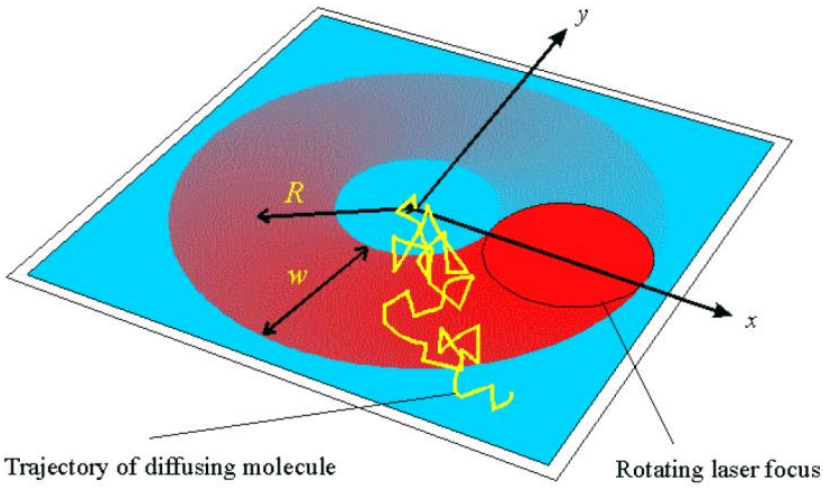

Figure 6.1. Circular laser pattern used to determine particle position. A focused and displaced laser, shown in red with a full-width-half-maximum w, circles about a central point at radius R. The diffusing particle is shown in yellow. Fluorescence collected throughout the rotation is used to determine the position of the particle. Figure adapted from Enderlein, 2000, with permission of Springer.[7]

Fluorescence intensity is directly related to laser excitation intensity, and thus the position of the laser that yields a maximum fluorescence signal is treated as the position of the particle. The position of the laser as a function of time can be represented in Cartesian coordinates by Equation 6.1 and Equation 6.2, where $x_{LaserPos}(t)$ is the position in the x dimension, $y_{LaserPos}(t)$ is the position in the y dimension, R is the radius of rotation, ω is the rotation frequency and t is time. The sine and cosine relationship of x and y is a result of the π/2 phase delay in the laser displacement pattern. The difference between a positive and negative position in x or y is ±π. The laser position corresponding to maximum fluorescence is treated as the particle position because the maximum fluorescence intensity is a result of the position of the laser. An effective method for correlating maximum fluorescence with laser position is through a phase-sensitive lock-in amplifier.[9]

$$x_{LaserPos}(t) = R \cdot cos(\omega t) \qquad \text{Equation 6.1}$$

$$y_{LaserPos}(t) = R \cdot sin(\omega t) \qquad \text{Equation 6.2}$$

Phase-sensitive lock-in detection selectively amplifies a single frequency component above all others in a composite signal, providing a DC output voltage proportional to both amplitude and phase of the individual component. Equation 6.3 and Equation 6.4 represent lock-in detection, accomplished by integrating the product of the fluorescence I(t) with the x displacement of the laser, represented by sin(ωt) where ω is the angular frequency and t is time. This product is integrated over several rotation cycles (t_c) to help average out noise and is subsequently proportional to the particle position. Particle displacements in x and y are phase shifted by π/2 due to the laser position phase shift, and subsequent phase-sensitive lock-in detection is able to resolve the x and y displacements because of the π/2 phase shift. For 2D tracking, lock-in detection is performed simultaneously in x and y dimensions using the same fluorescence signal I(t).

$$x_{ParticlePos}(t) \propto \int_0^{tc} I(t) \cdot cos(\omega t)\, dt \qquad \text{Equation 6.3}$$

$$y_{ParticlePos}(t) \propto \int_0^{tc} I(t) \cdot sin\,(\omega t)\, dt \qquad \text{Equation 6.4}$$

6.2.2 Three Dimensional Estimation of Particle Position

To obtain a 3D particle position, the laser is displaced in 3D, both laterally in x and y dimensions and axially in z. The axial displacement of the laser is accomplished through two different focal depths. These two different axial positions are alternated 5 times faster than the lateral displacement, leading to a laser pattern that has the appearance of two broken circles, shown in Figure 6.2. To determine the axial position,

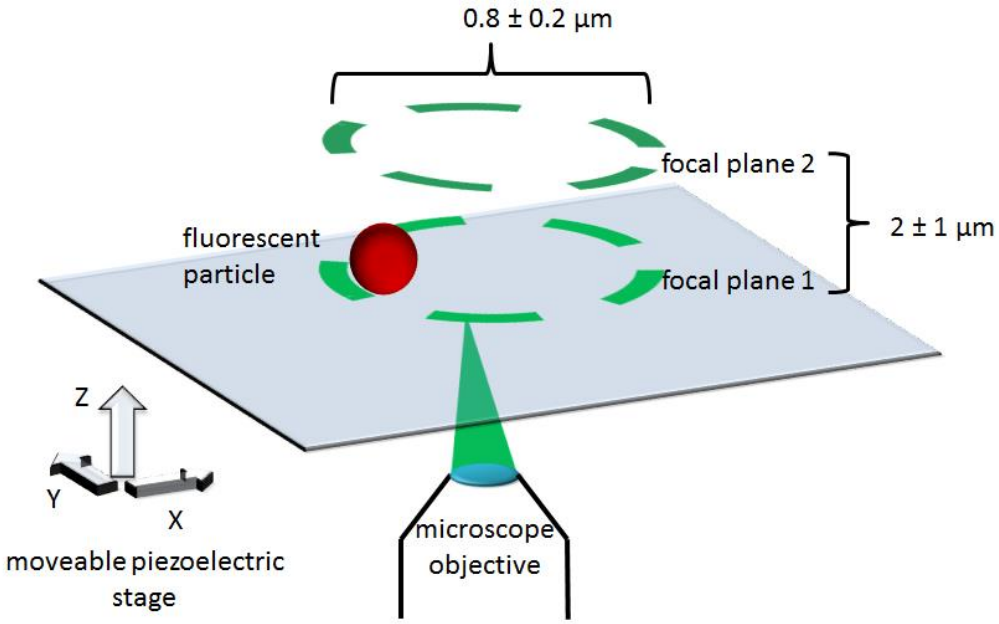

Figure 6.2. Schematic of laser displacement in three dimensions. A single laser (green) is focused through a microscope objective into a sample on a movable piezoelectric stage. The laser is displaced circularly (as in Figure 6.1) at two different focal depths and is switched between the two depths. Lateral circular rotation is at 10 kHz, axial switching is at 50 kHz and the horizontal diameter and vertical spacings are 0.8 ± 0.2 µm and 2 ±1 µm, respectively. The piezoelectric stage is moved to counter diffusion and maintain the fluorescent particle in the focus of the microscope.

lock-in detection is again employed. However, the axial and lateral dimensions use frequencies (50 kHz and 10 kHz, respectively) that are faster than diffusion, low enough for commodity hardware, and different such that they may be easily resolvable. Lock-in detection is frequency specific, so particle displacement in the axial dimension is easily resolved from the lateral dimension.

6.3 Single Particle Tracking

Once positional estimates have been obtained for fluorescent particles, a piezoelectric stage is moved to counter any motions that displace the particle from the center of the laser displacement pattern (Figure 6.2). This was accomplished through either LabView software or a home-built circuit that controls the 3D position of a piezoelectric stage. Stage positions are determined through integral feedback of the lock-in signals, represented in Equation 6.5. In Equation 6.5, $x_s(t)$ represents the next stage position, $L(\tau)$ is the lock-in signal which represents the particle position and G represents a gain factor.

$$x_s(t) = G \int_0^t L(\tau) d\tau \qquad \text{Equation 6.5}$$

The integral feedback combined with the piezoelectric stage, displaced laser, and freely diffusing fluorescent particle to create a closed feedback loop. The loop begins with the particle centered in the detection volume. Due to diffusion, the particle will move toward the edges of the detection volume. Periodic fluorescence signals are then obtained due to the displaced laser. The periodic fluorescence signals are analyzed by lock-in detection, yielding a signal proportional to position. This signal is then sent to the software or circuit, which performed integral feedback and subsequently moved the stage to counter the diffusion of the particle. The stage movement re-centers the particle in the

detection volume, but successive diffusive motions in the particle will cause it to continue moving towards the edges of the detection volume and the process repeats.

6.4 Previous Work

Initial implementation and alignment was completed by graduate student Andrew Khalil (Dickson Lab, Georgia Tech). The optical alignment for tracking particles 3D is depicted in Figure 6.3, where the output from a 633 helium-neon laser is aligned into three AOMs. Each AOM is used to displace the laser in one dimension. The laser is first sent through the x AOM and displaced in one dimension. The second AOM in the y axis

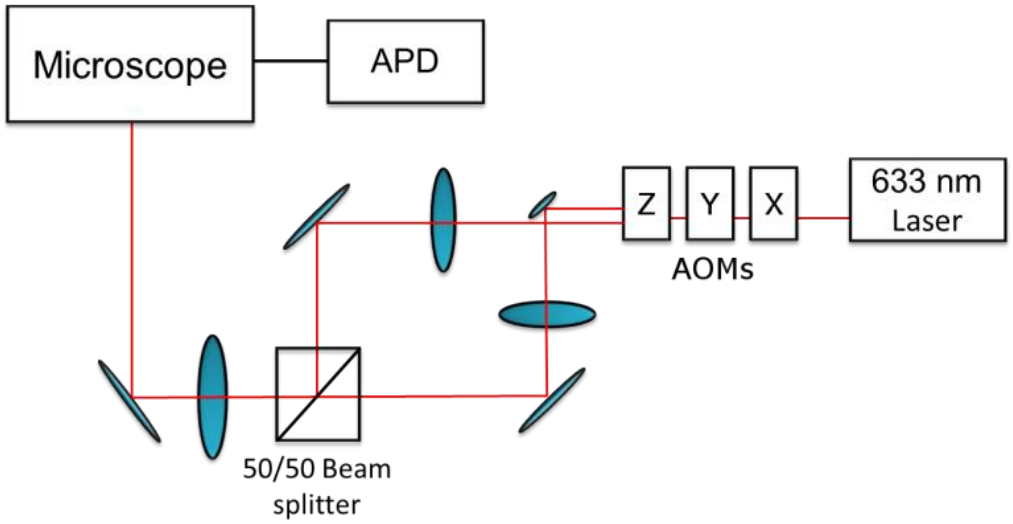

Figure 6.3. Schematic of optical alignment, where a single laser is passed through three AOMs. The first two AOMs dither the beam in a sinusoidal manner in the x and y dimensions. The third AOM is used to alternate the laser between two different beam paths, each with a lens pair that focuses at a different depth in the microscope. The focusing lens pairs use separate first lenses but rely on a 50/50 beam splitter to combine both optical paths through a single second lens. The beam is then aligned into a confocal microscope and fluorescence is collected on an avalanche photodiode (APD).

is aligned to displace the laser orthogonal to the x dimension. When both AOMs are driven sinusoidally at the same amplitude (approximately 10^{-6} degrees) and frequency (10 kHz) with $\pi/2$ phase shift between, the output is a circular pattern. The circle diameter

formed by the displaced laser is 0.8 ± 0.2 μm, and is sufficient for 3D tracking but will be further optimized.[7,19]

A third z AOM is switched on and off at 50 kHz to modulate the laser deflection angle such that when active it directs the laser toward a carefully aligned pick-off mirror, but when not active, the laser passes by the pick-off mirror. The z AOM alternates the laser between two different beam paths, each of which is passed through a pair of telescopic lenses. Each set of lenses allows for a different focal depth in an Olympus IX-70 inverted confocal microscope with a 60x 1.33 numerical aperture (NA) water immersion objective. It was found experimentally that a z AOM frequency of 50 kHz resulted in a lock-in signal with sufficient contrast. Optimal spacing between circles was found to be 2 ± 1 μm, which is close to previously published values.[18]

Fluorescence was collected on an avalanche photodiode (APD) and sent to three lock-in detectors and a computer, shown in Figure 6.4. Fluorescence signals from the APD were recorded on a computer using a National Instruments PCI-6602 multifunction data acquisition (DAQ) card and lock-in signals are recorded using a National Instruments PCIe-6361 DAQ card. LabView 8.6 software was used to perform integral feedback, according to Equation 6.5. The positions of the piezoelectric stage were recorded and changed through a universal serial bus (USB) interface in LabView 8.6 software. The piezoelectric stage implemented in this work had a resonant frequency of 200 Hz. To prevent physical damage to the piezo actuators, input frequencies must be below 200 Hz, and thus a 15 ms pause between stage movements was incorporated. Previous work had used a piezo stage with about a 100 kHz higher resonant frequency.[20]

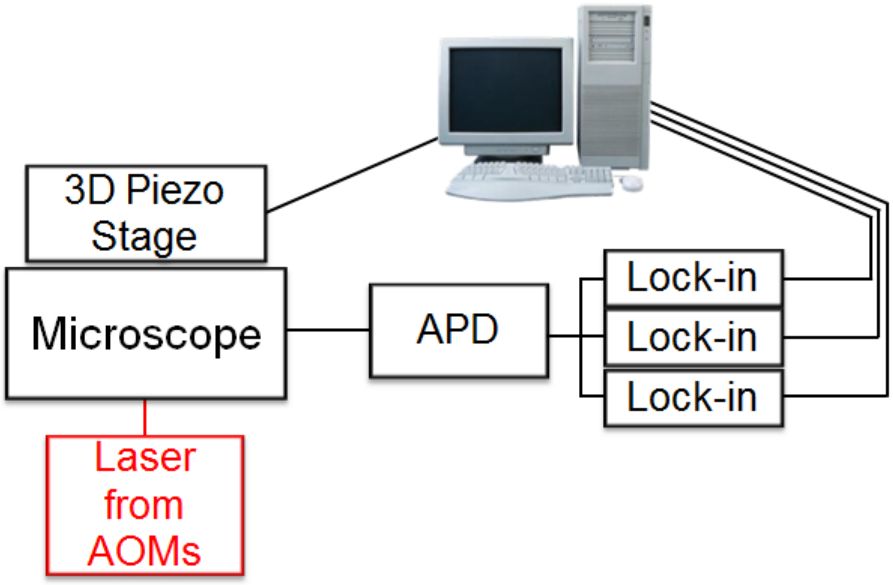

Figure 6.4. Schematic of fluorescence tracking instrument. Fluorescence collected on an optical microscope is sent to an APD and subsequently routed to three lock-in detectors. Each lock-in detector is able to analyze the fluorescence signal for each dimension and subsequently output a signal proportional to the displacement of the particle from the center of the stage. When tracking, LabView computer software was used to analyze the error signals and coordinate successive stage movement such that particle diffusion is countered.

Prior to this thesis work 3D tracking had been accomplished in our lab, but was not reproduced and optical alignment was unstable over a timescale of minutes. It was initially thought that the slow response in computer control was responsible. As previous work had cited circuit control, work on a circuit was completed but remained untested.[20]

The central component of the circuit-based stage control was an operational amplifier (Analog Devices, OP27G) configured as an integrator with an integration time constant long enough to prevent 200 Hz frequency oscillations that damage the piezoelectric stage. An initial design of the circuit was as shown in Figure 6.5 and Figure 6.6. By simultaneously and independently integrating the lock-in amplifiers for the x, y,

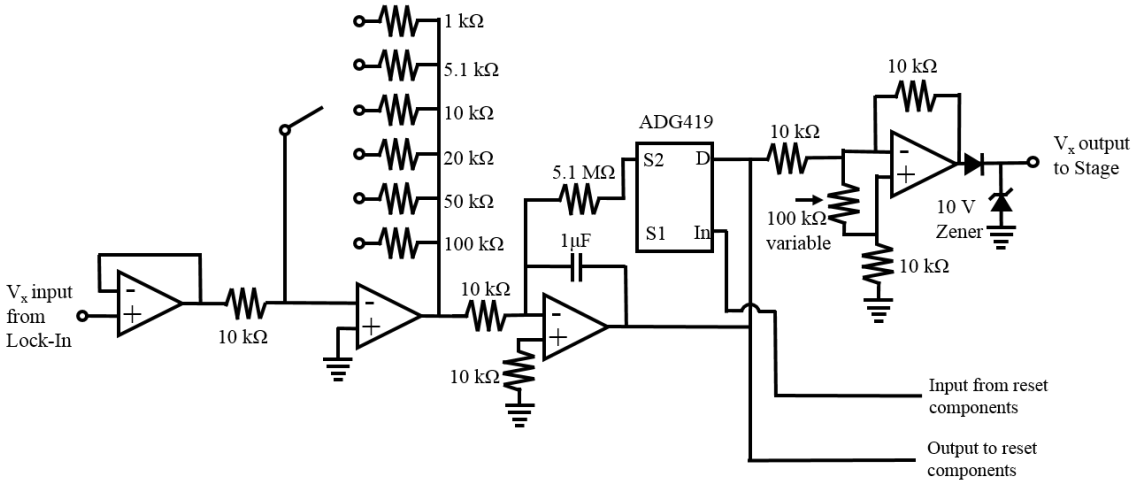

Figure 6.5. Tracking portion of the controlling circuit represented in only the x dimension, as y and z are identical. The tracking portion is comprised of a buffer, variable-gain inverting amplifier, integrator, switch (ADG419), modified inverting summing amplifier, and a Zener diode to prevent voltages >10V. The negative integral feedback is accomplished through the integrator with variable gain through the inverting amplifier. The analog switch is controlled through a separate portion of the circuit, and is normally closed. When the analog switch is opened the output is driven back to the initial position through an RC time-constant of 10 seconds. The final component is a modified inverted summing amplifier, capable of summing a variable voltage such that the initial position of the stage could be adjusted.

and z dimensions, the circuit moves the piezoelectric stage to counter particle motion, executing integral feedback. Each dimension (channel) of the circuit operates independently with a variable gain, integrator, and adjustable positional offset implemented through additional operational amplifiers (op-amps). This part of the circuit is shown in Equation 6.5. Every channel has set limits that when reached, initiate a timed reset back to a central location via a set of comparators, 555 timer and a series of OR gates to reset all channels simultaneously (Figure 6.6). The design differs from previous methods by combining all electronic components together. However, while simpler to experimentally set up, diagnosis of problems and implementation of fixes is difficult as all fixes to all dimensions had to be incorporated into one physical component.[20]

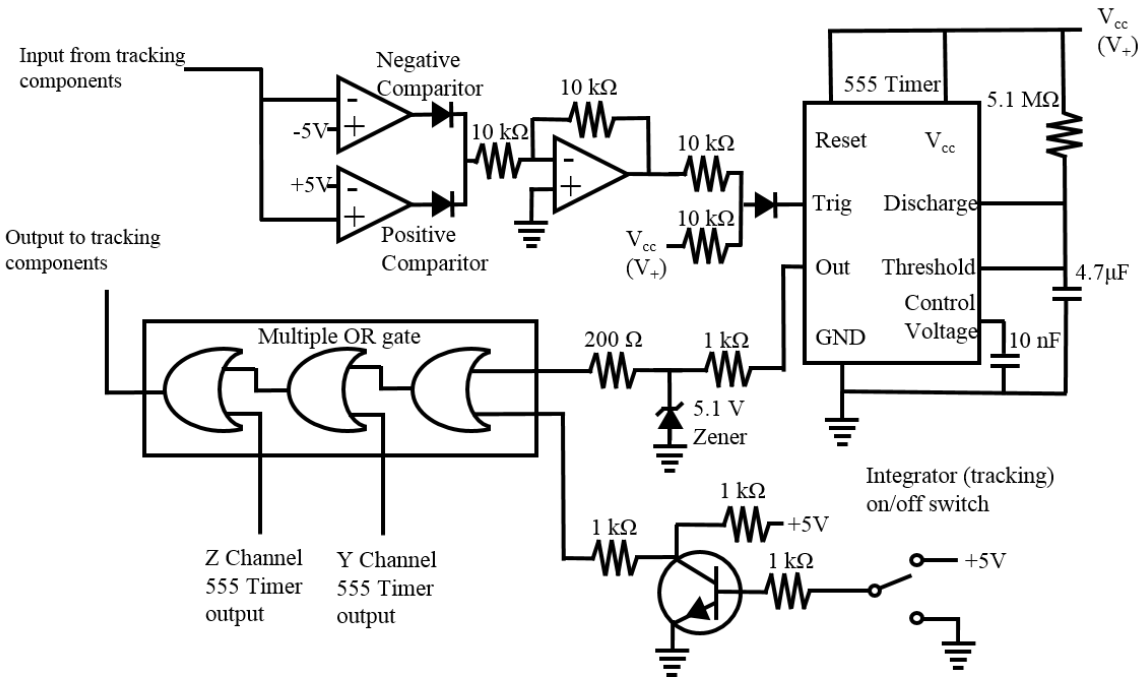

Figure 6.6. Reset portion of the circuit for the x channel which is replicated identically for y and z channels with the exception of the integrator switch and multiple OR gate. The tracking input is recorded on two comparators, which when triggered, send a transistor transistor logic (TTL) high signal to a 555 timer, which is configured to output a 10 second TTL high signal, forcing the tracking portion for all three channels to reset to their initial positions.

6.5 New Contributions to Instrumental Design

Optical alignment is crucial to optimized tracking and any offset in the pitch or roll of AOM alignment would contribute to slower tracking of single particles, resulting from a loss in $\pi/2$ phase shift between x and y laser displacements. A loss of this phase shift makes decoupling particle displacements in x from y via lock-in detection extremely difficult. In this situation, the system would still be capable of tracking but would be limited to slower particle diffusion. AOM mounts were modified such that the roll angle could be precisely adjusted, making the instrument much more sensitive to particle displacements in x and y.

Additionally, initial attempts at optical axial alignment were unsuccessful because it was assumed that the axial position of the two laser foci needed to be aligned

equidistant both above and below the focal plane of the microscope. However, as the z AOM is only able to deflect approximately 80 percent of the laser power into one beam path relative to the other, it was impossible to perform tracking resulting from the weaker of the two beams. Thus, the brighter of the two beams was offset (defocused) in the axial dimension to reduce its fluorescence contribution such that fluorescence from both beams was approximately equal. All reported 3D alignment tracking was accomplished by focusing two beams of unequal power (with axial offset) into a confocal microscope.

This somewhat unconventional alignment was extremely difficult in practice, and thus significant efforts were made to characterize alignment. A single immobilized bead was centered in the microscope and a computer software-based calibration program written in LabView 8.6 is used to characterize the alignment. While the AOMs actively displace the laser in 3D, the software rasters the piezoelectric stage in 3D, pausing to record position, fluorescence, and lock-in signals. A typical output for a well-aligned system is shown in Figure 6.7, where each of the dimensions displays a strong positive to negative error signal (Figure 6.7A-C) that is orthonormal to the other spatial axes. The alignment is considered optimized when motion along one axis causes a minimal change in error signal for any orthogonal axis.

6.6 Tracking Results

6.6.1 Software-Based Experimental Tracking

Successful tracking of 250 nm carboxylate-functionalized polystyrene fluorescent beads has been achieved in PEG solutions over a minutes timescale but no longer than 100 ms in water. Figure 6.8A shows the trajectory of a 250 nm polystyrene fluorescent bead freely diffusing in a 100% PEG-400 solution (90 cP viscosity). Initial attempts to track fluorescent beads in PEG solutions provided a good starting point as isolated individual particles diffusing through the detection volume provided measurable fluorescence signals on the order of seconds before being lost. It was observed that the

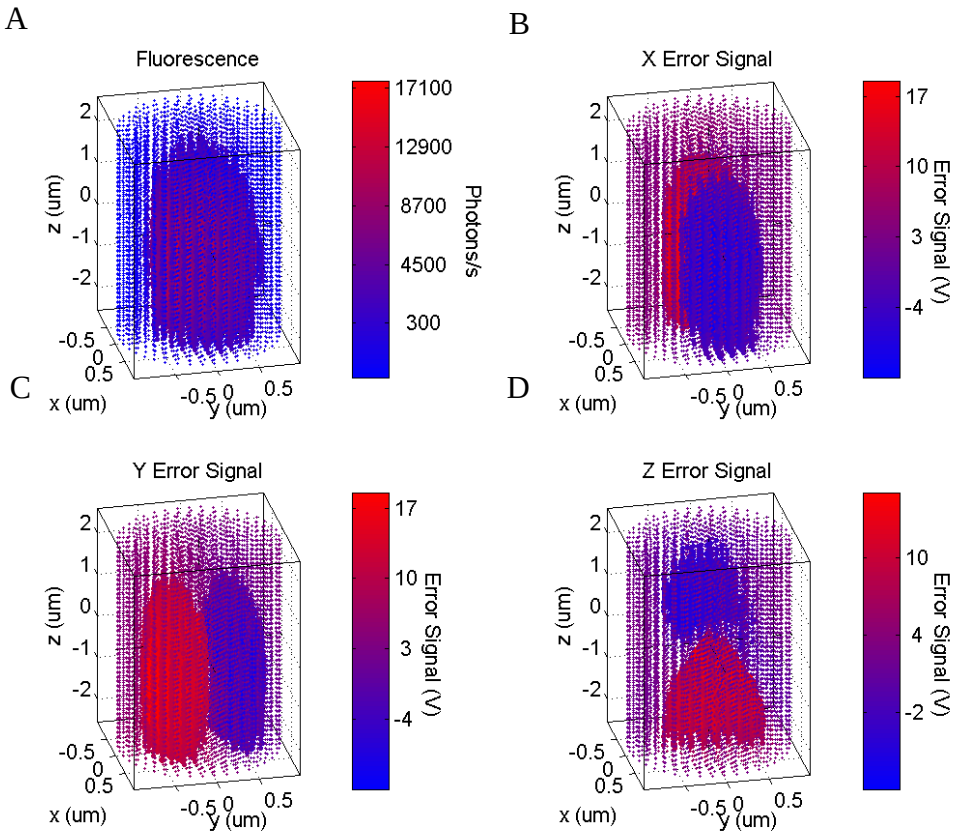

Figure 6.7. A 250 nm fluorescent bead immobilized on a cover slip is moved in 3D while fluorescence and lock-in signals are recorded. (A) represents the fluorescence intensity and in (B), (C) and (D) the x, y, and z lock-in signals, respectively, are shown. Typical for a confocal microscope, a prolate spheroid shape is apparent in the fluorescence, while x, y and z error signals are resolved in their respective dimensions.

system could track in the solution for extended periods of time (>30 minutes) although in such cases it is possible that the slowly photobleached bead could be exchanged for another bead of equal or greater brightness when two beads diffused across the detection volume simultaneously. To minimize the possibility of analyzing a trajectory where a particle is switched out for a brighter one, portions of trajectories with minimal fluorescence spikes or changes are analyzed Figure 6.8B).

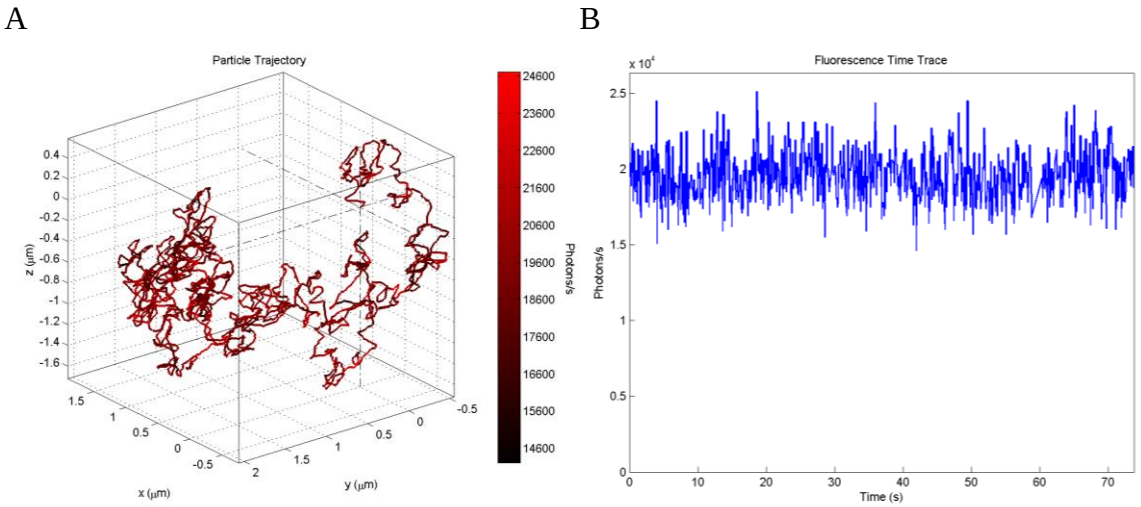

Figure 6.8. In A, a recorded trajectory for a 250 nm polystyrene bead diffusing freely in a PEG solution is shown. In B, the fluorescence intensity is plotted as a function of time. No obvious spikes or dips are present, suggesting a single bead was tracked.

As a means for benchmarking the proper operation of the tracking instrument, diffusion coefficients were calculated for the tracked fluorescent bead and compared to experimental values. The certificate of analysis provided with the polystyrene beads reports a transmission electron microscope (TEM) diameter of 250 ± 9 nm. To obtain an estimate of the diffusion coefficient, the TEM diameter was used to calculate a diffusion coefficient of 0.0195 ± 0.001 $\mu m^2/s$ using the Stokes-Einstein relation. The relation is shown in Equation 6.6, where k_B is the Boltzmann constant, T is temperature, η is the solution viscosity and r is the particle radius. This value of 0.0195 $\mu m^2/s$ should be considered approximate because the beads are carboxylate functionalized and are expected to interact with the PEG solution, yielding a different hydrodynamic radius.

$$D = \frac{k_B T}{6 \pi \eta r} \qquad \text{Equation 6.6}$$

The diffusion coefficient is also represented as the change in mean square displacement (MSD) in Equation 6.7, where n is the number of dimensions, t is time and

r is position. Thus, the diffusion coefficient can be calculated from the slope of the MSD versus time plot. To gain a statistical advantage, time averaging was applied in the MSD calculation for the trajectory presented in Figure 6.8A, shown in Figure 6.9A. A fit to the slope of the MSD versus time plot yields a diffusion coefficient of 0.018 $\mu m^2/s$.

$$D(t) = \lim_{t\to\infty} \frac{1}{2\,n\,t} \langle |r(t) - r(0)|^2 \rangle \qquad \text{Equation 6.7}$$

To study the diffusion coefficient more directly, the diffusion coefficient was plotted as a function of delay time according to Equation 6.7 (Figure 6.9B). It is important to note that the diffusion coefficient value does vary over time, so the value of 0.018 $\mu m^2/s$ should be considered approximate. The changing diffusion coefficient may partially be due to a slight drift in the focus of the microscope and/or temperature effects of laser. An interesting effect present in Figure 6.9B is the initial spike in the diffusion coefficient that relaxes back down. This could be due to the instrument overcorrecting and moving beyond the particle position, falsely representing a high diffusion coefficient at short times. This effect is minimized at longer times, leveling out to approximately 0.018 $\mu m^2/s$.

When experimental tracking of 250 nm beads was attempted in water (0.9 cP viscosity), the longest recorded trajectories were 0.1 seconds or less. Published work has detailed tracking of smaller (20 nm diameter) particles in less viscous solutions (water) for 25 seconds, so was is proposed that the 15 ms time delay between successive stage motions was responsible for poor tracking of smaller diameter beads.[18] To answer this question more fully, computer simulations were applied to better understand the tracking instrument.

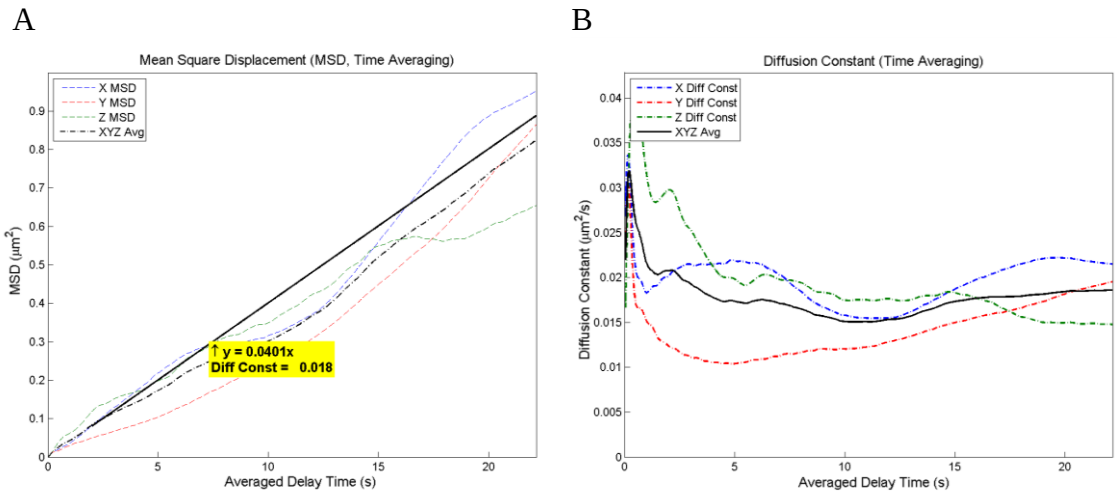

Figure 6.9. In (A), the mean square displacement (MSD) for a single freely diffusing carboxylate-functionalized 250 nm polystyrene bead is plotted as a function of delay time plotted for x, y and z dimensions. A diffusion coefficient of 0.018 $\mu m^2/s$ is obtained from fitting a line to the averaged MSD for each dimension. For each plotted point, an averaged MSD is calculated from all equivalent delay times present in the trajectory. The diffusion coefficient plotted against the delay time in (B), according to Equation 6.7, demonstrating changes over time in the diffusion coefficient.

6.6.2 Circuit-Based Experimental Tracking

While tracking 250 nm fluorescent beads in PEG solutions (90 cP) was possible through software-based tracking, the same beads in water (0.9 cP) was not possible for greater than 0.1 seconds. A 250 nm bead in water has a Stokes-Einstein diffusion coefficient of 0.20 $\mu m^2/s$, but previous literature has reported tracking of diffusion coefficients 100 fold greater using similar methods.[18] There were likely several causes of this related to stage control, software, and the interaction between both. The piezoelectric stage is equipped with a 'closed loop mode' which actively moves the stage to correct for hysteresis and creep in the piezoelectric actuators. However, this active correction may be conflicting with the integral feedback used in tracking fluorescent particles, causing erratic behavior and subsequently losing the particles. The tracking software was also deliberately written to incorporate a 15 ms wait time in an effort to prevent damage to the

piezoelectric stage from high frequency oscillations. This wait time effectively freezes the tracking instrument in place while particles continue to diffuse out of the detection volume. Finally, the use of computer software and a USB interface for controlling the piezoelectric sample stage impose limits on how fast output (stage positions) can be generated as a result of input (lock-in amplifiers, stage position). The time frame of these lags can be as high as tens of milliseconds, making the overall instrument effectively frozen for as long as 30 ms.

As a result, an analog circuit was implemented as an alternative to the discrete wait times and active stage control. This enabled the operation of the stage in the alternate, non-correcting mode by using analog control instead of the digital USB interface. In place of computer control, an analog circuit comprised of operational amplifier building blocks was used. This was expected to provide constant motion of the piezoelectric stage while preventing the damaging 200 Hz oscillations. A computer was still used for data collection, but the control of the stage would not be reliant on the response of a computer.

However, a series of additional problems became apparent which were initially only observable via repetitive resets in the circuit. Initially, a series of op-amp buffers were implemented such that the input voltages from the lock-in amplifiers and integrators could be observed. A very slight voltage offset in the lock-in amplifier would be integrated and ultimately lead to a significant drift when attempting to track fluorophores. As a result, a summing non-inverting amplifier was added before the variable-gain inverting amplifier to manually counteract constant drift. Additionally, a second switch was added in front of the integrator so that no additional integration would take place during the reset, and variable offset limits were added to the comparators to increase the effective tracking range. Finally, an external transistor-transistor logic (TTL) output was added to the circuit to automate the LabView software data collection. The final tracking circuit is shown in Figure 6.10.

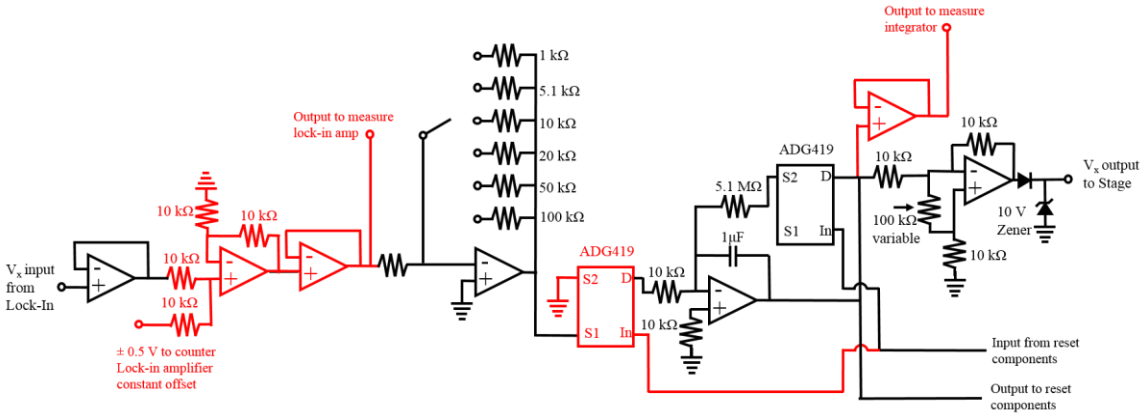

Figure 6.10. Modifications to tracking circuit, highlighted in red. Specifically, a noninverting summing amplifier and buffer were added to manually counter constant offsets present in lock-in amplifier inputs. An output just before the variable-gain inverting amplifier was added. An additional analog switch was added just before the integrator and a buffer such that the integrator value could be output. Not shown are adjustable comparator reset values and an output for recording resets.

Only tracking in two dimensions was attempted due to equipment (stage) limitations, but circuit modifications were made for three dimensions. Tracking was attempted on both 250 nm and 20 nm fluorescent beads in water, shown in Figure 6.11

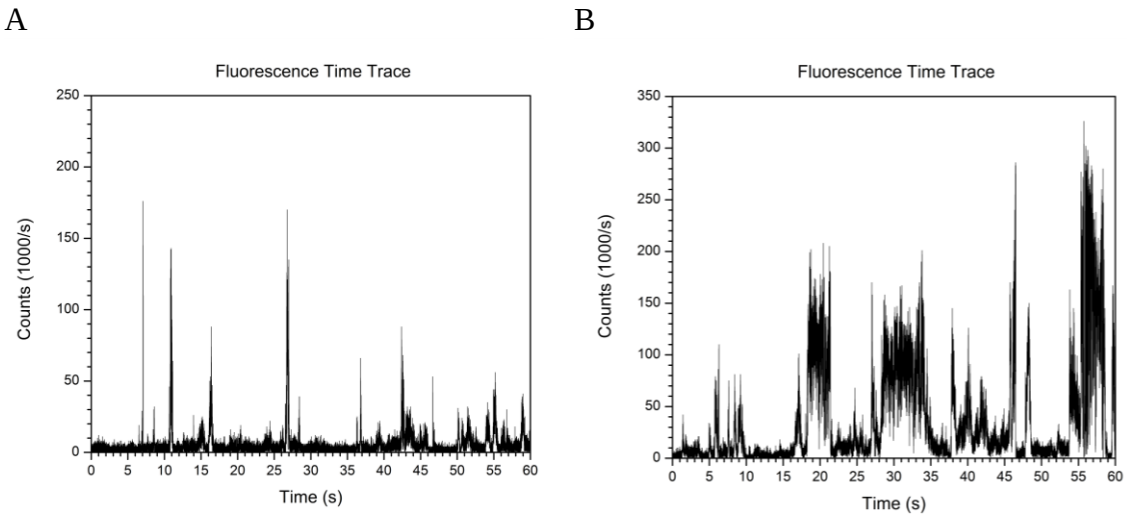

Figure 6.11. Fluorescence time trace of 250 nm beads in water. In (A), tracking was turned off, allowing beads to diffuse through the focus of the microscope during laser displacement. In (B), circuit tracking was enabled, demonstrating extended fluorescent traces, indicating an extension in the time single fluorescent beads were in the focus of the microscope.

and Figure 6.12, respectively. While single trajectories were not maintained out to the limits of the stage, trajectories were clearly extended for the 250 nm beads (Figure 6.11).

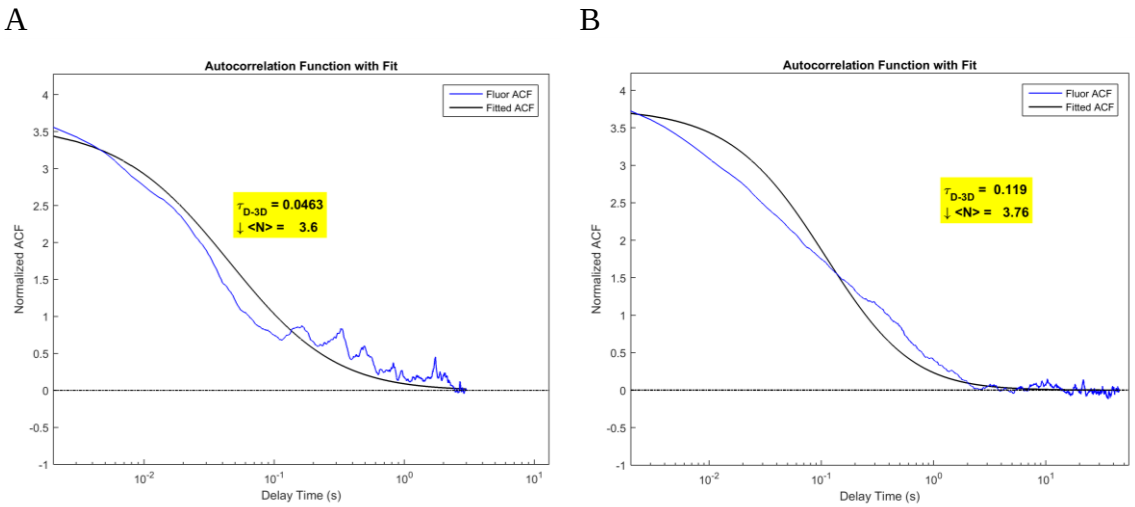

Figure 6.12. Autocorrelation of fluorescence obtained from 20 nm fluorescent beads in water. In (A), approximate fits to autocorrelated data with tracking turned off indicates an average transit time across the excitation volume of ~50 ms. In (B), the transit time is more than doubled with circuit tracking enabled. Fits were made to Equation 6, providing a rough estimate on the diffusion time.

Tracking of 20 nm beads was also attempted, again leading to extended tracking times. Fluorescent time traces were collected using 1 ms binning due to limitations in collection software, and autocorrelations were performed on data collected while tracking was disabled versus enabled. Autocorrelations were fit using Equation 6.8, where N is the number of molecules, $\tau_{(D-3D)}$ is the diffusional time across the excitation volume and κ is the ratio of excitation beam radius in the z axis to excitation beam radius in the xy plane. Fits were similar to diffusive FCS curves, though a non-Gaussian excitation volume coupled with roughly constrained diffusion led to less optimal fits, thus diffusion times should be considered approximate. However, an extension in time spent in the excitation volume was apparent, lending support to the validity of the tracking instrument.

$$\mathrm{F}(t) = \frac{1}{N} \cdot \frac{1}{\left(1 + \frac{t}{\tau_{D-3D}}\right)} \cdot \frac{1}{\sqrt{1 + \frac{t}{\tau_{D-3D}\kappa^2}}} \qquad \text{Equation 6.8}$$

6.7 Computational Simulation

Although the bulk of the work presented is experimental, preliminary simulations have been completed for 2D particle tracking in MatLab. In the simulation a series of bead positions are randomly generated that fit a normal distribution multiplied by the diffusion coefficient. The diffusion coefficient is calculated according to the Stokes-Einstein relation using a 200 nm bead diameter, temperature of 295 K, and appropriate solution viscosity (90 cP for PEG, 0.9 cP for water). Fluorescence intensity as a function of time is calculated according to Equation 6.9, where x and y are the particle positions (μm), ω is the angular frequency (2π·Hz) of laser rotation and w (m) is the radius of laser rotation.[7] Lock-in detection of the simulated fluorescence is applied according to Equation 6.4 and Equation 6.5 with a 10 ms time constant. The result of the Equation 6.4

$$P(x, y, t) = \exp\left(\frac{-2(x - R\cos(\omega t))^2 + 2(y - R\sin(\omega t))^2}{w^2}\right) \qquad \text{Equation 6.9}$$

and Equation 6.5 are used as the new x and y stage positions.

While the simulation provided excellent tracking results for 200 nm beads in PEG, it also reproduced the inability for the current system to track in water for any significant periods of time. This can be seen in Table 6.1, where tracked 200 nm beads in water yield an average trajectory of 31 ms. The maximum tracking time in the simulation was 10 s, and is reproduced for PEG viscosities. Due to the limitations in moving the piezoelectric stage (below 200 Hz, per manufacturer recommendations), a 15 ms wait period between stage motions was incorporated as a safeguard. However, this wait period may be responsible for the poor tracking of beads in water. The stage wait was

Table 6.1. Simulated tracking in varying viscosity for 200 nm diameter particle

Viscosity (cP)	Diffusion Coefficient ($\mu m^2/s$)	Average Trajectory Length (s)	Standard Deviation (s)
0.90 (water)	2.4	0.031	0.039
9.8	0.22	8.0	3.1
19	0.12	10	0
90 (PEG)	0.024	0.024	0

investigated by simulating tracking with varying stage wait periods. The results are shown in Figure 6.13, in which diffusion coefficient plots exhibit increased initial slopes

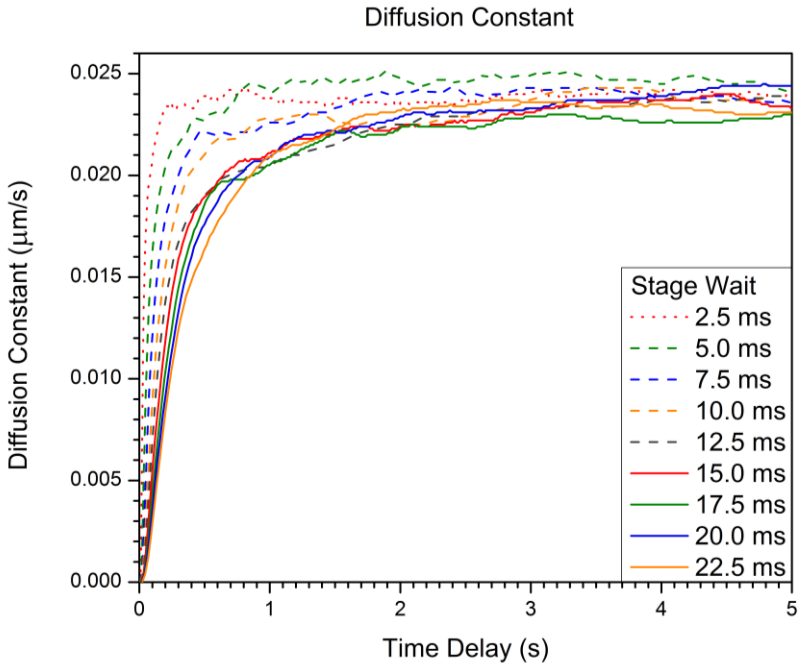

Figure 6.13. Randomly diffusing 200 nm beads were tracked according to a MatLab simulation. In each simulation, all conditions were held constant except for different stage wait periods between successive stage motions. Stage positions were recorded and diffusion coefficients are plotted according to Equation 6.7. In each plot, 2000 total trajectories are averaged. Shorter stage wait periods led to steeper initial slopes, or plots that approach the final diffusion coefficient at an earlier time delay. Accurate reporting of the diffusion coefficient at earlier time delays indicate the tracking instrument was following the particle much more closely and accurately.

when the stage wait period is shorter, meaning the tracking system is following the particle more closely and subsequently reporting accurate diffusion coefficients at earlier times. This earlier reporting indicates that the tracking system is faster and more accurate as a result of decreasing the stage wait period.

6.8 Future Work

6.8.1 Instrumental Design

Tracking alignment in the axial dimension was reliant on a single AOM to deflect between two different beam paths. Due to an 80% deflection efficiency, there was a significant difference in excitation intensity between the two beams, corrected only by aligning the excitation beams at the edge of the confocal detection volume. As a result, fluorescence signal resulting from the brighter of the two beams was partially ignored, and thus very likely responsible for reduced tracking efficiency. However, other alignment geometries circumvented this by relying on separate AOMs to adjust the excitation intensity for each of the two separate foci.[18] Separate AOMs have the distinct advantage of a high level of control for balancing the excitation intensities of each foci without discarding fluorescence from the excitation volume.

Tracking in 3D using the improved circuit has not yet been attempted, due to equipment that was unavailable at the time. While 2D tracking results are promising, 3D tracking is still yet to be attempted. In addition, circuit modifications also may have drawn enough current to affect integrated signals, manifested as a sluggish response. The alignment geometry was also somewhat problematic, as the z dimension relied on the diffraction efficiency of an AOM, which was 80 %. This alignment would then, at best, rely on discerning the difference between two lasers that are 20 % different in intensity. Adopting an alignment more similar to previously reported methods is likely more effective.[18]

Additionally, the design for the current circuit-based setup relied on a single circuit for stage control and integral negative feedback. This would make sense in an enterprise application where manufacturing of a single component is advantageous. However, in the research laboratory, it makes far more sense to design and implement individual circuit components separately to maximize the convenience of testing, replacing and upgrading.

Data collection software needs to be sensitive at a photon-by-photon timing, not simply binned fluorescence. This would likely mean a simultaneous collection regime synchronized with a single clock source (i.e. 20 MHz sync), such that the photon-by-photon and stage position signals could be properly synchronized.

Lastly, progress has been made in SPT such that additional tracking schemes are available. Two-photon excitation reduces out of plane fluorescence, simplifies alignment, and increases penetration depth.[12] Relying on lock-in amplification also reduces the responsivity of the system due to the need for some time averaging, and more recent methodologies forgo dithering altogether.[21] However, due to the need for sufficient sensitivity from single emitters, some level of fluorescence averaging will likely be necessary.

6.8.2 Computational Simulation

While preliminary simulations indicate the 15 ms stage wait period is limiting the experimental tracking of polystyrene beads in water, additional simulations with an analog circuit have not yet been accomplished. Instead of imposing a timed wait period, a low pass filter should be used to simulate the circuit integrator. By carefully tuning the low pass filter, it will be possible to determine the proper circuit components that provide an optimal balance between safeguarding the stage and optimal tracking. This optimization through simulation reduces the trial and error approaches to the physical piezoelectric stage, minimizing the potential of damaging the piezo actuators.

6.9 Applications

The eventual goal of this 3D tracking setup is to perform high-sensitivity SPT in a living cell by incorporating high frequency SAFIRe optical modulation. By sinusoidally modulating the intensity of a defocused long-wavelength laser significantly faster (>10x) than the dithering frequency, the fluorescence signal could first be demodulated (i.e. an additional lock-in amplifier tuned to the modulation frequency) before being passed to tracking lock-in amplifiers. Even in high background, we have demonstrated the ability to recover signals of interest through optical demodulation of fluorescence. Both correlation and Fourier transform methods should be directly compatible with these tracking studies for improved sensitivity and dynamics in complex environments.

6.10 Conclusions

A 3D real-time single particle tracking instrument was built with the goal of exploring weak protein-protein interactions. A detailed explanation of the theory of operation was provided, along with diagnostics for determining optimal alignment utilizing in-house LabView software. 3D tracking of 250 nm diameter beads in PEG solutions was recorded. Initial work on computer simulations of single particle tracking was performed, detailing the need for analog circuit control.

In order to pursue faster diffusion, a homebuilt analog tracking circuit was built using operational amplifiers as a fundamental building block. Modifications to the circuit were made, making 2D tracking of smaller beads possible in aqueous solutions. Remaining work could focus on computer simulations of circuit-based tracking, improved optical alignment, and modular circuit-based controller design.

6.11 References

1. Roy, R.; Hohng, S.; Ha, T. "A practical guide to single-molecule FRET." *Nature Methods*, **2008**, *5*, 507-516.

2. Weiss, S. "Fluorescence Spectroscopy of Single Biomolecules." *Science,* **1999**, *283*, 1676-1683.

3. Joo, C.; Balci, H.; Ishitsuka, Y.; Buranachai, C.; Ha, T. "Advances in Single-Molecule Fluorescence Methods for Molecular Biology." *Annual Review of Biochemistry,* **2008**, *77*, 51-76.

4. Schuster, B. S.; Ensign, L. M.; Allan, D. B.; Suk, J. S.; Hanes, J. "Particle tracking in drug and gene delivery research: State-of-the-art applications and methods." *Advanced Drug Delivery Reviews,* **2015**, *91*, 70-91.

5. Berg, H. C. "How to track bacteria." *Review of Scientific Instruments,* **1971**, *42*, 868-871.

6. Ha, T.; Chemla, D. S.; Enderle, T.; Weiss, S. "Single molecule spectroscopy with automated positioning." *Applied Physics Letters,* **1997**, *70*, 782-782.

7. Enderlein, J. "Tracking of fluorescent molecules diffusing within membranes." *Applied Physics B,* **2000**, *71*, 773-777.

8. Levi, V.; Ruan, Q.; Kis-Petikova, K.; Gratton, E. "Scanning FCS, a novel method for three-dimensional particle tracking." *Biochemical Society transactions,* **2003**, *31*, 997-1000.

9. Berglund, a. J.; Mabuchi, H. "Feedback controller design for tracking a single fluorescent molecule." *Applied Physics B: Lasers and Optics,* **2004**, *78*, 653-659.

10. Cang, H.; Wong, C. M.; Xu, C. S.; Rizvi, A. H.; Yang, H. "Confocal three dimensional tracking of a single nanoparticle with concurrent spectroscopic readouts." *Applied Physics Letters,* **2006**, *88*, 1-3.

11. Cang, H.; Xu, C. S.; Montiel, D.; Yang, H. "Guiding a confocal microscope by single fluorescent nanoparticles." *Optics Letters,* **2007**, *32*, 2729-2731.

12. Levi, V.; Ruan, Q.; Gratton, E. "3-D particle tracking in a two-photon microscope: application to the study of molecular dynamics in cells." *Biophysical Journal,* **2005**, *88*, 2919-2928.

13. Levi, V.; Ruan, Q.; Plutz, M.; Belmont, A. S.; Gratton, E. "Chromatin dynamics in interphase cells revealed by tracking in a two-photon excitation microscope." *Biophysical Journal,* **2005**, *89*, 4275-4285.

14. Levi, V.; Serpinskaya, A. S.; Gratton, E.; Gelfand, V. "Organelle transport along microtubules in Xenopus melanophores: evidence for cooperation between multiple motors." *Biophysical Journal,* **2006**, *90*, 318-327.

15. Levi, V.; Gelfand, V. I.; Serpinskaya, A. S.; Gratton, E. "Melanosomes transported by myosin-V in Xenopus melanophores perform slow 35 nm steps." *Biophysical Journal,* **2006**, *90*, L07-09.

16. Ragan, T.; Huang, H.; So, P.; Gratton, E. "3D particle tracking on a two-photon microscope." *Journal of Fluorescence,* **2006**, *16*, 325-336.

17. Lanzanò, L.; Gratton, E. "Orbital single particle tracking on a commercial confocal microscope using piezoelectric stage feedback." *Methods and Applications in Fluorescence,* **2014**, *2*, 024010-024010.

18. McHale, K.; Berglund, A. J.; Mabuchi, H. "Quantum Dot Photon Statistics Measured by Three-Dimensional Particle Tracking." *Nano Letters,* **2007**, *7*, 3535-3539.

19. Berglund, A. J.; Mabuchi, H. "Performance bounds on single-particle tracking by fluorescence modulation." *Applied Physics B: Lasers and Optics*, **2006**, *83*, 127-133.

20. McHale, K. *Feedback tracking and correlation spectroscopy of fluorescent nanoparticles and biomolecules.* PhD Thesis, California Institute of Technology, 2008.

21. Perillo, E. P.; Liu, Y.-L.; Huynh, K.; Liu, C.; Chou, C.-K.; Hung, M.-C.; Yeh, H.-C.; Dunn, A. K. "Deep and high-resolution three-dimensional tracking of single particles using nonlinear and multiplexed illumination." *Nat Commun,* **2015**, *6*.

CHAPTER 7

CONCLUSIONS AND OUTLOOK

Fluorescence microscopy has made significant contributions to our understanding of physical, chemical and biological processes. However, limitations in our ability to discriminate between the signal of interest and background will continue to provide challenges as systems of increasing complexity, lower copy number, and smaller length scales are studied. Improved sensitivity will always be an important part of overcoming these obstacles, whether novel fluorophores, techniques, or applications are employed.

Intrinsic electronic properties of fluorophores are of paramount importance, as fundamental losses due to non-emissive relaxations are not recorded as fluorescence. However, if the analyte is uniquely sensitive to external stimuli, it is possible to separate it from endogenous background, paving the way for higher sensitivity. The use of dual excitation opens multiple avenues for study. For example, in Chapter 4, pulsed excitation combined with long wavelength repumping is a novel approach to attain theoretically background free signal recovery, but is limited to fluorophores that are sensitive to two photon sequential photobrightening. Optical modulation can also be leveraged to quantitatively recover analyte concentrations amid background through application of correlation subtraction, though application of Fourier transforms is more robust.

Correlation and correlation-like statistics can also be applied to fluorescence imaging and spectroscopy in novel ways. Synchronously amplified fluorescence image recovery – fluorescence correlation spectroscopy (SAFIRe-FCS) is presented in Chapter 3 and combines the sensitivity of optical modulation with the statistical averaging of autocorrelations. Proof-of-concept is demonstrated through improvement of FCS sensitivity. SAFIRe-FCS was also demonstrated to quantitatively recover concentrations amid a highly autofluorescent background. Cumulants, which can be represented as

multi-order correlations, are utilized in Chapter 5 to improve optical resolution beyond the Abbe limit of diffraction. Cumulants are crucial to the narrowing, as they correlate the n^{th} order blinking statistics of only single emitters, ignoring the simultaneous contributions of multiple emitters. This provides an increased ability to distinguish between independently blinking emitters instead of simply narrowing the point spread function (PSF). Through the use of computer simulations, it was shown that the optical resolution limit may be surpassed in a confocal arrangement. Important fluorophore photophysical characteristics such as short fluorescent lifetimes (few ns) and long dark state lifetimes (~100 μs) which dictate blinking statistics were explored in an effort to identify effective SOFI fluorescent labels.

Finally, high sensitivity measurements are paramount for weak, unsynchronized or infrequent phenomena. Single particle tracking approaches the single molecule level of detail while being less disruptive than immobilization, permitting greater access to unperturbed molecular-level interactions. To this end, a single particle tracking instrument was built and computationally simulated. Tracking results are presented in Chapter 6. Remaining work includes incorporation of optical modulation for tracking in highly fluorescent background such as that of a living cell.

Sensitivity is perhaps the largest barrier to studying systems of decreasing size and increasing biological complexity. Novel applications of optical modulation, higher order statistics, and instrumental design have been demonstrated in this thesis to improve sensitivity in fluorescence-based imaging. Techniques designed around higher sensitivity will be increasingly important as smaller length scales, environments with higher background, and weakly observable phenomena are explored.